



HAL
open science

Tumbling, bending, stretching: particles in laminar and chaotic flows

Emmanuel Lance Christopher Vi Medillo Plan

► **To cite this version:**

Emmanuel Lance Christopher Vi Medillo Plan. Tumbling, bending, stretching: particles in laminar and chaotic flows. Other [cond-mat.other]. COMUE Université Côte d'Azur (2015 - 2019), 2017. English. NNT: 2017AZUR4032 . tel-01589397

HAL Id: tel-01589397

<https://theses.hal.science/tel-01589397>

Submitted on 18 Sep 2017

HAL is a multi-disciplinary open access archive for the deposit and dissemination of scientific research documents, whether they are published or not. The documents may come from teaching and research institutions in France or abroad, or from public or private research centers.

L'archive ouverte pluridisciplinaire **HAL**, est destinée au dépôt et à la diffusion de documents scientifiques de niveau recherche, publiés ou non, émanant des établissements d'enseignement et de recherche français ou étrangers, des laboratoires publics ou privés.

École doctorale Sciences Fondamentales et Appliquées
Unité de recherche : Laboratoire Jean Alexandre Dieudonné UMR 7351

Thèse de doctorat

Présentée en vue de l'obtention du
grade de Docteur en Physique de
Université Côte d'Azur

par

Emmanuel Lance Christopher VI Medillo PLAN

Tumbling, bending, stretching : particles in laminar and chaotic flows

Dirigée par *Hélène Politano, Directrice de Recherche, Université Côte d'Azur*
et codirigée par *Dario Vincenzi, Chargé de Recherche, Université Côte d'Azur*

Soutenue le 15 juin 2017
Devant le jury composé de :

Roberto	Benzi	Professeur, Università di Roma "Tor Vergata"	Rapporteur
Bernhard	Mehlig	Professeur, Göteborgs Universitet	Rapporteur
Anke	Lindner	Professeur, Université Paris Diderot	Examinatrice
Rahul	Pandit	Professeur, Indian Institute of Science	Examineur
Massimo	Vergassola	Professeur, University of California San Diego	Examineur
Hélène	Politano	Directrice de Recherche, Université Côte d'Azur	Directrice de thèse
Dario	Vincenzi	Chargé de Recherche, Université Côte d'Azur	Directeur de thèse

Acknowledgments

*“Ang hindi marunong lumingon sa pinanggalingan
ay hindi makararating sa paroroonan.”*

*Whoever does not know to look back from whence (s)he came
will not arrive to where (s)he shall go.*

– Filipino proverb

It is fitting to start the thesis, the culmination of my doctoral journey, by looking back and knowing that I had never been alone and that I could not have gone a step farther had it not been for those who have sustained my strength, my happiness, my tranquility.

First and foremost, I thank the Lord Almighty for the opportunity to continue my academic journey in the form of a Ph.D. in Nice, France and actually accomplish this feat within three years.

I was blessed to work under the supervision of Dario Vincenzi and H el ene Politano and thank them for their support. I would like to honour Dario in a special way, for having patiently guided me and shared with me his expertise, passion, ingenuity. Most importantly, he had etched upon me, by means of leading by example, the importance of being a good person. Dear “Sir”, my heartfelt thanks for all that we have shared.

I would like to acknowledge Roberto Benzi and Bernhard Mehlig for accepting to be referees of my thesis. Likewise, I thank Anke Lindner, Rahul Pandit and Massimo Vergassola, all members of the jury for their time and interest in my work. I appreciate their appreciation of my work and their helpful comments and suggestions.

This thesis could not have materialized without the significant contributions of my collaborators: Aamir Ali, John Gibbon, Anupam Gupta, Stefano Musacchio, Samriddhi Sankar Ray. Their openness in sharing their wisdom and knowledge helped me to mature scientifically. I also thank other friends who work in fluid mechanics and with whom I have interacted with in one way or another: Holger, Jeremie, Giorgio, Lionel, Fran ois, Mamadou, Martin, Adeel.

I have greatly benefited from the generosity of the European Union, which, through the Erasmus Mundus Mobility with Asia (EMMA) program, provided the scholarship for my doctoral studies. In particular, I thank the coordinators Francine and Marc. The whole EMMA team must be acknowledged for their hard work and for their friendliness, above all, Julie and Gildas. I also thank the fellow EMMA scholars with whom I have spent time with during my stay in Nice. I also acknowledge the Cooperation for Science and Technology Action MP1305, which by sponsoring conferences and summer schools allowed me to meet fellow researchers in the field of fluid dynamics.

I thank the Ateneo de Manila University, in particular the Mathematics Department, for their friendship and never-ending support. I likewise thank the Laboratory J. A Dieudonné for hosting me for the past three years. In a special way I thank Jean-Marc, Roland, Julia, Angelique and Victoria for their friendship and their valuable technical and administrative assistance.

Spending three years in a single building would have been lonely had I not met wonderful colleagues: Emiliano, Mayya, Vova, Zeinab, Chenmin, Jiqiang, Si Jie, Luis, Marcella, Huda, Yen, Ratti, Rinel, Jafar. It is my pleasure to have spent time with you.

Being far away from home, I have found a community in the Filipino Catholics in Nice. I like to thank them for their camaraderie and for impressing on me that I am not alone. I thank our chaplains Fr. Gerry and Fr. Bong, and my surrogate mothers Nanay Lily, Nanay Mel, Nanay Fila, Nanay Puring. I must not forget the people with whom I spent much time singing, eating and dancing: Vicky, Lea, Jocelyn, Josie, Jun M, Richard, Zeny, Jun Z, Frosie, Bong, Romel, Ijay, Orben, Rommel, Vilma, Jean-Claude, Chelsea, Pascal, Raphael, Neneth, Boy, Andy, Nanette, Edgar, Eleanor, Boy, Maricar, John-john, Mabelle, Remi, Dayang, Anamae, Tess, Mercy, and all the other members of the community that I may have missed out in this already extensive list. Rest assured that you will remain in my prayers as I hope I remain in yours.

I now turn to, perhaps against their wishes, magnify my friends with whom I have spent a lot of time with during the past three years. They have brought me joy and I am assured of a continuing and lasting friendship. *Merci, mes amis*: Christian, Kate, Typ, Jasmin, Joy, Jethro, Ricky, Raissa, Sophie, Martin, Sandi, Win, Bien, Anh, Lam, Yen. I append to this list certain people I met and who have kept in touch: bà, chú, cô, chi Thuy, Lan, Duc, Natasha, Misha, the Breaking Pandesal group, Tita Vina, Sir Arsen(+), Maam Rechie, Maam Mari-Jo.

Even if people start fear that this thesis is a litany of names, I continue to enumerate, now, those who have always been there from the start, constantly sending me support by messages and long-distance video calls. This work I dedicate to my family: Mom, Dad, Kuya EG, Ate Mean, Kuya EA, Ate Mags, Kuya EL, Ate Poi, EJ, Gab, Benedict, Aubrey, my *titas* and *titos*, cousins, nephews, nieces. I take this opportunity to thank Ate Rose, Ate Ellen, Kuya Ric, Kuya Meyo, members of my extended family.

Lastly, to my friend who has been by my side during my doctoral journey and who has shared with me the joys and sorrows of becoming a “doctor”, the long working hours and the short lunch and coffee breaks, and the discovery of the world which used to exist only in pictures. I thank you, my dear Huong, for encouraging and supporting me and above all, for making my life more colorful – especially with your sweet smile.

And if I accidentally forgot to put your name, kind reader, in one of these lists, let me make amends by treating you to two scoops of *gelato*. My deepest gratitude to all who have been part of this chapter of my life. *Maraming salamat po!*

Contents

Acknowledgments	i
Abstract in English	1
Abstract <i>en français</i> (Résumé)	3
General introduction	5
References - General Introduction	7
Additional remarks on the thesis	9
List of publications accomplished during the doctorate	11
Part I. Single-particle dynamics	13
Introduction	15
Chapter 1. Tumbling in an extensional flow	21
1.1. Introduction	21
1.2. The trumbbell	25
1.3. The angular formulation of the trumbbell	27
1.4. Stationary statistics in the extensional flow	32
1.5. Tumbling dynamics	37
1.6. Concluding remarks and perspectives	40
1.7. Appendices	41
Chapter 2. Bead-rod-spring models in random flows	45
2.1. Introduction	45
2.2. Bead-rod-spring models	46
2.3. Diffusion equation for a short-correlated random flow	48
2.4. An example: the rhombus model	51
2.5. Concluding remarks and perspectives	56
2.6. Appendices	56
Chapter 3. Bending of semiflexible particles in turbulent flows	61
3.1. Introduction	61
3.2. Bending in the extensional flow	62
3.3. Bending in a random flow	65
3.4. Direct numerical simulations	67
3.5. Concluding remarks and perspectives	68
3.6. Appendix	69
Bibliography - Part I	73

Part II. Chaotic dynamics at low Reynolds number	79
Introduction	81
Chapter 4. Lyapunov dimension of elastic turbulence	85
4.1. Introduction	85
4.2. Lyapunov exponents of dynamical systems	86
4.3. The 2D Oldroyd-B model for polymer solutions	90
4.4. Estimating the Lyapunov dimension	91
4.5. Direct numerical simulations of elastic turbulence	97
4.6. Conclusions and perspectives	99
4.7. Appendices	100
Chapter 5. Emergence of chaos in a viscous solution of rodlike polymers	103
5.1. Introduction	103
5.2. The model of rodlike-polymer solutions	104
5.3. Numerical simulations	106
5.4. Analysis	106
5.5. Concluding remarks and perspectives	109
Bibliography - Part II	111

Abstract in English

Particles, when subjected into a flow, display non-trivial dynamics comprised of a variety of deformations and predominant orientations depending on their elasticity and geometry and the flow velocity field. Flows can conversely be modified when the particle stresses are sufficiently large. This thesis presents theoretical and numerical results on this two-way relationship between particles and flows in two parts.

Part I starts with a stability analysis and numerical simulations that show a semiflexible Brownian particle in an extensional flow undergo tumbling, a phenomenon commonly associated with shear flows only. Chapter 2 extends analytical tools only available for elementary polymer models or for steady flows to general bead-rod-spring models in a random flow. By building on the previous chapters, Chap. 3 culminates with the study of a yet unexplored Lagrangian degree of freedom in a turbulent flow: bending. A semiflexible particle is shown to display different bending behaviours in two- and three-dimensional random flows. This prediction is confirmed via direct numerical simulations in turbulent flows.

Part II concerns “elastic turbulence”, a chaotic regime created in a flow with low inertial forces by the addition of elastic polymers. Chapter 4 provides an estimate for the number of degrees of freedom of the solution of this chaotic system via the Lyapunov dimension of the attractor of the two-dimensional Oldroyd-B model, a model known to reproduce elastic turbulence. Chapter 5 questions the necessity of elasticity in producing the aforementioned chaotic regime and concludes that a rodlike-polymer solution can create a regime similar to elastic turbulence.

Abstract *en français* (Résumé)

Des particules dans un écoulement présentent des dynamiques non triviales basées sur des déformations variées et des orientations privilégiées des particules, selon leur élasticité et géométrie, et la structure du champ de vitesse. Réciproquement, un écoulement peut être modifié lorsque les contraintes dues aux particules sont suffisamment intenses. Cette thèse expose des résultats théoriques et numériques sur cette inter-relation.

La I^{ère} partie de la thèse débute par une analyse de stabilité et des simulations numériques montrant qu'une particule brownienne semi-flexible dans un écoulement hyperbolique effectue un mouvement de retournement; un phénomène généralement associé aux écoulements cisailés. Le Chap. 2 étend des outils analytiques connus, pour des modèles de polymères simples ou pour des écoulements indépendants du temps, aux modèles "bead-rod-spring" généraux dans un écoulement aléatoire. A partir des résultats précédents, le Chap. 3 aboutit à l'étude d'un degré de liberté lagrangien jusqu'ici inexploré dans un écoulement turbulent: la flexion. La statistique de la flexion d'une particule semi-flexible dépend fortement de la dimension de l'écoulement aléatoire sous-jacent.

La II^{ème} partie concerne la turbulence élastique; un régime chaotique créé en ajoutant des polymères élastiques dans un écoulement à faible inertie. Le Chap. 4 estime le nombre de degrés de liberté d'une solution de ce régime en calculant la dimension de Lyapunov de l'attracteur du modèle Oldroyd-B bidimensionnel. Le Chap. 5 étudie une solution diluée de polymères rigides et montre que l'élasticité n'est pas indispensable pour générer un régime comparable à celui de la turbulence élastique.

General introduction

There is a two-way relationship between particles and flows. Indeed the dynamics of a particle depends on the flow in which it is immersed, and conversely, a flow can feel the particles and can be modified owing to their presence. The former is often studied by considering how a single particle behaves under the effect of a flow. These particles can be polymers, rods, filaments, red blood cells, vesicles, among others. For instance, rods and elastic filaments are found to align in the direction of a shear flow; such a configuration is unstable and particles perform end-over-end reversals [7, 15]. Particles may also deform, such as flexible fibers that buckle into U-shaped, S-shaped, or even W-shaped figures when transported in a cellular flow [10].

One of the well-studied dynamics is the stretching of a flexible object in a flow. In particular, Perkins et al. observed that an extensional flow stretches a DNA polymer [13], consistent with the predictions of de Gennes on the coil–stretch transition of elastic particles in time-independent extensional flows [5]. This transition depends on the ratio of the magnitude of the velocity gradient to that of the elastic force. If the flow is not strong enough to overcome the elastic forces of the polymer, the polymer would remain in its equilibrium coiled state. A sufficiently strong flow would however stretch it to its maximum length. The coil–stretch transition also exists for chaotic flows, but the transition between the coiled and stretched configurations is not as sharp and a polymer may more easily switch between the two configurations [1]. These differences are due to the fluctuating nature of the velocity gradient.

The examples above illustrate how a particle may orient or deform under the effect of a flow. In the presence of a sufficient quantity of these particles, the fluid or flow properties may display non-Newtonian effects due to the feedback of the particles. One of the more amusing ones is the phenomenon of shear-thickening [4]. Such an idea is frequently demonstrated in scientific fairs, where children are asked to run over a tub of water mixed with substantial amounts of cornstarch. In the presence of rapid successive running or jumping motions, the water-cornstarch solution displays shear-thickening and allows a person to momentarily not submerge in the fluid; shear-thickening is defined as an increase in the viscosity of the fluid with increasing shear rate in a steady shear flow.

Of perhaps more practical importance is that the addition of even a few parts per million of elastic particles such as polyacrylamide or polyethylene oxide in turbulent flows can reduce drag resistance [2, 12, 14]. The applications of drag reduction range from efficient fluid transfer in pipes that are used in industrial companies to efficient water usage and controllability in firefighting [8, 17]. Drag reduction may be obtained by using either rigid or flexible particles [14, 16, 17]. A main difference, however, is the necessity of higher concentrations of rigid polymers to achieve maximum drag reduction; less flexible polymers are required if both the turbulent intensity of the flow and polymer elasticity are sufficiently high [14]. This implies that elasticity plays a significant role in the amplification of elastic stresses in cases of low concentration.

The phenomenon of drag reduction described above emerges when polymers are injected in a flow that is otherwise turbulent. With low fluid inertia, a flow without any polymers is laminar. The presence of elastic particles in such a flow however triggers elastic instabilities and creates a turbulent-like regime characterized by the activation of a range of scales in the kinetic-energy spectrum and an increase in both the flow resistance and the elastic stresses as polymer elasticity increases [9]. The emergence of this chaotic regime dubbed as “elastic turbulence” is attributed to the stretching of polymers, which absorb energy, stretch and produce a secondary flow (see, e.g., Refs. [3, 9]).

The association of the viscoelastic effects above to polymer-stretching illustrates how single-polymer dynamics and their collective effect are inseparable. Indeed, the constitutive models of polymer solutions with which analytical and numerical calculations reproduce the aforementioned phenomena can be derived from equations describing the evolution of a single particle in the flow (see, e.g., Refs. [6, 11]). This thesis presents analytical and numerical results on certain aspects of this relationship.

Part 1 of this thesis considers single-particle dynamics towards understanding a Lagrangian degree of freedom that, as far as we know, has not yet been explored in a turbulent flow: bending. Chapter 1 reports the existence of tumbling, a phenomenon normally associated to shear flows, in a purely extensional flow. To this end, a stability analysis and numerical simulations were performed on the dynamics of a simple semiflexible Brownian particle in an extensional flow. Chapter 2 extends tools currently available only for elementary polymer models or for steady flows to general-bead-rod spring models in random flows. By then building on the stability analysis in Chap. 1 and by utilising the analytical tools derived in Chap. 2, Chapter 3 provides an analytical prediction on the bending dynamics of a semiflexible particle in a turbulent flow. This prediction is confirmed via direct numerical simulations of the Lagrangian trajectories of the particle in a turbulent flow.

Part 2 of this thesis discusses some properties of elastic turbulence. Chapter 4 provides an estimate for the number of degrees of freedom of the solution of this chaotic system via the Lyapunov dimension of the attractor of the two-dimensional Oldroyd-B model, which is known to reproduce elastic turbulence successfully in numerical simulations. Chapter 5 questions the necessity of elasticity in producing a turbulent-like regime. It will be shown that even a solution of rigid rodlike polymers can create a chaotic regime similar to elastic turbulence.

References - General Introduction

- [1] Balkovsky E, Fouxon A, Lebedev V. *Phys. Rev. Lett.* **84**, 4765 (2000).
- [2] Benzi R. *Physica D* **239**, 1338 (2010).
- [3] Berti S, Bistagnino A, Boffetta G, Celani A, Musacchio S. *Phys. Rev. E* **77**, 055306(R) (2008).
- [4] Bird RB, Curtiss CF, Armstrong RC, Hassager O. *Dynamics of Polymeric Liquids* (1987).
- [5] De Gennes PG. *J Chem. Phys.* **60**, 5030 (1974).
- [6] Doi M, Edwards SF. *The Theory of Polymer Dynamics* (1988).
- [7] Einarsson J, Johansson A, Mahata SK, Mishra Y, Angilella JR, Hanstorp D, Mehlig B. *Acta Mechanica* **224**, 2281 (2013).
- [8] Fabula AG. *J. Basic Eng.* **93**, 453 (1971).
- [9] Groisman A, Steinberg V. *Nature* **405**, 53 (2000).
- [10] Lindner A, Shelley M. In *Fluid–Structure Interactions in Low Reynolds-Number Flows* (eds. C. Duprat and H. Stone) (2016).
- [11] Öttinger HC. *Stochastic Processes in Polymeric Fluids* (1996).
- [12] Pandit R, Perlekar P, Ray SS. *Pramana* **73**, 157 (2009).
- [13] Perkins TT, Smith DE, Chu S. *Science* **276**, 2016 (1997).
- [14] Procaccia I, L'vov VS, Benzi R. *Rev. Mod. Phys.* **80**, 225 (2008).
- [15] Schroeder CM, Teixeira RE, Shaqfeh ESG, Chu S. *Phys. Rev. Lett.* **95**, 018301 (2005).
- [16] Virk PS, Sherman DC, Waggoner DL. *AIChE J.* **43**, 3257 (1997).
- [17] White CM, Mungal MG. *Ann. Rev. Fluids Mech.* **40**, 235 (2008).

Additional remarks on the thesis

This work is a compilation of the work that the student has performed in the course of three years. Parts of the results, such as certain numerical simulations presented here, were done in collaboration with other people. The simulations on the trumbbell in extensional flow (Chap. 1) as well as those on the rodlike polymer solutions (Chap. 5) were wholly performed by the student. The simulation of the trumbbell in a turbulent flow (Chap. 3) is a joint work with S.S. Ray. Lastly, the simulations for the Lyapunov dimension (Chap. 4) were done in collaboration with A. Gupta.

Appendices, when provided, are at the end of each chapter. These appendices describe or explain some technical terms or detailed calculations that the student skipped to avoid lengthy digressions. Note also that the variables used in the appendices may not necessarily hold the same definition as elsewhere in the previous chapters due to the extensive use of notations.

Two sets of bibliographic entries are provided, one at the end of each part. Each set is a compilation of the entries from the relevant chapters preceding the bibliography.

List of publications accomplished during the doctorate

Publications relevant to Part 1 of the thesis:

- E.L.C. VI M. Plan & D. Vincenzi. Tumbling of a Brownian particle in an extensional flow. *Proc. R. Soc. A* **472**, 20160226 (2016).
- E.L.C. VI M. Plan, A. Ali & D. Vincenzi. Bead-rod-spring models in random flows. *Phys. Rev. E*, **94** 020501(R) (2016).
- A. Ali, E.L.C. VI M. Plan, S.S. Ray & D. Vincenzi. Semiflexible particles in isotropic turbulence. *Phys. Rev. Fluids*, **1** 082402(R) (2016).

Publications relevant to Part 2 of the thesis:

- E.L.C. VI M. Plan, A. Gupta, D. Vincenzi & J.D. Gibbon. Lyapunov dimension of elastic turbulence. *J. Fluid Mech.*, **822** R4 (2017)
- E.L.C. VI M. Plan, S. Musacchio & D. Vincenzi. Emergence of chaos in a viscous solution of rodlike polymers. In submission.

Part I

Single-particle dynamics

Introduction

Understanding particle-laden flows often requires understanding how a single particle behaves in these flows. Whereas following the evolution of a single particle instead of hundreds is evidently advantageous in experimental set-ups, this single-particle approach is practical more so from the theoretical and numerical point of view because the number of degrees of freedom becomes significantly low to allow a more complete understanding of the particle, its dynamics, and its potential effect on the flow. Limiting the observation to one particle also permits the isolation of the effects of the flow on the particle from all other effects. In particular it is possible to neglect the feedback flow that the particle may induce on the flow by assuming that the stress it exerts on the fluid is negligible. Hydrodynamic interactions that would be present in non-dilute suspensions may also be safely disregarded. Fundamental results on dilute polymer solutions also indicate that the quantities measuring the rheological properties of these solutions are but linear combinations of those from more dilute solutions, i.e. the effect of the particles on these quantities is proportional to their concentration [60]. Hence, single-particle dynamics provides a first step towards the general behaviour of particles in a flow.

The simplification to a single particle does not prevent it from displaying rich dynamics, as displayed by the multitude of research being performed. The study of particle transport and dynamics involves a variety of different particles: models exist depending on whether they are passive or active [34, 97], tracer or inertial [17, 35, 97], pointlike, rodlike or complex-shaped [21, 22, 32, 87, 102, 106], elastic or rigid [12, 12, 33, 45, 65, 75], not to mention biological particles [27, 52, 53]. The choices for the flow into which these particles can be subjected into are likewise extensive: laminar [16, 60, 75], random [14, 69, 72], or turbulent [35, 42, 73]. The presence of boundaries or obstacles may further increase the complexity of the problem [7, 65].

Some recent work on particle dynamics include that on crosses and jacks [66], which are manufactured by three-dimensional printing. They confirm existing analytical and numerical results on the rotation of spherical and ellipsoidal objects in turbulent flow. The study of rigid triaxial ellipsoids [21] and four-bead particles [43], extend these studies on the effect of turbulent flow on spheroidal particles by reducing symmetry and thereby allowing more non-trivial dynamics. Chiral dipoles provide an example of particles without axial symmetry but retaining rotational symmetry and were shown to perform preferential rotation in isotropic turbulence (see Fig. I.1) [56]. Another active field of research is the study of deformable particles motivated by biological structures, such as the helical-shaped flagella of some bacteria. Helices of nanoscale thickness were synthesized and were found to considerably uncoil in a high-velocity flow and relax back to its coiled structure when the flow is turned off (see Fig. I.2). Environmentally-motivated research also require modelling more complex particles. For instance, aerosols particles are not perfect spheres but are generally modeled as such. A slightly more complex model than a sphere is given

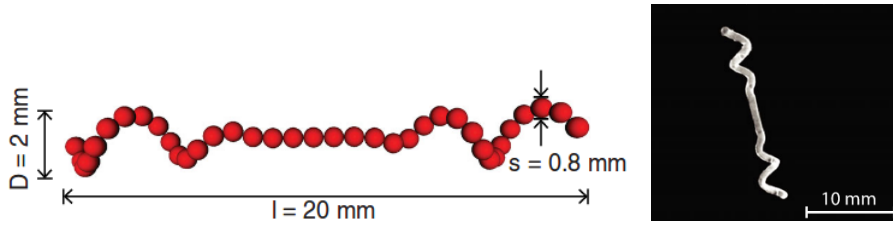


FIGURE I.1. (Left) A model of a chiral dipole made of 40 spheres. (Right) A chiral dipole produced by 3D printing. From Ref. [56]. Reprinted figure with permission from Kramel S, Voth GA, Tymphel S, Toschi F, *Phys. Rev. Lett.* **117**, 154501 (2016). Copyright (2016) by the American Physical Society.

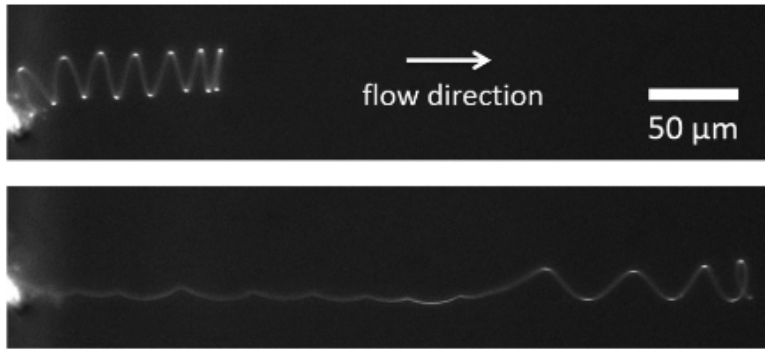


FIGURE I.2. Deformation of a synthesized helix of thickness around 50 nm in a flow of order 10 mm/s. From Ref. [75]. Reprinted figure with permission from Pham J, Morozov A, Crosby AJ, Lindner A, du Roure O, *Phys. Rev. E*, **92**, 011004(R) (2016). Copyright (2016) by the American Physical Society.

by isotropic helicoids, which are spheres endowed with an internal parity orientation (see figure I.3). These isotropic helicoids break reflection invariance but preserve rotation invariance; the so-called left-handed particles and right-handed particles respond differently to the same vortical structures [43, 44].

The wide interest on particle dynamics in laminar and turbulent flows is not surprising given that the applications span various sciences from biology to meteorology. In biology, the dynamics of microscopic particles like red blood cells, bacteria and DNAs have continuously been studied [27, 53, 64]. For instance, understanding the particle dynamics in blood, which is a dense suspension, gives insight into the rheological properties of the blood cells, which in turn is related to the stable circulation of blood called homeostasis. The study of the dispersion of particulates in the atmosphere and in cities are of clear practical importance. To cite an example, the exposure of the city to toxic ozone particulates were linked to regional wind patterns and day-night and seasonal thermal fluctuations [49]. These various studies nevertheless rely on possibly the same underlying physics of complex flows and fluids, thereby motivating studying the simple models of particles in flows and their behaviours.

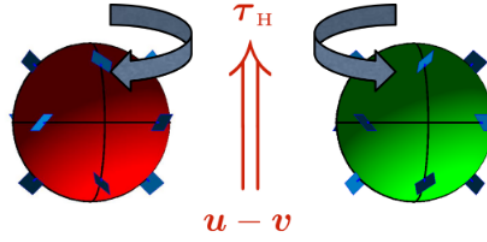


FIGURE I.3. Illustration of a left-handed (left) and a right-handed (right) helocoid. The velocity difference between that of the fluid \mathbf{u} and the particle \mathbf{v} results in a net torque τ_H produces a (counter-) clockwise motion for the (right-) left-handed helicoid. From Ref. [44]. Reprinted figure with permission from Gustavsson K, Biferale L, *Phys. Rev. Fluids***1**, 054201 (2016). Copyright (2016) by the American Physical Society.

The first part of the thesis consists of three chapters on the dynamics of simple particles in various flows. Even if each chapter has its own intrinsic interest, a common thread lies in studying the bending dynamics of a particle in a turbulent flow. Indeed, the first chapter introduces a prototype three-bead-two-rod trumbbell model (see Fig. I.4) and studies its bending (and tumbling) dynamics in a purely extensional flow as a first step towards turbulence. The second chapter equips the reader with an analytical tool to study complex-shaped particles in random flows, which had been previously used to predict particle dynamics in turbulent flows. By building on the results of the first two chapters, the third chapter addresses the question of bending of semiflexible particles in a turbulent flow. This Lagrangian degree of freedom, to the best of my knowledge, has not yet been explored. The contents of each chapter are further detailed below.

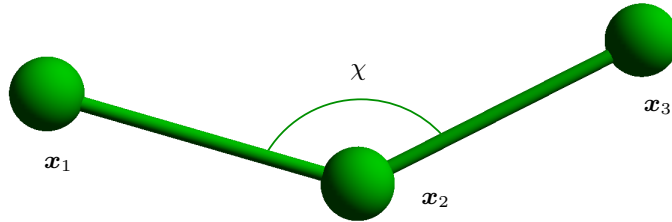


FIGURE I.4. The trumbbell model, consisting of three beads at $\mathbf{x}_1, \mathbf{x}_2, \mathbf{x}_3$ connected by two rigid rods. The internal angle between the rods is χ .

Chapter 1

In the first chapter, the phenomenon of tumbling, i.e. the reversal of orientation of microscopic objects is explored in stretching-dominated flows. Tumbling is commonly associated with shear flows, but has not been reported in extensional flows. To see if tumbling may occur in a non-fluctuating planar extensional velocity field, the dynamics of a semiflexible trumbbell is studied. Indeed a simpler two-bead “dumbbell” model would remain aligned to the stretching direction and be

unable to perform tumbling. Having a single bending mode proves to be sufficient to exhibit tumbling. The study commences in two dimensions, wherein two stable configurations (extended and folded) of the trumbbell are established. It is then shown to undergo a random tumbling-through-folding motion from one extended configuration to another. The probability distribution of long tumbling times is exponential with a mean time exponentially increasing with the Weissenberg number, which compares the strength of the extensional flow to that of the trumbbell's elastic restoring potential. The results are then explained by considering tumbling as an escape from a basin of attraction. Analogous results are drawn for three-dimensional planar extensional flows.

Chapter 2

Towards the goal of studying the bending dynamics in a turbulent flow, the trumbbell may be subjected to a random flow. An important tool used in Chap. 1 is the diffusion equation for a trumbbell, whose solution gives the probability density function of the configuration of the particle. The diffusion equation as provided (e.g. in Ref. [10]) can be easily extended for a general-bead-rod-spring model. This equation is not however directly applicable when considering random flows. In this chapter, the diffusion equation for a general bead-rod-spring model in short-correlated Gaussian random flows is derived. To illustrate its practicality, this equation is solved analytically under isotropic conditions for a finitely-extensible model that has both rigid and elastic links. Its application to the trumbbell is left to the next chapter.

Chapter 3

The first part of the thesis culminates with the third chapter, which is on the study of the bending dynamics of a particle in a turbulent flow. Bending is one of the simplest deformations that a flexible polymer may experience, and yet, it has not been explored before in a turbulent flow. To this end (and once again), the simplest model that can exhibit bending is considered: a trumbbell that has but a single bending mode. This chapter builds on the insights from purely extensional flows (Chap. 1) so as to highlight the effect of turbulence on the bending dynamics. The Lagrangian dynamics of the trumbbell in homogeneous and isotropic turbulent flows is then studied in the context of a short-correlated random flow, whose associated diffusion equation is derived in Chap. 2. Finally, the predictions of this analytically solvable model are confirmed by using direct numerical simulations of a turbulent flow. The stationary statistics of the bending angle of the trumbbell shows a strong dependence on the dimension of the flow. In two-dimensional turbulence, particles are either found in a fully extended or in a fully folded configuration. In three dimensions, the predominant configuration is the fully extended one. Such a sensitivity of the bending statistics on the dimensionality of the flow is peculiar to fluctuating flows and is not observed in laminar stretching flows. These results are explained by considering the temporal statistics of folding and unfolding.

CHAPTER 1

Tumbling in an extensional flow

1.1. Introduction

Various microscopic objects, when immersed in a laminar shear flow, perform a tumbling motion in the plane of the shear. These include anisotropic solid particles, flexible and semiflexible polymers, vesicles, bacteria, red blood cells. Even though tumbling may be simply defined as a reversal of the orientation of a particle with respect to some referential orientation, the entirety of the tumbling motion may exhibit richer dynamics commensurate to the complexity of the particle.

One of the most famous studies of tumbling in a viscous fluid is that of Jeffery, where the motion of an spheroidal object in a viscous shear flow is described [51]. In the absence of external forces, an axisymmetric particle will perform a periodic motion and, depending on its initial orientation define one of the marginally-stable “Jeffery’s orbits”; the associated period can be calculated as a function of the shear rate and the particle’s aspect ratio. Interestingly, even bacteria (e.g. *Escherichia coli*) that are not completely axisymmetric display a tumbling behaviour in a shear flow following the predictions of Jeffery. Based on a microfluidic experiment using shear flow, Kaya and Kosher have produced a model that can estimate the period of a tumbling as a function of the aspect ratio of the bacteria and the distance of its centre from the wall of the microfluidic device [53]. Other particles that lose the completely axisymmetric property may still tumble but may possibly deviate from the classical Jeffery orbits. For instance rigid rodlike particles (see Fig. 1.1) with some random deformations at the ends perform quasiperiodic tumbling [31, 33].

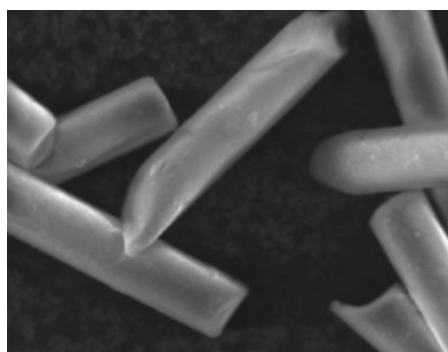


FIGURE 1.1. Asymmetric glass rods in a microchannel; the center rod is approximately $15 \mu\text{m}$ long. From Ref. [33]: Einarsson J, Mihiretie BM, Laas A, Ankardal S, Angilella JR, Hanstorp D, Mehlig B. *Phys. Fluids*, AIP Advances, Vol. **28**, 013302 (2016); used in accordance with the Creative Commons Attribution (CC BY) license.

Rheological particles such as vesicles and red blood cells in a shear flow display a wider variety of dynamics owing to a deformable membrane around the fluid particle



FIGURE 1.2. A red blood cell performs tank-threading in a flow with low shear. From Ref. [27].

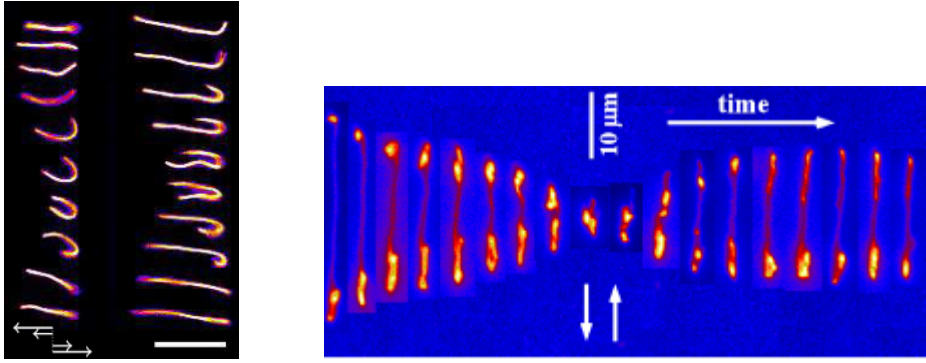


FIGURE 1.3. (Left) Successive snapshots of actin filaments of length $8 \mu\text{m}$ and $16 \mu\text{m}$ show tumbling in a shear flow by buckling. Photo reproduced from Ref. [45]. Reprinted figure with permission from Harasim M, Wunderlich B, Peleg O, Kröger M, Bausch AR, *Phys. Rev. Lett.* **110**, 108302 (2013). Copyright (2013) by the American Physical Society. (Right) A DNA tumbling in a shear flow via a coiling transition. From Ref. [88]. Reprinted figure with permission from Schroeder CM, Teixeira RE, Shaqfeh ESG, Chu S, *Phys. Rev. Lett.* **95**, 018301 (2005). Copyright (2005) by the American Physical Society.

(see Refs. [27, 52] and references therein). Whereas it is observed that they tumble in weak flows similarly to how anisotropic solid particles do, they perform tank-threading in stronger flows. Placing a marker at a fixed point in the membrane allows one to confirm that the membrane deforms, rolls and reverses its orientation like the tracks of a tank; Fig. 1.2 shows such a transition. The extent of the deformation depends on the elasticity of the particle and the strength of the flow. Other non-trivial intermediate dynamics between tumbling and tank-threading have also been observed, such as spinning and vascillating behaviours, and have been studied as functions of the aspect ratio of the particle and the ratio of elastic and viscous forces of the particle and the fluid respectively.

Likewise complex are the behaviours of flexible and semiflexible polymers in shear flows, where the tumbling dynamics goes through buckling or coiling [40, 45, 88]. The buckling behaviour, displayed by actin filaments for instance, is akin to the tank-threading behaviour but in the absence of an internal fluid and a closed membrane. Such a behaviour is seen in Fig. 1.3 (left). Tumbling dynamics may also happen through a coiling transition. For instance, a DNA polymer (see Fig. 1.3) spends most of its time stretched and aligned in the direction of the flow until parts of it, due to thermal fluctuation, lie in the unstable direction of the flow, causing the polymer to (partially) coil. The polymer then tumbles and again stretches and orients to the direction of the shear. This transition is illustrated in Fig. 1.4.

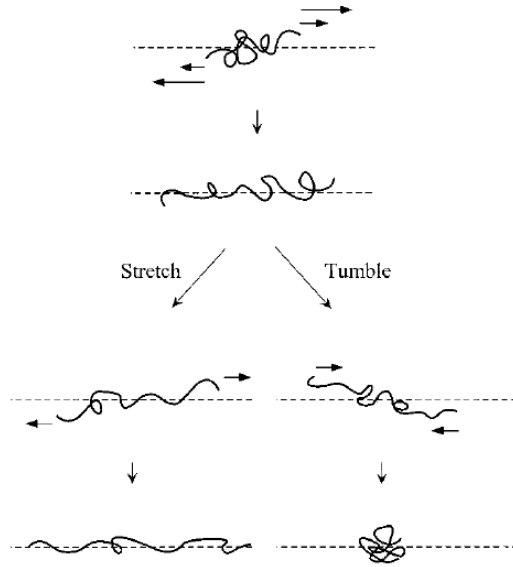


FIGURE 1.4. A polymer in a shear flow stretches in the direction of the shear or tumbles via a coiled configuration. From Smith DE, Babcock HP, Chu S. *Science* **283**, 1724 (1999) (Ref. [93]). Reprinted with permission from AAAS.

The various examples above illustrate the fact that the tumbling dynamics of a particle depends on its nature and on its interaction with the fluid: tumbling may occur only within a restricted range of shear rates, and it can be periodic, chaotic, or random. Numerous numerical studies confirm these experimental observations [8, 9, 50, 92, 104, 107]. In the case of ran tumbling, it would be useful to note the the tumbling time, i.e. the time between two successive reversal of orientations is exponential with a typical tumbling time that decreases as the flow becomes stronger [19, 40, 79, 99].

The general dynamics of tumbling motion in shear flows is captured by some of the simplest objects that tumble, such as axisymmetric solid particles and elastic dumbbells. In a viscous simple shear flow of a Newtonian fluid, indeed, the motion of a neutrally buoyant axisymmetric particle follows Jeffery's orbits as mentioned above: it spends most of the time aligned with the direction of the flow and periodically reverses its orientation [11, 51]. An elastic dumbbell (see Fig. 1.5), which consists of two beads joined by a spring, also performs an end-over-end tumbling motion in a shear flow [15, 19, 79, 99]. The dumbbell models a flexible polymer with an equilibrium length R_0 by its end-to-end vector \mathbf{R} , which captures its length and orientation in space. Under the effect of an incompressible linear velocity field \mathbf{u} (in this case, a shear flow $\mathbf{u} = \lambda(y, 0, 0)$), the evolution of \mathbf{R} obeys the equation (summation over repeated indices is implied throughout this thesis unless otherwise indicated by the presence of a non-vanishing index)

$$\frac{d}{dt}R_i = R_k \partial_k u_i - \frac{f(R^2)}{2\tau} R_i + \sqrt{\frac{R_0^2}{\tau}} \xi_i(t) \quad (1.1)$$

where ∂_k is the derivative in the k th coordinate, $f(R^2)$ is a specific function that expresses the rate of extension (constant equal to 1 in the simplest case), τ is the

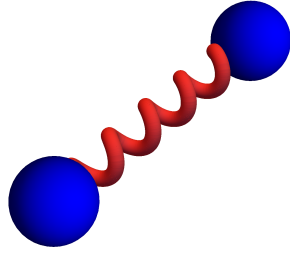


FIGURE 1.5. Illustration of the a dumbbell composed of two beads and an elastic link.

polymer relaxation time and $\xi(t)$ is white noise. Under the effect of Brownian fluctuations, the reversals occur at random times and are characterised by a transition from the stretched to the coiled state. The distribution of the time intervals separating two reversals has an exponential tail with a time scale that decreases as a power-law of the Weissenberg number (the product of the amplitude of the velocity gradient and the relaxation time of the spring). These predictions from the analyses of these simple models explain the numerical and experimental findings.

The descriptions above describe how a *shear* flow affects particles. Here the question of whether tumbling can also exist in *stretching-dominated* flows is addressed. If so, what are the minimal requirements for a particle to tumble in such flows and how does the resulting tumbling motion compare with the analogous motion in a shear flow? The orientational dynamics of an axisymmetric solid particle or of an elastic dumbbell in a purely *extensional* velocity field is trivial: such objects indeed simply align with the stretching direction. In order to observe tumbling in the extensional flow, particles that permit different dynamics, e.g. bending, must be considered. The ‘trumbbell’, also known as trimer or three-bead-two-rod model, is one of the simplest semiflexible objects. It consists of three beads joined by two rigid connectors and of an elastic hinge at the central bead [10, 46]. Owing to its simplicity, it was initially introduced in chemical physics to study analytically the low-frequency dynamics of stiff macromolecules [10, 37, 46, 85]. It was also used as the prototypical system for showing that the infinite-stiffness limit of elastic bonds is singular, i.e. the behaviour of elastic polymers with vanishing elasticity does not correspond to the behaviour of their completely rigid counterparts [48].

The trumbbell model is sufficient to respond to the question posed above. Indeed it is shown in this chapter that a particle in the form of a trumbbell may tumble in an extensional flow. It initially spends a significant amount of time extended and oriented along the stretching direction of the flow. Occasionally, a favourable sequence of Brownian fluctuations makes the trumbbell fold, reverse its orientation, and unfold. This tumbling-through-folding dynamics is examined in terms of the stable configurations of the trumbbell and of the associated basins of attraction. The properties of the statistics of the tumbling times are explained by using the large deviations theory. In particular, the analysis of the tumbling statistics reveals a fundamental difference between the tumbling motion of a trumbbell in an extensional flow and the tumbling motion of an elastic dumbbell in a simple shear flow. In the

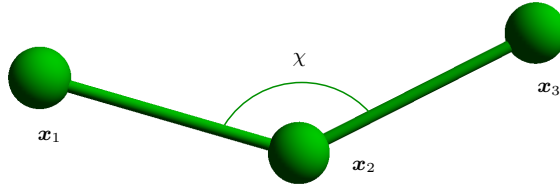


FIGURE 1.6. The trumbell model, consisting of three beads at $\mathbf{x}_1, \mathbf{x}_2, \mathbf{x}_3$ connected by two rigid rods. The internal angle between the rods is χ .

former case, indeed, the mean time that separates two reversals grows with the Weissenberg number, and moreover, this growth is exponential.

Section 1.2 describes the trumbell and its equations of motion. An alternative formulation of the trumbell in terms of its angles and a diffusion equation for its configuration is given in Sec. 1.3. Section 1.4 examines the stationary statistics of the configuration of a trumbell in a two-dimensional extensional flow. In particular, a linear stability analysis establishes the fixed points of the system. Section 1.5 analyses the tumbling motion and its statistical properties. Analogous results in three dimensions are also presented. Finally, concluding remarks and potential extensions of the work are given in Sec. 1.6.

1.2. The trumbell

A trumbell consists of three identical beads located at \mathbf{x}_ν ($\nu = 1, 2, 3$) and joined by two inertialess rods of length ℓ (see Fig. 1.6) [10, 46]. The rods connecting the beads are described by the vectors

$$\begin{aligned}\boldsymbol{\rho}_1 &= \mathbf{x}_1 - \mathbf{x}_2, \\ \boldsymbol{\rho}_3 &= \mathbf{x}_3 - \mathbf{x}_2.\end{aligned}\tag{1.2}$$

The internal angle between the rods is denoted by χ . In this chapter, the two configurations obtained by interchanging \mathbf{x}_1 and \mathbf{x}_3 are distinguished from each other, thus χ varies between 0 and 2π . When $\chi = 0, 2\pi$ the trumbell is folded; when $\chi = \pi$ it is fully extended. An elastic hinge at the middle models the entropic forces that oppose the bending of the trumbell. The force exerted by the hinge is described by a harmonic potential

$$\phi(\chi) = \frac{A}{2}(\chi - \pi)^2\tag{1.3}$$

for some non-negative constant A that represents the magnitude of the potential.

The trumbell is advected by a linear velocity field $\mathbf{u}(\mathbf{x}, t)$, in which each bead experiences Stokes' drag with drag coefficient ζ . The fluid is Newtonian. The beads are assumed to be sufficiently small for them to experience Brownian fluctuations and for the velocity gradient $\nabla\mathbf{u}$ to be spatially uniform across the trumbell. The inertia of the beads and the hydrodynamic interactions between them are disregarded [25, 62]. It is furthermore assumed that the trumbell does not modify the flow.

The position vectors of the beads satisfy the following evolution equations:

$$m\ddot{\mathbf{x}}_\nu = -\zeta[\dot{\mathbf{x}}_\nu - \mathbf{u}(\mathbf{x}_\nu, t)] + \mathbf{t}_\nu + \mathbf{f}_\nu + \sqrt{D}\boldsymbol{\eta}_\nu(t), \quad \nu = 1, 2, 3,\tag{1.4}$$

where m is the mass of each bead, $D = 2\zeta KT$ (K is the Boltzmann constant and T is temperature), and $\boldsymbol{\eta}_\nu(t)$ are independent d -dimensional white noises. The restoring forces \mathbf{f}_ν take the form (derivation in appendix 1.7.1):

$$\begin{aligned}\mathbf{f}_1 &= A_\chi (\hat{\boldsymbol{\rho}}_1 \cot \chi - \hat{\boldsymbol{\rho}}_3 \csc \chi), \\ \mathbf{f}_2 &= -(\mathbf{f}_1 + \mathbf{f}_3), \\ \mathbf{f}_3 &= A_\chi (\hat{\boldsymbol{\rho}}_3 \cot \chi - \hat{\boldsymbol{\rho}}_1 \csc \chi),\end{aligned}\tag{1.5}$$

with $A_\chi = A(\pi - \chi)/\ell$ and $\hat{\boldsymbol{\rho}}_i = \boldsymbol{\rho}_i/|\boldsymbol{\rho}_i|$. The tensions \mathbf{t}_ν keep the distances between the beads constant. The terms on the right hand side of Eq. (1.4) describe Stokes' drag, the rigidity of the rods, the resistance of the particle to bend, and Brownian noise, respectively. Neglecting inertial effects yields:

$$\dot{\mathbf{x}}_\nu = \mathbf{u}(\mathbf{x}_\nu, t) + \frac{1}{\zeta} \left[\mathbf{t}_\nu + \mathbf{f}_\nu + \sqrt{D} \boldsymbol{\eta}_\nu(t) \right], \quad \nu = 1, 2, 3.\tag{1.6}$$

In the following it will be useful to isolate the evolution of the internal configuration of the trumbbell from the motion of its centre of mass

$$\mathbf{x}_{\text{CM}} = \frac{\mathbf{x}_1 + \mathbf{x}_2 + \mathbf{x}_3}{3},\tag{1.7}$$

which evolves like a tracer owing to the linearity of the velocity field:

$$\dot{\mathbf{x}}_{\text{CM}} = \mathbf{u}(\mathbf{x}_{\text{CM}}, t) + \sqrt{\frac{D}{3}} \hat{\boldsymbol{\eta}}(t),\tag{1.8}$$

where $\hat{\boldsymbol{\eta}}(t)$ is white noise. In the reference frame of \mathbf{x}_{CM} the configuration of the trumbbell can be described by using the vectors $\boldsymbol{\rho}_1$ and $\boldsymbol{\rho}_3$ defined in Eq. (1.2) and which, from Eq. (1.6), satisfy the following differential equations:

$$\begin{aligned}\dot{\boldsymbol{\rho}}_1 &= \boldsymbol{\rho}_1 \cdot \nabla \mathbf{u} + \frac{1}{\zeta} (2\mathbf{t}_1 + \mathbf{t}_3) + \frac{1}{\zeta} (2\mathbf{f}_1 + \mathbf{f}_3) + \Gamma \tilde{\boldsymbol{\eta}}_1, \\ \dot{\boldsymbol{\rho}}_3 &= \boldsymbol{\rho}_3 \cdot \nabla \mathbf{u} + \frac{1}{\zeta} (2\mathbf{t}_3 + \mathbf{t}_1) + \frac{1}{\zeta} (2\mathbf{f}_3 + \mathbf{f}_1) + \Gamma \tilde{\boldsymbol{\eta}}_3,\end{aligned}\tag{1.9}$$

where $\Gamma = \sqrt{2D}/\zeta$ and $\tilde{\boldsymbol{\eta}}_i = [\boldsymbol{\eta}_i(t) - \boldsymbol{\eta}_2(t)]/\sqrt{2}$ with $\langle \tilde{\boldsymbol{\eta}}_i(t) \rangle = 0$ and $\langle \tilde{\eta}_i^\alpha(t) \tilde{\eta}_i^\beta(t') \rangle = \delta^{\alpha\beta} \delta(t - t')$, $i = 1, 3$. The tensions may be calculated explicitly by imposing the rigidity constraints $d|\boldsymbol{\rho}_i|^2/dt = 0$ or

$$\boldsymbol{\rho}_i \circ \dot{\boldsymbol{\rho}}_i = 0,\tag{1.10}$$

where the symbol 'o' indicates that the dot products involving the noise terms are understood in the Stratonovich sense [54] (see also appendix 1.7.2). Equations (1.10) form a linear system in the variables $|\mathbf{t}_1|$ and $|\mathbf{t}_3|$ (in terms of $\boldsymbol{\rho}_1, \boldsymbol{\rho}_3$) and yields:

$$\begin{aligned}\mathbf{t}_1 &= -\zeta c_\chi [2\sigma_1 - \sigma_3 \cos \chi - \tilde{A}_\chi + 2\Gamma(\hat{\boldsymbol{\rho}}_1 \circ \tilde{\boldsymbol{\eta}}_1) - \Gamma \cos \chi (\hat{\boldsymbol{\rho}}_3 \circ \tilde{\boldsymbol{\eta}}_3)] \hat{\boldsymbol{\rho}}_1, \\ \mathbf{t}_2 &= -(\mathbf{t}_1 + \mathbf{t}_3), \\ \mathbf{t}_3 &= -\zeta c_\chi [2\sigma_3 - \sigma_1 \cos \chi - \tilde{A}_\chi + 2\Gamma(\hat{\boldsymbol{\rho}}_3 \circ \tilde{\boldsymbol{\eta}}_3) - \Gamma \cos \chi (\hat{\boldsymbol{\rho}}_1 \circ \tilde{\boldsymbol{\eta}}_1)] \hat{\boldsymbol{\rho}}_3,\end{aligned}\tag{1.11}$$

where $\sigma_i = \sum_{\alpha, \beta} \ell \hat{\rho}_i^\alpha \partial^\alpha u^\beta \hat{\rho}_i^\beta$, $c_\chi = (4 - \cos^2 \chi)^{-1}$, and $\tilde{A}_\chi = \zeta^{-1} A_\chi \sin \chi (2 - \cos \chi)$. By substituting Eqs. (1.11) into Eqs. (1.9), the following system is obtained:

$$\begin{aligned}\dot{\boldsymbol{\rho}}_1 &= \mathbf{A}_1 + \mathcal{B}_{11} \circ \tilde{\boldsymbol{\eta}}_1(t) + \mathcal{B}_{13} \circ \tilde{\boldsymbol{\eta}}_3(t), \\ \dot{\boldsymbol{\rho}}_3 &= \mathbf{A}_3 + \mathcal{B}_{31} \circ \tilde{\boldsymbol{\eta}}_1(t) + \mathcal{B}_{33} \circ \tilde{\boldsymbol{\eta}}_3(t).\end{aligned}\tag{1.12}$$

The explicit forms of the vectors $\mathbf{A}_1, \mathbf{A}_3$ are:

$$\begin{aligned}\mathbf{A}_1 &= \boldsymbol{\rho}_1 \cdot \nabla \mathbf{u} - 2c_\chi \left[2\sigma_1 - \sigma_3 \cos \chi - \tilde{A}_\chi \right] \hat{\boldsymbol{\rho}}_1 \\ &\quad - c_\chi \left[2\sigma_3 - \sigma_1 \cos \chi - \tilde{A}_\chi \right] \hat{\boldsymbol{\rho}}_3 + \frac{1}{\zeta} (2\mathbf{f}_1 + \mathbf{f}_3), \\ \mathbf{A}_3 &= \boldsymbol{\rho}_3 \cdot \nabla \mathbf{u} - 2c_\chi \left[2\sigma_3 - \sigma_1 \cos \chi - \tilde{A}_\chi \right] \hat{\boldsymbol{\rho}}_3 \\ &\quad - c_\chi \left[2\sigma_1 - \sigma_3 \cos \chi - \tilde{A}_\chi \right] \hat{\boldsymbol{\rho}}_1 + \frac{1}{\zeta} (2\mathbf{f}_3 + \mathbf{f}_1),\end{aligned}$$

and the matrix-valued coefficients of the noises are

$$\begin{aligned}\mathcal{B}_{11} &= \Gamma [\mathbb{I} + c_\chi (\hat{\boldsymbol{\rho}}_3 \cos \chi - 4\hat{\boldsymbol{\rho}}_1) \otimes \hat{\boldsymbol{\rho}}_1], \\ \mathcal{B}_{13} &= 2\Gamma c_\chi (\hat{\boldsymbol{\rho}}_1 \cos \chi - \hat{\boldsymbol{\rho}}_3) \otimes \hat{\boldsymbol{\rho}}_3, \\ \mathcal{B}_{31} &= 2\Gamma c_\chi (\hat{\boldsymbol{\rho}}_3 \cos \chi - \hat{\boldsymbol{\rho}}_1) \otimes \hat{\boldsymbol{\rho}}_1, \\ \mathcal{B}_{33} &= \Gamma [\mathbb{I} + c_\chi (\hat{\boldsymbol{\rho}}_1 \cos \chi - 4\hat{\boldsymbol{\rho}}_3) \otimes \hat{\boldsymbol{\rho}}_3],\end{aligned}$$

where \mathbb{I} is the identity matrix and \otimes denotes the tensor product. The internal angle χ can be obtained from $\boldsymbol{\rho}_1 \cdot \boldsymbol{\rho}_3 = \ell^2 \cos \chi$. This formulation holds both for $d = 2$ and for $d = 3$ dimensions. It will be used later for numerical simulations, especially for the $d = 3$ case.

1.3. The angular formulation of the trumbbell

An alternative formulation for the evolution of the trumbbell can be obtained by expressing its configuration in terms of angular variables. In the reference frame of the centre of mass \mathbf{x}_{CM} , the configuration of the trumbbell can be described by $2(d-1)$ angular coordinates \mathbf{q} , where d is the dimension of the flow [10, 46]. For $d = 2$, $\mathbf{q} = (\theta, \chi)$ where χ is again the internal angle and $0 \leq \theta < 2\pi$ gives the orientation of the rod $\boldsymbol{\rho}_3 = \mathbf{x}_3 - \mathbf{x}_2$ with respect to a fixed frame of reference. For $d = 3$, $\mathbf{q} = (\alpha, \beta, \gamma, \chi)$ where $0 \leq \alpha < 2\pi$, $0 \leq \beta < \pi$ and $0 \leq \gamma < 2\pi$ are the Euler angles that specify the orientation of the orthogonal triad $(\mathbf{x}_3 - \mathbf{x}_1) \wedge (\mathbf{x}_2 - \mathbf{x}_{\text{CM}})$, $\mathbf{x}_3 - \mathbf{x}_1$, $\mathbf{x}_2 - \mathbf{x}_{\text{CM}}$ with respect to a fixed coordinate system.

Let us denote the separation vectors describing the location of the beads with respect to \mathbf{x}_{CM} as

$$\mathbf{r}_\nu = \mathbf{x}_\nu - \mathbf{x}_{\text{CM}}. \quad (1.13)$$

The statistics of the configuration of the trumbbell at a time t is specified by the probability density function (PDF) $\Psi(\mathbf{q}; t)$, which is normalised as $\int \Psi(\mathbf{q}; t) d\mathbf{q} = 1$ and satisfies the following diffusion equation [46] (see also Ref. [10] for the derivation.):

$$\frac{\partial \Psi}{\partial t} = -\frac{\partial}{\partial q^i} \left\{ \mathcal{G}^{ij} \left[\left(\kappa^{kl}(t) r_\nu^l \frac{\partial r_\nu^k}{\partial q^j} - \frac{1}{\zeta} \frac{\partial \phi}{\partial q^j} \right) \Psi - \frac{KT}{\zeta} \sqrt{h} \frac{\partial}{\partial q^j} \left(\frac{\Psi}{\sqrt{h}} \right) \right] \right\}, \quad (1.14)$$

where $\kappa^{kl}(t) = \partial^l u^k(t)$ is the velocity gradient evaluated at \mathbf{x}_{CM} , $h = \det(\mathcal{H})$ with

$$\mathcal{H}^{ij} = \frac{\partial r_\nu^k}{\partial q^i} \frac{\partial r_\nu^k}{\partial q^j} \quad \text{and} \quad \mathcal{G} = \mathcal{H}^{-1}. \quad (1.15)$$

Note that in a linear flow the orientational dynamics of the trumbbell only depends on the velocity gradient which is spatially uniform. The internal configuration of the trumbbell is therefore decoupled from the position of the centre of mass. This

implies that the statistics of the angular variables \mathbf{q} is independent of \mathbf{x}_{CM} . Hence, without any loss of generality, the dynamics of the trumbbell is studied in the frame of reference that is translated with the centre of mass. Also note that the stationary PDF of \mathbf{q} , $\Psi_{\text{st}}(\mathbf{q})$, takes the form

$$\Psi_{\text{st}}(\mathbf{q}) = J\psi_{\text{st}}(\mathbf{q}), \quad (1.16)$$

where J is proportional to the Jacobian of the transformation from the \mathbf{r}_ν to the \mathbf{q} coordinates; $J = 1$ for $d = 2$ and $J = \sin \chi \sin \beta$ for $d = 3$. Details for calculating these Jacobian may be found in Sec. 2.6.3.

In the absence of both the flow gradient ($\boldsymbol{\kappa} = 0$) and the restoring potential ($A = 0$), the stationary PDF takes the form [46]

$$\psi_{\text{st}}(\mathbf{q}) = \psi_0(\chi) \quad (1.17)$$

with

$$\psi_0(\chi) \propto \sqrt{4 - \cos^2 \chi}, \quad (1.18)$$

which shows that the stationary PDF depends only on the bending angle χ . In this case, the configuration with the rods being perpendicular ($\chi = \pi/2$) has slightly greater probability than the other configurations, while the folded ($\chi = 0$) and the extended ($\chi = \pi$) configurations are equally probable. The restoring potential breaks this symmetry. For $A \neq 0$, then [46]

$$\psi_{\text{st}}(\chi) \propto \psi_0(\chi) \exp \left[-\frac{Z}{2}(\chi - \pi)^2 \right], \quad (1.19)$$

where $Z \equiv A/KT$ is a stiffness parameter that compares the amplitude of the restoring potential to that of the thermal fluctuations (recall that K is the Boltzmann constant and T is temperature). The extended configuration $\chi = \pi$ is evidently the most probable one, and its probability increases as Z increases. The plots of ψ_{st} are given in Fig. 1.7. Evidently, when the trumbbell is introduced in a non-uniform flow ($\boldsymbol{\kappa} \neq 0$) its dynamics results from the interplay between the restoring elastic force and the deformation caused by the flow.

The results on the stationary PDF of χ are not the only advantages of considering angular variables. It is practical especially for the case $d = 2$ for two more reasons: first a stability analysis can be carried out in two variables θ, χ instead of four (each component of the rods $\boldsymbol{\rho}_1, \boldsymbol{\rho}_3$) and consequently only two variables will be evolved when numerical simulations would eventually be performed.

To study the dynamics of the trumbbell, it is useful to rewrite the diffusion equation (1.14) as a Fokker–Planck equation (FPE), which is associated to a stochastic differential equation on the variable \mathbf{q} . The FPE is a differential equation of the form

$$\frac{\partial \Psi}{\partial t} = -\frac{\partial}{\partial q^i} (V^i \Psi) + \frac{1}{2} \frac{\partial^2}{\partial q^i \partial q^j} (D^{ij} \Psi), \quad (1.20)$$

from which we obtain the drift and diffusion coefficients V^i and D^{ij} , respectively. The associated system of Itô stochastic differential equations (SDEs) to this FPE (1.20) is then given by:

$$dq^i = V^i dt + \tilde{D}^{ij} dW^j(t) \quad (1.21)$$

where $\tilde{D}\tilde{D}^\top = D$ and $dW^j(t)$ are independent Brownian motions. Note that the choice of \tilde{D} is not unique. It is also remarked that if the flow is random, the velocity gradient $\boldsymbol{\kappa}$ in Eq. (1.14) will have a noise term associated to it and the desired

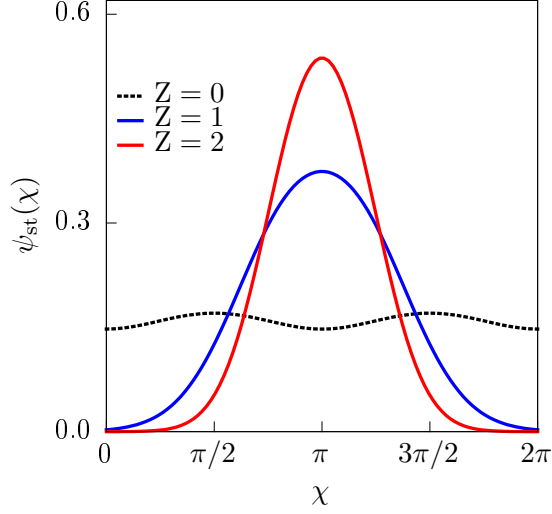


FIGURE 1.7. The stationary PDF $\psi_{\text{st}}(\chi)$ in the absence of flow for different values of the stiffness parameter Z . The black dotted line represents the PDF in the absence of a restoring potential.

PDF would have to be averaged over its realizations (a diffusion equation taking a stochastic gradient into consideration is derived in Chap. 2).

In the following subsections, the explicit expressions of the coefficients appearing in the diffusion equation (1.14) and, for the two-dimensional case, the coefficients of the associated FPE, are provided.

1.3.1. Two dimensions. As discussed at the beginning of this section, the angular variables describing the trumbell in two dimensions are $\mathbf{q} = (\theta, \chi)$, where χ is the internal angle and $0 \leq \theta < 2\pi$ is the angle that the vector $\boldsymbol{\rho}_3 = \mathbf{x}_3 - \mathbf{x}_2$ makes with the \mathbf{x} -axis on some fixed frame of reference (see Fig. 1.8). The separation vectors \mathbf{r}_ν defined in Eq. (1.13) can then be expressed in terms of θ and χ as

$$\begin{aligned} \mathbf{r}_1 &= \frac{\ell}{3} (2 \cos(\theta + \chi) - \cos(\theta), 2 \sin(\theta + \chi) - \sin(\theta)), \\ \mathbf{r}_2 &= -\frac{\ell}{3} (\cos(\theta + \chi) + \cos(\theta), \sin(\theta + \chi) + \sin(\theta)), \\ \mathbf{r}_3 &= \frac{\ell}{3} (2 \cos(\theta) - \cos(\theta + \chi), 2 \sin(\theta) - \sin(\theta + \chi)). \end{aligned}$$

The other coefficients in the diffusion equation are then derived as $h = \ell^4(4 - \cos^2 \chi)/9$ and (see Eq. (1.15) for the definition)

$$\mathcal{G} = \frac{1}{\ell^2} \begin{pmatrix} \frac{6}{4 - \cos^2 \chi} & -\frac{3}{2 + \cos \chi} \\ -\frac{3}{2 + \cos \chi} & \frac{6}{2 + \cos \chi} \end{pmatrix}.$$

The FPE (1.20) in two variables can then be written with its coefficients as

$$V^\theta = -\frac{6KT \sin \chi}{\zeta \ell^2 (2 - \cos \chi)(2 + \cos \chi)^2} - \frac{3A(\pi - \chi)}{\zeta \ell^2 (2 + \cos \chi)} - \frac{1}{4 - \cos^2 \chi} \times$$

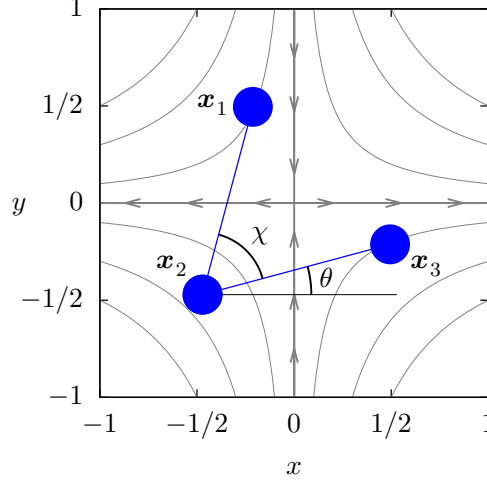


FIGURE 1.8. A trumbbell in the frame of reference of its centre of mass. The origin coincides with the centre of mass. The flow is extensional (streamlines shown in gray) with stretching in the x direction and compression in the y direction.

$$\begin{aligned} & \{ [2 \sin \chi \cos^2(\theta + \chi) + \cos \theta (4 \sin \theta - \cos \chi \sin(\theta + \chi))] \kappa^{11}(t) + \\ & [2 \cos \chi \sin^2(\theta + \chi) - \sin \theta (2 + \cos \chi) \sin(\theta + \chi) + 4 \sin^2 \theta] \kappa^{12}(t) + \\ & [-2 \cos \chi \cos^2(\theta + \chi) + \cos \theta (2 + \cos \chi) \cos(\theta + \chi) - 4 \cos^2 \theta] \kappa^{21}(t) + \\ & [2 \cos \theta (\sin(\theta + \chi) - 2 \sin \theta) + \cos \chi (\sin \theta \cos(\theta + \chi) - \sin(2(\theta + \chi)))] \kappa^{22}(t) \}, \end{aligned}$$

$$V^x = \frac{12KT \sin \chi}{\zeta \ell^2 (2 - \cos \chi)(2 + \cos \chi)^2} + \frac{6A(\pi - \chi)}{\zeta \ell^2 (2 + \cos \chi)} + \frac{\sin \chi}{2 + \cos \chi} \{ [1 - 2 \cos(2\theta + \chi)] \times \kappa^{11}(t) - 2 \sin(2\theta + \chi) [\kappa^{12}(t) + \kappa^{21}(t)] + [1 + 2 \cos(2\theta + \chi)] \kappa^{22}(t) \}.$$

and

$$D^{\theta\theta} = \frac{12KT}{\zeta \ell^2 (4 - \cos^2 \chi)}, \quad D^{\theta\chi} = -\frac{6KT}{\zeta \ell^2 (2 + \cos \chi)}, \quad D^{\chi\chi} = \frac{12KT}{\zeta \ell^2 (2 + \cos \chi)}.$$

The associated system of Itô SDEs (1.21) in the case $d = 2$ is then given by:

$$\begin{aligned} \dot{\theta}(t) &= V^\theta + \sqrt{D^{\theta\theta}} \xi_\theta(t), \\ \dot{\chi}(t) &= V^\chi + \frac{D^{\theta\chi}}{\sqrt{D^{\theta\theta}}} \xi_\theta(t) + \sqrt{D^{\chi\chi} - \frac{(D^{\theta\chi})^2}{D^{\theta\theta}}} \xi_\chi(t), \end{aligned} \tag{1.22}$$

where $\xi_\theta(t)$ and $\xi_\chi(t)$ are independent white noises. Note that in Eqs. (1.22) $D^{\chi\chi} - (D^{\theta\chi})^2/D^{\theta\theta} = 3KT/\zeta \ell^2$.

1.3.2. Three dimensions. For $d = 3$, the configuration is given by four angles $\mathbf{q} = (\alpha, \beta, \gamma, \chi)$ where the first three are the Euler angles and χ is again the internal angle as defined in Sec. 1.3. It would be convenient to work in the frame of reference that follows the trumbbell, i.e. with trumbbell's centre of mass at its origin. In particular, this transformation from a fixed frame of reference \mathbf{x}, \mathbf{y} and \mathbf{z} to the new set of axes $\mathbf{x}' = (\mathbf{x}_3 - \mathbf{x}_1) \wedge (\mathbf{x}_2 - \mathbf{x}_{\text{CM}})$, $\mathbf{y}' = \mathbf{x}_3 - \mathbf{x}_1$, and $\mathbf{z}' = \mathbf{x}_2 - \mathbf{x}_{\text{CM}}$ keeps the

rods of the trumbbell $\boldsymbol{\rho}_1 = \mathbf{x}_1 - \mathbf{x}_2$, $\boldsymbol{\rho}_3 = \mathbf{x}_3 - \mathbf{x}_2$ in the $\mathbf{y}'\text{-}\mathbf{z}'$ plane:

$$\begin{aligned}\boldsymbol{\rho}_1 &= \ell \left[\cos\left(\frac{\chi}{2}\right) \mathbf{z}' - \sin\left(\frac{\chi}{2}\right) \mathbf{y}' \right], \\ \boldsymbol{\rho}_3 &= \ell \left[\cos\left(\frac{\chi}{2}\right) \mathbf{z}' + \sin\left(\frac{\chi}{2}\right) \mathbf{y}' \right].\end{aligned}$$

The transformation is given by the matrix $\Sigma :=$

$$\begin{pmatrix} \cos\alpha \cos\beta \cos\gamma - \sin\alpha \sin\gamma & \sin\alpha \cos\beta \cos\gamma + \cos\alpha \sin\gamma & -\sin\beta \cos\gamma \\ -\cos\alpha \cos\beta \cos\gamma - \sin\alpha \sin\gamma & -\sin\alpha \cos\beta \cos\gamma + \cos\alpha \sin\gamma & \sin\beta \sin\gamma \\ \cos\alpha \sin\beta & \sin\alpha \sin\beta & \cos\beta \end{pmatrix};$$

and the separation vectors (see Eq. (1.13)) can then be written as

$$\begin{aligned}\mathbf{r}_1 &= \frac{\ell}{3} (2\boldsymbol{\rho}_1 - \boldsymbol{\rho}_3), \\ \mathbf{r}_2 &= -\frac{\ell}{3} (\boldsymbol{\rho}_1 + \boldsymbol{\rho}_3), \\ \mathbf{r}_3 &= \frac{\ell}{3} (2\boldsymbol{\rho}_3 - \boldsymbol{\rho}_1).\end{aligned}$$

The other coefficients in the diffusion equation (1.14) may now be obtained for the case $d = 3$, in particular, the matrix \mathcal{G} and the determinant h of \mathcal{G}^{-1} . These results may be found in Refs. [10, 46]:

$$\begin{aligned}\mathcal{G}^{11} &= \frac{3(-3 \cos 2\gamma (\cos \chi - 1) + \cos \chi - 5) \csc^2 \beta \sec^2\left(\frac{\chi}{2}\right)}{8\ell^2(\cos \chi - 2)} \\ \mathcal{G}^{12} &= \frac{9 \cos \gamma \csc \beta \sin \gamma \tan^2\left(\frac{\chi}{2}\right)}{2\ell^2(2 - \cos \chi)} = \mathcal{G}^{21} \\ \mathcal{G}^{13} &= \frac{3(3 \cos 2\gamma (\cos \chi - 1) - \cos \chi + 5) \cot \beta \csc \beta \sec^2\left(\frac{\chi}{2}\right)}{8\ell^2(\cos \chi - 2)} = \mathcal{G}^{31} \\ \mathcal{G}^{22} &= \frac{3(-6 \cos^2 \gamma \sec^2\left(\frac{\chi}{2}\right) + 3 \cos 2\gamma + 1)}{4\ell^2(\cos \chi - 2)} \\ \mathcal{G}^{23} &= \frac{9 \cot \beta \sin 2\gamma \tan^2\left(\frac{\chi}{2}\right)}{4\ell^2(\cos \chi - 2)} = \mathcal{G}^{32} \\ \mathcal{G}^{33} &= \left\{ 9 \sin^2 \beta \sin^2 2\gamma \sin^4\left(\frac{\chi}{2}\right) - [3 \cos 2\gamma (\cos \chi - 1) - \cos \chi + 5] \times \right. \\ &\quad \left. \left[\cos^2\left(\frac{\chi}{2}\right) \sin^2 \beta + 3 (\cos^2 \gamma + \cos^2 \beta \sin^2 \gamma) \sin^2\left(\frac{\chi}{2}\right) \right] \right\} \times \\ &\quad [2\ell^2(\cos \chi - 2) \sin^2 \beta \sin^2 \chi]^{-1} \\ \mathcal{G}^{44} &= \frac{6}{\ell^2(\cos \chi + 2)} \\ \mathcal{G}^{14} &= \mathcal{G}^{24} = \mathcal{G}^{34} = \mathcal{G}^{41} = \mathcal{G}^{42} = \mathcal{G}^{43} = 0\end{aligned}$$

and $h = -\frac{1}{54} \ell^8 \sin^2 \beta \sin^2 \chi (\cos 2\chi - 7)$. These expressions will be useful in Chap. 3, where analytical expressions of the PDFs of the trumbbell will be derived. It would be further possible to calculate the expressions of the drift and diffusion coefficients V^i and D^{ij} in the FPE (1.20) and the associated SDEs (1.21) for the $d = 3$ case. They are however not reported as they will not be used in the stability analysis nor in the subsequent numerical simulations. In fact, the angular formulation in the case

$d = 3$ is not suitable for simulations since, for instance, \mathcal{G}^{33} blows up to infinity as $\beta \rightarrow 0$ or $\chi \rightarrow 0$.

1.4. Stationary statistics in the extensional flow

The goal of this chapter is to study if a trumbbell performs an end-to-end reversal in an extensional flow. The existence of any tumbling requires a configuration from which a trumbbell may tumble from and another configuration to which it tumbles to. In this section, the stationary configurations of the trumbbell in an extensional flow is studied. In particular, stable fixed points of the system will be identified. From this point the angular formulation given in Sec. 1.3 is assumed unless otherwise indicated.

It is convenient to formulate the equations (such as Eqs. (1.22)) in terms of two dimensionless parameters: the stiffness parameter (already used and defined in Eq. (1.19))

$$Z = \frac{A}{KT} \quad (1.23)$$

and the Weissenberg number

$$Wi = \frac{\lambda\zeta\ell^2}{A}, \quad (1.24)$$

where λ is the magnitude of the velocity gradient. The latter compares the strengths of the flow and of the restoring force. In addition, the Péclet number is also introduced

$$Pe = \frac{\lambda\zeta\ell^2}{KT} = Z Wi, \quad (1.25)$$

which is the relative intensity of the flow to Brownian noise.

To simplify the stability analysis and study the existence of tumbling, first consider a two-dimensional flow (tumbling in a three-dimensional planar extensional flow will be considered in Sec. 1.5.2). This assumption is valid if the trumbbell is immersed in a thin layer of fluid, for instance, in microfluidic experiments. Consider the extensional flow

$$\mathbf{u}(x, y) = \lambda(x, -y), \quad \lambda > 0, \quad (1.26)$$

which consists of a stretching direction \mathbf{x} and a compressing direction \mathbf{y} (Fig. 1.8). For this flow, the stationary PDF of θ and χ takes the form

$$\psi_{\text{st}}(\theta, \chi) \propto \sqrt{h} \exp \left[\frac{\Phi - \phi}{KT} \right] \quad (1.27)$$

with $\Phi = (\zeta/2)\kappa^{ij}r_\nu^i r_\nu^j$ [46]. Its explicit expression is:

$$\psi_{\text{st}}(\theta, \chi) \propto \sqrt{4 - \cos^2 \chi} \exp \left[\frac{Z Wi(2 \cos \chi - 1) \cos(2\theta + \chi)}{3} - \frac{Z(\pi - \chi)^2}{2} \right]. \quad (1.28)$$

The contour plot of $\ln \psi_{\text{st}}(\theta, \chi)$ is shown in Fig. 1.9 for representative values of Z and Wi . It is easily shown that the maxima of $\psi_{\text{st}}(\theta, \chi)$ are located at $P_\pi : (\theta = n\pi, \chi = \pi)$, where n is an integer. Hence, the trumbbell spends most of the time in an extended configuration and oriented in the stretching direction of the flow. The peaks at P_π become narrower as Wi increases, showing stronger preference for these configurations (see the marginal PDF of θ , $\psi_{\text{mar}}(\theta)$ in Fig. 1.10). Also note that these peaks are not symmetrically distributed around P_π in Fig. 1.9.

1.4.1. Stability analysis without restoring potential. To understand the behaviour of $\psi_{\text{st}}(\theta, \chi)$ when the flow is much stronger than both the restoring force

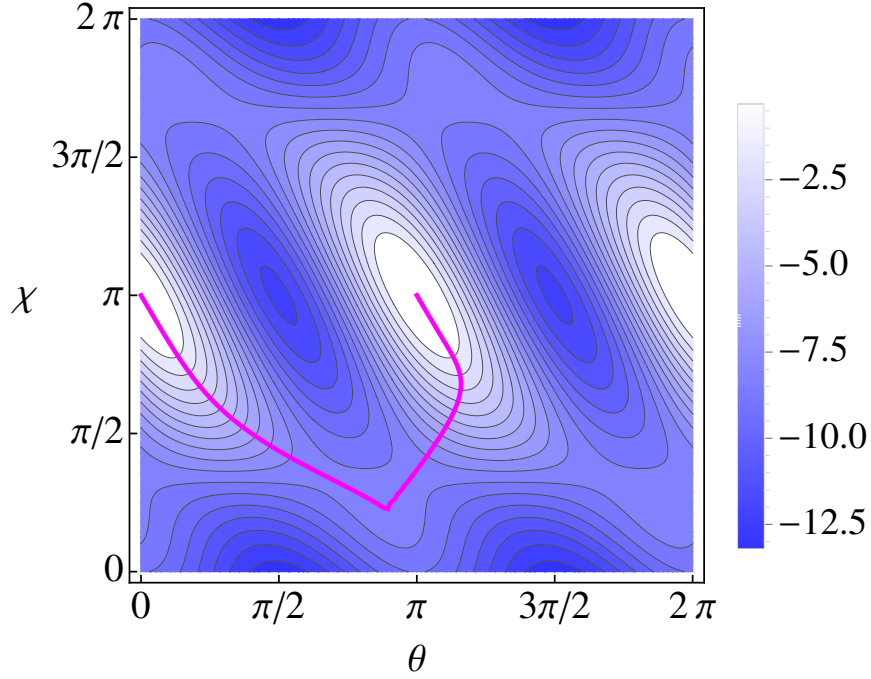


FIGURE 1.9. Contourplot of $\ln \psi_{\text{st}}(\theta, \chi)$ for $Z = 1$ and $Wi = 6$. One minimum energy path (see Sec. 1.5) connecting (π, π) and $(0, \pi)$ is drawn with a solid magenta curve.

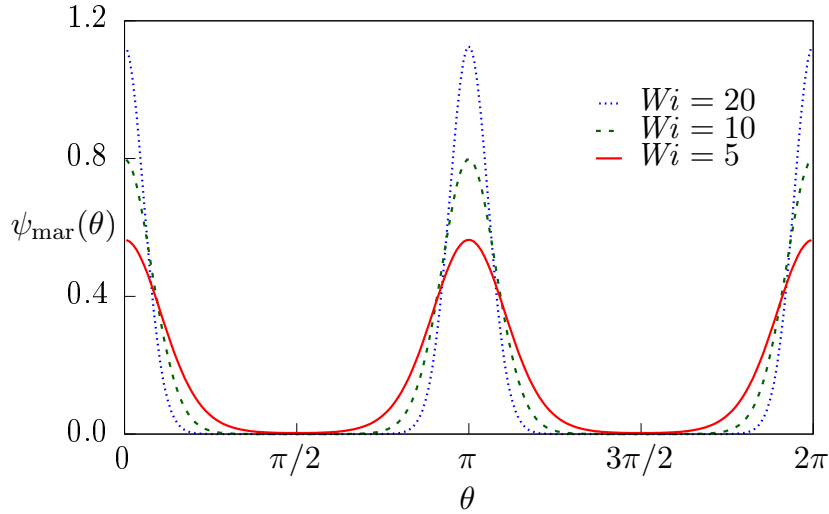


FIGURE 1.10. The marginal PDF $\psi_{\text{mar}}(\theta)$ of θ for $Z = 1$ and $Wi = 5$ (red, solid), $Wi = 10$ (green, dashed), and $Wi = 20$ (blue, dotted).

and Brownian noise, set $A = 0$ and $KT = 0$ in Eqs. (1.22), which corresponds to considering the limiting case $Wi = Pe = \infty$. The resulting system is:

$$\begin{aligned} \dot{\theta}(t) &= -\frac{\lambda}{2(4 - \cos^2 \chi)} [7 \sin(2\theta) + 4 \cos(2\theta + \chi) \sin \chi - \sin(2(\theta + \chi))], \\ \dot{\chi}(t) &= -\frac{4\lambda}{2 + \cos \chi} [\sin \chi \cos(2\theta + \chi)]. \end{aligned} \quad (1.29)$$

The linear stability analysis of this system yields two stable configurations, both aligned with the stretching direction of the flow ($\theta = 0, \pi, 2\pi$):

- (1) The extended configuration $P_\pi : (\theta = n\pi, \chi = \pi)$ with two negative eigenvalues: $\mu_\pi^{(1)} = -4\lambda, \mu_\pi^{(2)} = -2\lambda$.
- (2) The folded configuration $P_0 : (\theta = n\pi, \chi = 0, 2\pi)$ with two negative eigenvalues $\mu_0^{(1)} = -2\lambda, \mu_0^{(2)} = -4\lambda/3$.

As the velocity gradient λ becomes stronger, both configurations become increasingly stable, since the eigenvalues are proportional to λ . However, the ratio of the most negative eigenvalues of the two configurations is $\mu_\pi^{(1)}/\mu_0^{(1)} = 2$; hence the extended configuration P_π is more stable than the folded one P_0 for all λ and is expected to dominate the long-time statistics. This fact can be understood by noting that the velocity of a bead is proportional to its distance from the center of mass, and in the extended configuration P_π the end beads are farther from \mathbf{x}_{CM} than they are in the folded configuration P_0 . The presence of the two stable configurations is seen in the vector plot of $(\dot{\theta}, \dot{\chi})$ shown in Fig. 1.11.

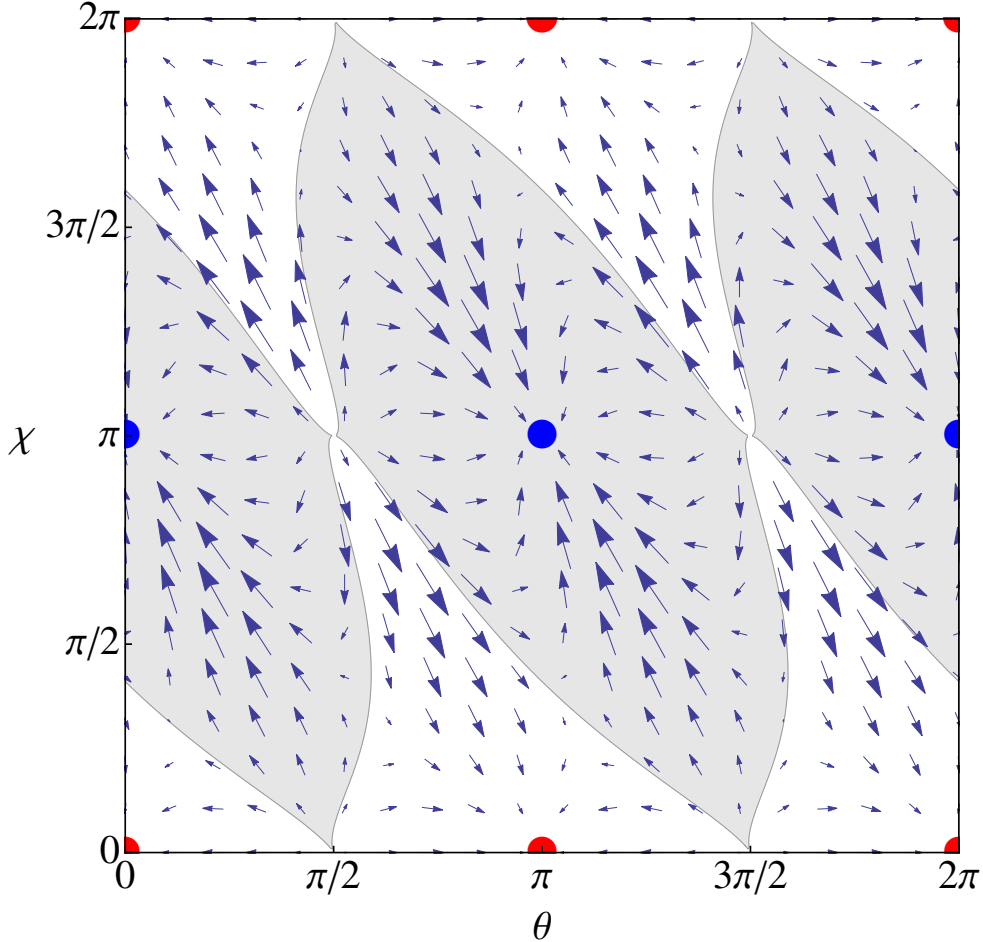


FIGURE 1.11. Vector plot of $\lambda^{-1}(\dot{\theta}, \dot{\chi})$ for $Wi = Pe = \infty$. The size of the arrows are proportional to the magnitude of the vector $\lambda^{-1}(\dot{\theta}, \dot{\chi})$. The basins of attraction of P_π (blue disks) are in gray; those of P_0 (red disks) are in white.

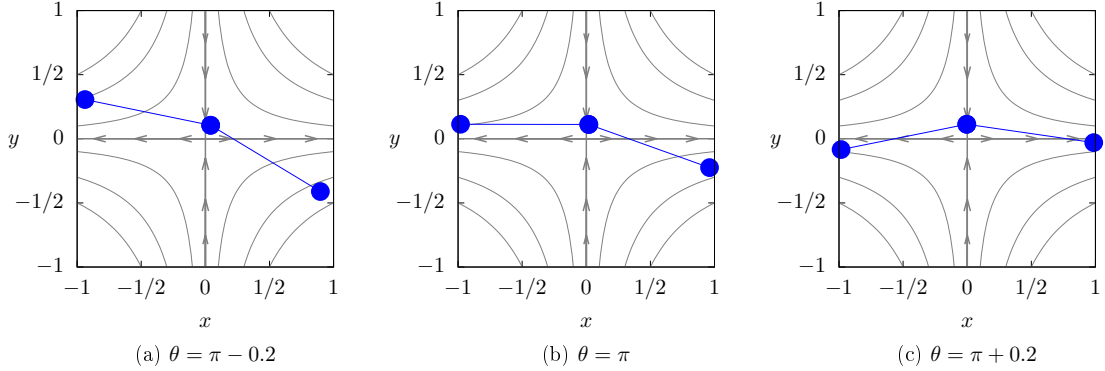


FIGURE 1.12. Three configurations near an extended equilibrium configuration for the same value of $\chi = 2.8$.

As both $\dot{\theta}$ and $\dot{\chi}$ are proportional to λ (see Eqs. (1.29)), the geometrical structure of the vector plot does not change with λ . In accordance with the stability analysis of the fixed points of Eqs. (1.29), the vectors that lie in the neighbourhood of P_π are larger than those in the neighbourhood of P_0 . Therefore, the presence of Brownian noise allows an easier escape from the basin of attraction of the folded configuration P_0 than from that of the extended configuration P_π . Conversely, a trumbbell in an extended configuration is more likely to remain in the basin of attraction of this configuration, until there is sufficient noise for it to fold. Also note that the basin of attraction of the points P_π is not symmetrically distributed around them, but there is a preferential direction along which the system is more strongly attracted (see Fig. 1.11). Consider indeed two configurations with the same value of χ close to π and with θ either slightly less than π or slightly greater than it (see Fig. 1.12). It is clear that the latter configuration is more strongly attracted to P_π .

1.4.2. Stability analysis in the presence of a restoring potential. In the presence of a restoring potential ($Wi < \infty, Pe = \infty$), the fixed points of system (1.22) and their stability can be calculated numerically. Only P_π remain stable fixed points; the configurations P_0 are no longer fixed because of the restoring potential. However, if the flow is sufficiently strong ($Wi \gtrsim 4$ for $Z = 1$), there exist stable points $P_\star : (\theta_\star, \chi_\star)$ that approach P_0 as Wi increases (see Fig. 1.13 and Fig. 1.14, left). Moreover, the points P_π are more stable than P_\star for all λ and as Wi increases, the eigenvalues of P_π and P_\star approach the corresponding eigenvalues of the $Wi = \infty$ case (see Fig. 1.14, right). Finally, the basins of attraction of P_π and P_\star have similar structures to those of P_π and P_0 when Wi is infinite (see Figs. 1.11 and 1.13). These results indicate that the intuition gained from the study of the $Wi = \infty$ case holds true also for $Wi < \infty$. In particular, the stability analysis of the fixed points explains why $\psi_{\text{st}}(\theta, \chi)$ shows high peaks only at the extended configuration P_π and not at the folded configuration (see Fig. 1.9). Furthermore, the examination of the basins of attraction of P_π and of the vector field $(\dot{\theta}, \dot{\chi})$ clarifies the shape of these peaks.

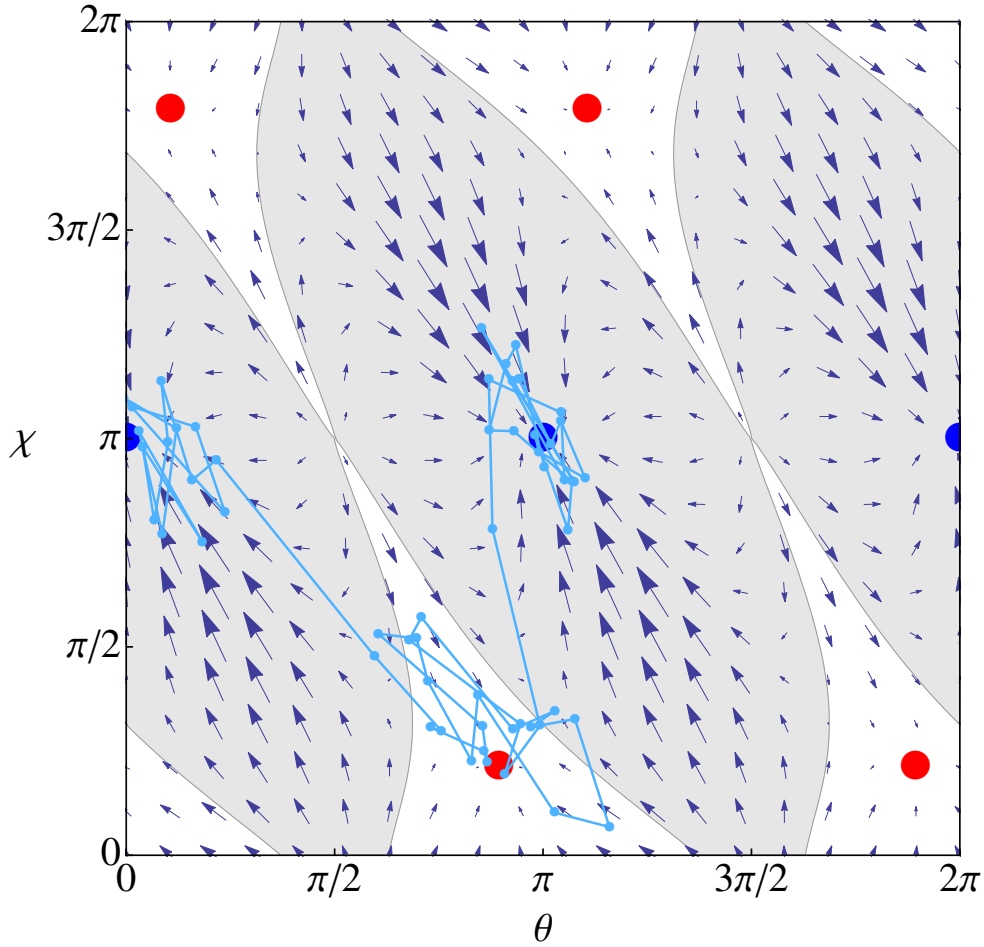


FIGURE 1.13. Vector plot of $(\dot{\theta}, \dot{\chi})$ for $Z = 1$, $Wi = 6$. The white areas are now the basins of attraction of P_* (red disks). The light blue curve with markers is a trajectory $(\theta(t), \chi(t))$ corresponding to a tumbling motion from $\theta = \chi = \pi$ to $\theta = 0, \chi = \pi$ (see Sec. (1.5)).

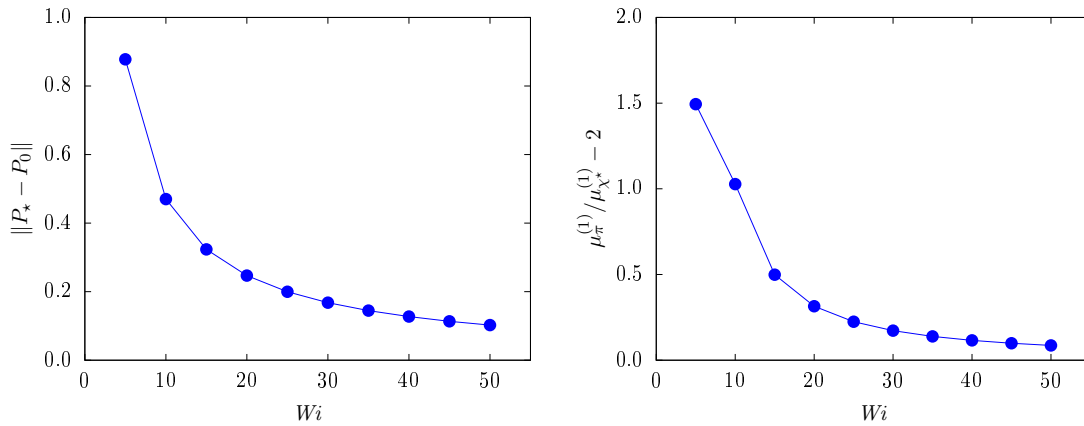


FIGURE 1.14. Left: Distance of a stable fixed point P_* from the nearest P_0 for $Pe = \infty$ as a function of Wi . Right: Ratio of the most negative eigenvalue of P_π to that of P_* subtracted by $\mu_\pi^{(1)}/\mu_*^{(1)} = 2$.

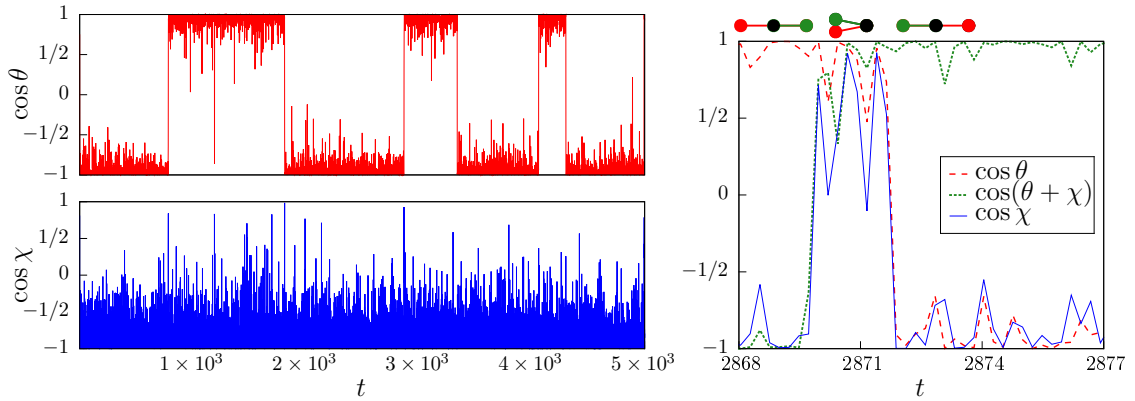


FIGURE 1.15. Time series of $\cos\theta(t)$ (left, top) and $\cos\chi(t)$ (left, bottom) for a two-dimensional extensional flow with $Z = 1$, $Wi = 6$. Right: zoom of the time series of $\cos\theta$, $\cos\chi$, $\cos(\theta + \chi)$ over a tumbling event.

1.5. Tumbling dynamics

The analysis of the fixed points and their basins of attraction in the preceding section opens the possibility of the existence of tumbling in extensional flows. In the (θ, χ) phase space, a tumbling manifests through a trajectory from one basin of attraction of P_π to another. Indeed, for sufficiently large Wi , the trumbbell is trapped in the basin of attraction of one of the extended configuration P_π for a long time. However, Brownian fluctuations may occasionally make it tumble between the aligned configuration ($\theta = 0, 2\pi$) and the anti-aligned one ($\theta = \pi$). To investigate this phenomenon, numerical simulations of Eqs. (1.22) were performed by using the Euler–Maruyama scheme with a time step $dt = 10^{-3}$ (a brief description of the numerical scheme can be found in appendix 1.7.3 of this chapter) [54]. Numerical simulations with smaller time steps were performed to confirm the accuracy of the results. The inspection of a representative time series of $\cos\theta(t)$ and $\cos\chi(t)$ confirms the aforementioned tumbling dynamics and shows that these reversals are characterised by partial folding (see Fig. 1.15). A typical trajectory in the (θ, χ) phase space is shown in Fig. 1.13. The trumbbell is initially extended and anti-aligned with the stretching direction. A favourable sequence of Brownian fluctuations makes it exit from the initial basin of attraction and pass through that of the folded configuration. The trumbbell then unfolds towards the extended but aligned configuration. A movie, provided as a supplementary material of Ref. [77] (also available in <http://math.unice.fr/~elcplan/tumbling.avi>), further illustrates this tumbling-through-folding motion.

Although the trumbbell always folds (possibly not completely) during a tumbling event, there are instances in which folding does not result in a reversal and the trumbbell rapidly unfolds back into the original configuration (see for instance Fig. 1.15 at $t \approx 1.2 \times 10^3$). In order to correctly identify a tumbling event, the following criterion is applied. Suppose that at time t_1 the trumbbell is sufficiently extended, i.e.

$$|\cos\theta| > 1 - \epsilon, \quad |\cos(\theta + \chi)| > 1 - \epsilon, \quad \cos\theta \cos(\theta + \chi) < 0 \quad (1.30)$$

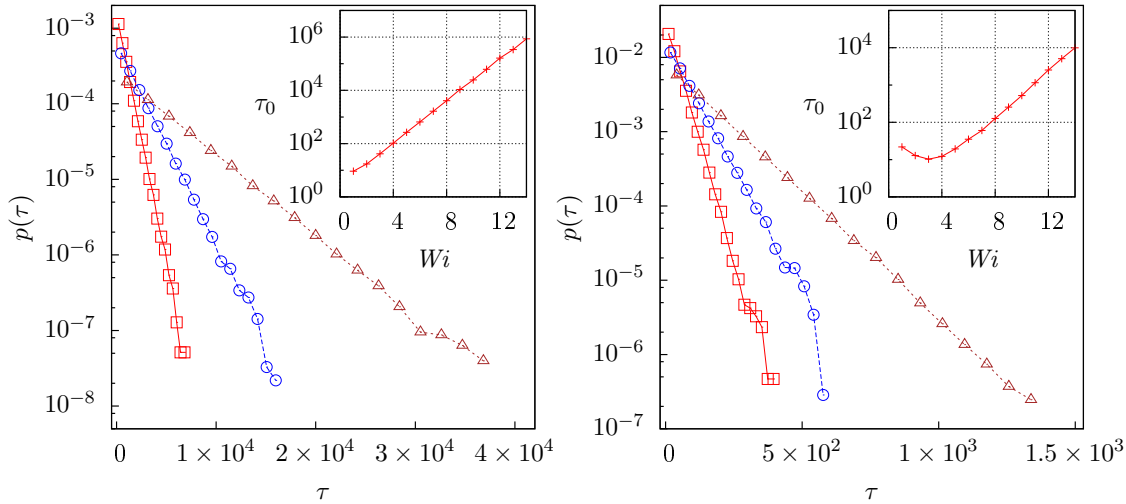


FIGURE 1.16. PDFs of the tumbling time in two dimensions (left) and three dimensions (right) for $Z = 1$ and $Wi = 6$ (red squares), $Wi = 7$ (blue circles), and $Wi = 8$ (brown triangles). The insets show τ_0 as a function of Wi .

for some small ϵ . A tumbling then occurs at time t_2 if t_2 is the smallest time after t_1 such that the criteria (1.30) is again satisfied and $\cos\theta(t_1)\cos\theta(t_2) < 0$. In the simulations, ϵ is set to 0.01; the specific choice of ϵ was verified not to affect the statistical analysis of tumbling, provided the threshold $1 - \epsilon$ is sufficiently close to 1.

1.5.1. Properties of the tumbling dynamics. The tumbling dynamics described above is not periodic. On the contrary, the time τ separating two tumbling events is distributed randomly. For each different value of the Weissenberg number Wi , at least 10^4 tumbling realizations were collected. The resulting PDF of τ has an exponential tail:

$$p(\tau) \propto \exp(-\tau/\tau_0) \quad (1.31)$$

for $\tau \gg \tau_0$. Moreover, the typical tumbling time τ_0 increases exponentially as a function of Wi (see Fig. 1.16, left). Hence, as the flow becomes stronger, it takes a longer time for a tumbling to occur. The configurations P_π indeed become increasingly stable, and larger Brownian fluctuations are required for the system to escape from the basins of attraction of P_π .

The above properties of the PDFs $p(\tau)$ can be predicted by using the Freidlin–Wentzell large deviations theory [36] (see also Ref. [98]). Indeed, for large values of Wi (or Pe since $Z = 1$ is kept constant in the simulations), tumbling in an extensional flow can be regarded as escaping from an attractor of a stochastic dynamical system in the limit of small noise. The PDF of the exit time thus has an exponential tail and the mean exit time increases exponentially as the amplitude of the noise vanishes. The same theory also predicts the tumbling-through-folding phenomenon. Indeed, the most probable transition paths, or minimum energy paths, that connect two adjacent configurations P_π are parallel to the gradient of the pseudo-potential $V = -\ln\psi_{st}$ [28]. The application of the improved string method to V [30] shows that these minimum energy paths pass through the folded configurations P_\star , which

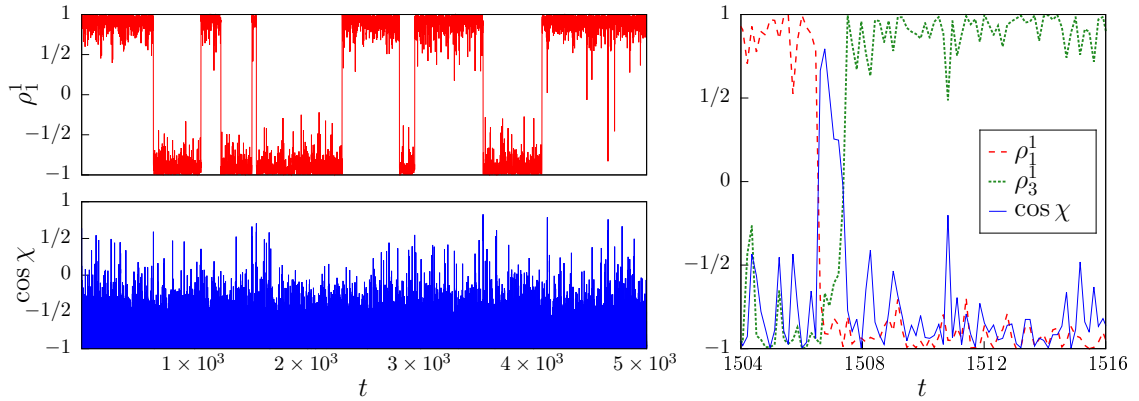


FIGURE 1.17. Time series of $\rho_1^1(t)$ (left, top) and $\cos \chi(t)$ (left, bottom) for a three-dimensional planar extensional flow with $Z = 1$, $Wi = 10$. Right: zoom of the time series of ρ_1^1 , ρ_3^1 , $\cos \chi$ over a tumbling event.

are saddle points of V (see also appendix 1.7.4). By way of illustration, a minimum energy path connecting (π, π) and $(0, \pi)$ is given in Fig. 1.13.

1.5.2. Extension to three dimensions. The analysis so far considers a two-dimensional velocity field. However, in a realistic planar extensional flow, a trumbbell may move outside the plane of the flow. This situation can be described by considering a three-dimensional velocity field

$$\mathbf{u} = \lambda(x, -y, 0), \quad \lambda > 0. \quad (1.32)$$

In this case, the trumbbell has four degrees of freedom $\mathbf{q} = (\alpha, \beta, \gamma, \chi)$ as described in Sec. 1.3.2. This formulation, however, is not suitable for numerical simulations (see remark in Sec. 1.3.2). To circumvent this difficulty, the formulation of the trumbbell in terms of its rods $\boldsymbol{\rho}_1$ and $\boldsymbol{\rho}_3$ (see Sec. 1.2) is used. The system (1.12) of Stratonovich stochastic differential equations for $\boldsymbol{\rho}_1$ and $\boldsymbol{\rho}_3$ has been numerically solved with the Euler–Heun method with $dt = 10^{-3}$ (a brief description of the scheme is available in appendix 1.7.3) [54].

When Wi is sufficiently high, the trumbbell is observed to be predominantly in the extended configuration $\chi = \pi$ with the separation vectors aligned or anti-aligned with the stretching direction of the flow. At random times, the trumbbell folds and reverses its orientation, with a dynamics similar to that observed in two dimensions. A time series showing $\cos \chi$ and the first component of $\boldsymbol{\rho}_1$ is shown in Fig. 1.17. The tumbling events can be identified as before by replacing $\cos \theta, \cos(\theta + \chi)$ with the first components of $\boldsymbol{\rho}_1$ and $\boldsymbol{\rho}_3$, respectively. The PDF of the tumbling time is again exponential for long times with a time scale increasing exponentially with Wi (see Fig. 1.16, right). The tumbling statistics, therefore, shows properties similar to those found in a purely two dimensional flow. For the same values of Wi , the mean tumbling time is however significantly shorter than in two dimensions. This fact is attributed to the increased dimensionality of the system, which makes it easier for the trumbbell to escape from the aligned or anti-aligned configuration. For the same reason, the asymptotic exponential behaviour of the typical tumbling time τ_0 is observed at larger Wi compared to the two-dimensional case.

1.6. Concluding remarks and perspectives

The phenomenon of tumbling is commonly associated with shear flows. The simplest objects that perform end-over-end tumbling in a simple shear, viz. axisymmetric solid particles and the dumbbell, exhibit a trivial orientational dynamics in an extensional flow and do not tumble. It was shown that, in contrast, a rich dynamics is obtained by considering one of the most elementary semiflexible objects, namely the trumbbell. The mere consideration of one bending mode indeed yields a random end-over-end tumbling motion with exponentially distributed tumbling times. While it is well known that several microscopic objects tumble in a shear flow, tumbling had not been observed in an extensional flow before. Moreover, a fundamental qualitative difference between the tumbling motion in an extensional flow and the analogous motion in a shear flow is found. In the latter case, the typical tumbling time decreases as a power law of Wi ; in the former case, it increases exponentially as Wi increases. This difference is a consequence of the fact that the configurations aligned with the flow are stable in an extensional flow, whereas they are unstable in a shear flow.

This chapter also shows that in an extensional flow, a trumbbell reverses its orientation by folding and then extending again in the opposite direction. This dynamics is reminiscent of the buckling instability of a fiber near to a hyperbolic point [63, 81]. Nevertheless, the tumbling motion described here is triggered by Brownian fluctuations that bend the trumbbell, whereas the buckling instability of a fiber results from its internal dynamics and does not necessarily require Brownian fluctuations.

The simplicity of the trumbbell model has allowed the study of its tumbling motion in detail and to relate this phenomenon to the properties of the stable configurations of the trumbbell and to the structure of the corresponding basins of attraction. In this study, the most elementary version of the trumbbell model was considered. In particular, hydrodynamic and excluded volume interactions between the beads are disregarded. If the size of the beads is sufficiently smaller than their mutual separations, the inclusion of such interactions into the model would somewhat modify the stable folded configuration (e.g. exact location of the fixed point P_*) but not the essential structure of the phase space of the system. Hydrodynamic and excluded volume interactions are however secondary to the main flow especially when Wi increases. Therefore, although a more accurate description of the trumbbell would require taking into account these interactions [25, 62], these interactions are not expected to alter the essential properties of the tumbling dynamics, as long as the size of the beads is small compared to their mutual separations.

Further explorations of this study include modification of the particle, for instance, to four-bead particles or n -bead chains. The rigidity of the rods may also be relaxed to an extensible spring. It is inferred that the former case may probably still exhibit tumbling, but with increasing difficulty as n increases, since it requires a very favourable sequence of partial foldings in the extensional flow. In the latter case, noting that the rigidity of the rods in this chapter permitted the tumbling, an infinitely extensible (and sufficiently elastic) spring will probably imitate the behaviour of an elastic dumbbell. A finitely-extensible spring may possibly display more interesting dynamics. All these suggested extensions considered variations of the particle but

keeps the flow extensional steady. The trumbbell in a random or turbulent flow will be the topic of Chap. 3.

1.7. Appendices

1.7.1. Calculation of the restoring forces. The forces \mathbf{f}_ν in Eqs. (1.5) can be obtained in two steps: first, by obtaining the direction of the force and then obtaining its magnitude. The calculation for \mathbf{f}_1 is demonstrated here; that for \mathbf{f}_3 follows similarly. The relation $\mathbf{f}_2 = -(\mathbf{f}_1 + \mathbf{f}_3)$ is required in the balance of forces.

Since $\mathbf{f}_1 \perp \boldsymbol{\rho}_1$ (\mathbf{f}_1 pushes the rod $\boldsymbol{\rho}_1$ to open), then $\{\hat{\mathbf{f}}_1, \hat{\boldsymbol{\rho}}_1\}$ forms an orthonormal basis for \mathbb{R}^2 (recall that $\hat{\mathbf{v}} = \mathbf{v}/|\mathbf{v}|$ for a vector \mathbf{v}), and hence

$$\begin{aligned}\boldsymbol{\rho}_3 &= (\boldsymbol{\rho}_3 \cdot \hat{\boldsymbol{\rho}}_1)\hat{\boldsymbol{\rho}}_1 + (\boldsymbol{\rho}_3 \cdot \hat{\mathbf{f}}_1)\hat{\mathbf{f}}_1 \\ &= \rho_3 \cos \chi \hat{\boldsymbol{\rho}}_1 - \rho_3 \sin \chi \hat{\mathbf{f}}_1.\end{aligned}$$

It then follows that $\hat{\mathbf{f}}_1 = \hat{\boldsymbol{\rho}}_1 \cot \chi - \hat{\boldsymbol{\rho}}_3 \csc \chi$. The magnitude can be calculated by noting that $\mathbf{f}_1 = \nabla \phi$, where $\phi = \frac{A}{2}(\pi - \chi)^2$ is the potential. The gradient can be calculated in polar coordinates ρ_1, χ as

$$\begin{aligned}\mathbf{f}_1 &= \left(\frac{\partial \phi}{\partial \rho_1}, \frac{1}{\rho_1} \frac{\partial \phi}{\partial \chi} \right) \\ &= \left(0, \frac{A}{\ell}(\pi - \chi) \right),\end{aligned}$$

from which the magnitude A_χ appearing in Eqs. (1.5) is obtained. Note that Eqs. (1.5) for the forces correct a typing error in Ref. [25] in the relation of the forces $\mathbf{f}_1, \mathbf{f}_2$ and \mathbf{f}_3 .

1.7.2. Itô and Stratonovich stochastic differential equations. Let $W(t)$ be a Wiener process and $g(t)$ be L^2 -integrable (for time $[0, T]$). The Itô integral $\int_0^T g(x, t) dW(t)$ is the mean-square limit of the sum

$$\sum_{i=1}^{n-1} g(\xi_i)(W(t_{i+1}) - W(t_i))$$

as $n \rightarrow \infty$, where $0 = t_0 < t_1 < \dots < t_n = T$ is a partition of $[0, T]$ into n intervals and $\xi_i \in [t_i, t_{i+1}]$ is chosen to be $\xi_i = t_i$. It is well known that the Itô calculus, while enjoying the martingale property, does not obey the same usual rules of classical calculus due to the fact that $dW^2(t) = dt$ in the sense of the mean square. Transformations or nonlinear combinations of stochastic differentials must use the known Itô formula [54].

A different choice for ξ_i results in a different value of the integral. The choice of $\xi_i = \frac{1}{2}(t_i + t_{i+1})$ leads to the Stratonovich integral, which has the advantage of preserving the rules of classical calculus. To distinguish the Stratonovich integral, the symbol ‘ \circ ’ is used: $\int_0^T g \circ dW(t)$. The choice of Itô or Stratonovich depends largely on the particular model at hand. Many systems that use white noise to model smooth real noise, such as systems in physics and engineering that are derived from physical laws, generally use the Stratonovich formulation. On the other hand, biological processes often use the Itô formulation because the resulting SDEs are often approximated from discrete processes.

Classifying an SDE as Itô or Stratonovich depends on the interpretation of the stochastic integral. There exists a relation, however, that associates any Stratonovich SDE to an Itô SDE and vice versa. For instance in the one-dimensional setting, any solution x to the Itô SDE

$$dx = \mathcal{A} dt + \mathcal{B} dW(t)$$

for some functions $\mathcal{A}(x, t), \mathcal{B}(x, t)$ is also a solution of the Stratonovich SDE

$$dx = \left(\mathcal{A} - \frac{1}{2} \mathcal{B} \frac{\partial \mathcal{B}}{\partial x} \right) dt + \mathcal{B} dW(t).$$

The reader is referred to the next chapter (Sec. 2.3.1) where the derivation of this relation is given (in vector form and with multiple sources of noise). The reader may also check Ref. [54] for more details.

1.7.3. Numerical methods for stochastic integration. In this section, the Euler–Maruyama method and the Euler–Heun method are described. These integrate the Itô and Stratonovich differential equations, respectively. These methods are strong Taylor approximation with order of convergence 0.5; they are sufficient in view of the equations concerned in this thesis. Consider a system of Itô SDEs

$$dq^i = V^i dt + \tilde{D}^{ij} dW^j(t)$$

where \mathbf{W} is a vector of m independent Wiener processes. The Euler–Maruyama method allows the calculation of the value $q_{n+1}^i = q^i(t + \delta t)$ from its previous value $q_n^i = q^i(t)$ (δt is the time step of integration) by the relation:

$$q_{n+1}^i = q_n^i + V^i(\mathbf{q}_n) \delta t + \tilde{D}^{ij}(\mathbf{q}_n) (W_{n+1}^j - W_n^j). \quad (1.33)$$

While it may be convenient to convert the Stratonovich SDEs into Itô SDEs and use the Euler–Maruyama method, the Euler–Heun method takes into account this transformation. Let

$$dq^i = A^i dt + B^{ij} \circ dW^j(t)$$

be a system of Stratonovich SDEs. The value of q_{n+1}^i calculated from q_n^i is given by first calculating an intermediate value, say \mathbf{p}_n with

$$\mathbf{p}_n^i = q_n^i + \tilde{D}^{ij}(\mathbf{x}_n) (W_{n+1}^j - W_n^j)$$

followed by the relation:

$$q_{n+1}^i = q_n^i + V^i(\mathbf{q}_n) \delta t + \frac{1}{2} \left(\tilde{D}^{ij}(\mathbf{q}_n) + \tilde{D}^{ij}(\mathbf{p}_n) \right) (W_{n+1}^j - W_n^j).$$

It is useful to remind the reader that the differences $W_{n+1}^j - W_n^j$ are normally distributed with zero-mean and variance $\sqrt{\delta t}$, by definition of a Wiener process. The reader is referred to Ref. [54] for more details.

1.7.4. Minimum energy paths and the String method. Consider a system in which a particle experiences thermal fluctuations and whose permissible states \mathbf{x} is associated to a smooth surface potential V that describes its energy. For the purposes of simplification, suppose that V has two different local minima M_1 and M_2 , i.e. there exist two stable configurations for the particle. Thanks to the thermal noise, a particle on a local minimum say M_1 may eventually escape the basin of M_1 and explore the surface, depending on the geometry of V and on the amount of thermal noise available.

A minimum energy path (MEP) connecting M_1 and M_2 is the path by which the transition between these two local minima requires minimal energy or thermal noise to achieve. Associated to a minimum energy path is a large probability that the transition between the two states M_1 and M_2 will occur through the states represented by the points in the minimum energy path. It is defined mathematically as a smooth curve φ^0 such that

$$(\nabla V)^\perp(\varphi^0(\alpha)) = 0,$$

where $(\nabla V)^\perp = \nabla V - (\nabla V, \tau)\tau$ is the component of ∇V normal to φ^0 (τ is the unit tangent to $\varphi^0(\alpha)$, and $\alpha \in [0, 1]$ parametrizes the string φ^0 such that $\varphi^0(0) = M_1$ and $\varphi^0(1) = M_2$). The (zero-energy) string method is a computational tool that is used to calculate the MEP in the absence of thermal noise [29]. In this case, the points on the string $\varphi^0(\alpha)$ are evolved such that

$$\dot{\varphi}^0(\alpha) = -(\nabla V)^\perp \varphi^0(\alpha) + r(\alpha, t)\tau$$

where r enforces some reparametrization. A simplified and improved string method groups the tangential term from $(\nabla V)^\perp$ together with the parametrization r , and the evolution only requires

$$\dot{\varphi}^0(\alpha) = -(\nabla V)\varphi^0(\alpha) + \bar{r}(\alpha, t)\tau,$$

which is less computationally expensive. Details can be found in Refs. [28, 29, 30].

CHAPTER 2

Bead-rod-spring models in random flows

2.1. Introduction

The previous chapter considered the trumbbell in a laminar extensional flow as an initial step to study its bending dynamics in a turbulent flow. Another step closer towards a turbulent flow is to study the trumbbell in a Gaussian random flow with short correlation time, which still permits analytical results even with a velocity gradient that is time-dependent [35]. The diffusion equation (1.14) as provided in the previous chapter cannot be used because it assumes a steady flow, which a random flow is not. In this chapter, a diffusion equation will be derived that will work not only for a trumbbell in a random flow but also for more general particle models.

The study of polymer solutions generally requires a coarse-grained description of a polymer molecule that significantly reduces the complexity of the particle but retains its essential features. A successful and well-established approach consists in using bead-rod-spring models, where a polymer is described as a sequence of beads connected by rigid or elastic links [6, 10, 22, 70] (see Fig. 2.1). By selecting the number of beads and the nature of the links, it is possible to build flexible, semiflexible, or rigid molecules with various internal structures. Polymers, for instance, can be considered as a long chain of hundreds of freely-jointed beads while axisymmetric rods can be considered as a sequence of rigidly-connected beads. Semiflexible particles like fibers can be described by beads with restoring potentials, a minimal example of which is the trumbbell (see Chap. 1). More complex shapes like the tri-dumbbell, i.e. three dumbbells oriented in three orthogonal directions and merged at their midpoints, can be attained if the beads are not restricted to form a chain or restricted to lie in a plane. Given the variety of particles that they can model, bead-rod-spring models play a central role across several fields, including rheology, non-Newtonian fluid mechanics, chemical physics, soft matter [10, 59].

Analytical solutions of these bead-rod-spring models represent an essential step towards the derivation of constitutive equations and hence the prediction of the non-Newtonian properties of polymeric fluids [6, 10, 60, 70]. In spite of their conceptual simplicity, the internal dynamics of bead-rod-spring models may be exceedingly complex. For this reason bead-rod-spring models have been solved analytically only in simplified settings. In the case of laminar flows, analytical results are restricted to linear velocity fields with elementary time dependence, namely steady, start-up, or oscillatory extensional and shear flows [6, 10, 70]. In the case of randomly fluctuating flows, exact solutions are only available for dumbbells, which are simply composed of two beads and a single elastic or rigid link [2, 3, 14, 16, 18, 19, 67, 89, 95, 99]. In the latter case, even if they correctly predict some general phenomena, results are limited to observables that concern the end-to-end vector describing the dumbbell. For instance, in an isotropic, homogenous, random flow, the coil-stretch transition

can be observed because it can be captured by the elastic dumbbells. Bending or buckling cannot be exhibited by dumbbells.

In recent years, however, there has been a growing interest in the Lagrangian dynamics of complex-shaped objects in turbulent flows since they offer a more realistic model than dumbbells. The coil-stretch transition and tumbling phenomenon continue to be studied [64, 105], but these more complex particles may now necessitate considering entanglements or take into consideration hydrodynamic or bead-bead interactions. In this chapter an analytical tool that is applicable even to these complex particles is provided via a diffusion equation for the probability distribution function (PDF) of the configuration of a general bead-rod-spring polymer in a random flow. The derived equation will be used in this thesis primarily to analytically predict the bending dynamics of a semiflexible particle (the trumbbell) in a turbulent flow in Chap. 3. To permit a fully analytical result, turbulent flows have been modeled as Gaussian random flows with short correlation time [55]. Indeed short-correlated stochastic fields have been widely employed in the theoretical study of turbulent flows as they have yielded fundamental results on passive-scalar mixing and on turbulent dynamo [35]. Moreover, they have been used to predict the coil-stretch transition of polymers in turbulent flows [3] and the associated critical slowing down [16]. This is in spite of suffering shortcomings as real flows are not delta-correlated in time nor are turbulent velocity fields Gaussian.

The general bead-rod spring model is introduced in Section 2.2; the formulation follows the approach in Refs. [10, 70]. Section 2.3 describes the derivation of the diffusion equation of a general bead-rod-spring model for a short-correlated, Gaussian, random flow. In Sec. 2.4, the practical use of this diffusion equation is illustrated by calculating the stationary configuration in an isotropic random flow for a model that has both rigid and elastic links between the beads: the elastic rhombus model [23]. Concluding remarks and perspectives will follow.

2.2. Bead-rod-spring models

Consider N spherical beads with mass m_μ , $\mu = 1, \dots, N$. Let \mathbf{x}_μ denote the position vector of the μ th bead with respect to a space-fixed coordinate system. The position of the centre of mass of the polymer is

$$\mathbf{x}_{\text{CM}} = \sum_{\mu} m_{\mu} \mathbf{x}_{\mu} / \sum_{\mu} m_{\mu}, \quad (2.1)$$

and the position vector of the μ th bead referred to the centre of mass is

$$\mathbf{r}_{\mu} = \mathbf{x}_{\mu} - \mathbf{x}_{\text{CM}}. \quad (2.2)$$

The polymer is immersed in a Newtonian fluid, whose motion is described by the incompressible velocity field $\mathbf{u}(\mathbf{x}, t)$. The velocity gradient, $\boldsymbol{\kappa} = \nabla \mathbf{u}$, $\kappa^{ij} = \partial u^i / \partial x^j$, is assumed to be uniform over the length of the polymer. If the flow is turbulent, this assumption means that the size of the polymer is much smaller than the viscous-dissipation scale. The force of the flow on bead μ is given by Stokes's law with drag coefficient ζ_{μ} ; the inertia of the beads is disregarded. Furthermore, the concentration of the solution is sufficiently small for polymer-polymer hydrodynamic interactions to be negligible, and the flow is unperturbed by the presence of polymers.

Assume that the beads are subject to D' rigidity constraints. Then, the number of degrees of freedom of the polymer in the frame of reference of the centre of mass is

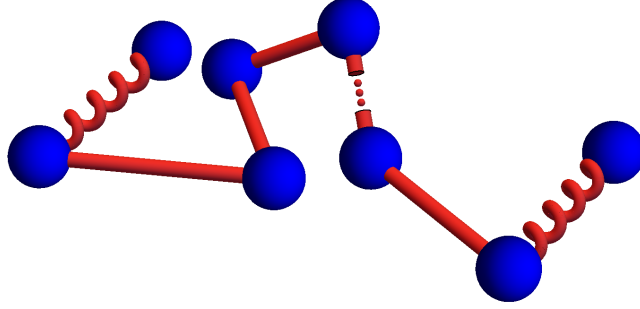


FIGURE 2.1. Illustration of a general bead-rod-spring model with rigid and elastic links.

$D = d(N - 1) - D'$, where d is the dimension of the flow. It is therefore convenient to specify the configuration of the polymer in terms of D coordinates $\mathbf{q} = (q^1, \dots, q^D)$, which describe its degrees of freedom. The statistics of the coordinates \mathbf{q} is given by the PDF $\psi(\mathbf{q}; t)$. The choice of notation should have hinted that this is a more general formulation than the one used in Chap. 1. Indeed, the formulation in this chapter may be used to obtain the trumbbell model by considering three beads and choosing the appropriate force terms between the beads and neglecting hydrodynamic interactions. For instance, a three-dimensional trumbbell will have $D = 3(3 - 1) - 2 = 4$ degrees of freedom, which were taken to be the Euler angles α, β, γ and the internal angle χ .

The tensors $\zeta_{\mu\nu}$ are defined implicitly from the equation: $\sum_{\nu} \zeta_{\mu\nu} \cdot (\zeta_{\nu}^{-1} \delta_{\nu\mu'} \mathbf{I} + \mathbf{\Omega}_{\nu\mu'}) = \delta_{\mu\mu'} \mathbf{I}$, where $\delta_{\mu\mu'}$ is the Kronecker delta, \mathbf{I} is the identity matrix, and the tensors $\mathbf{\Omega}_{\nu\mu}$ describe the hydrodynamic interactions between the μ th and the ν th bead (in the simplest approximation $\mathbf{\Omega}_{\mu\nu}$ is the Oseen tensor, which is used to estimate the effect of one moving bead μ on the velocity field felt by another bead ν ; its explicit expression is available, e.g., in Ref. [10]). Define also the tensors $\mathbf{Z} = \sum_{\mu\nu} \zeta_{\mu\nu}$, $\mathbf{\Lambda}_{\nu} = \mathbf{Z}^{-1} \cdot \sum_{\mu} \zeta_{\mu\nu}$, and $\tilde{\zeta}_{\mu\nu} = \zeta_{\mu\nu} - \mathbf{\Lambda}_{\mu}^T \cdot \mathbf{Z} \cdot \mathbf{\Lambda}_{\nu}$. Finally, $\mathbf{f}_{\mu\nu}$ is the force exerted by the ν th bead over the μ th one through the springs and \mathbf{f}_{μ} is the external force on bead μ (which is assumed to be independent of \mathbf{x}_{CM}). Then, $\Psi(\mathbf{q}; t)$ satisfies the diffusion equation [10, 70]:

$$\frac{\partial}{\partial t} \Psi(\mathbf{q}; t) = - \frac{\partial}{\partial q^i} \left\{ \tilde{\mathbf{G}}^{ij} \left[(\mathbf{M}^{jkl} \kappa^{kl}(t) + F^j + \mathfrak{F}^j) \Psi - KT \sqrt{h} \frac{\partial}{\partial q^j} \left(\frac{\Psi}{\sqrt{h}} \right) \right] \right\}, \quad (2.3)$$

where K is the Boltzmann constant, T is temperature,

$$\mathbf{M}^{jkl} = r_{\nu}^l \frac{\partial r_{\mu}^m}{\partial q^j} \tilde{\zeta}_{\mu\nu}^{mk}, \quad F^j = \sum_{\nu} f_{\mu\nu}^k \frac{\partial r_{\mu}^k}{\partial q^j}, \quad \mathfrak{F}^j = \mathbf{f}_{\mu}^k \frac{\partial r_{\mu}^k}{\partial q^j}, \quad (2.4)$$

$h = \det(\mathbf{H})$, and $\tilde{\mathbf{G}} = \tilde{\mathbf{H}}^{-1}$ with:

$$\mathbf{H}^{ij} = m_\mu \frac{\partial r_\mu^k}{\partial q^i} \frac{\partial r_\mu^k}{\partial q^j}, \quad \tilde{\mathbf{H}}^{ij} = \tilde{\zeta}_{\mu\nu}^{kl} \frac{\partial r_\mu^k}{\partial q^i} \frac{\partial r_\nu^l}{\partial q^j}. \quad (2.5)$$

Equation (2.3) and the expressions (2.5) are the generalizations of Eqs. (1.14) and (1.15), where the beads were assumed to be identical and external forces were disregarded. The stationary solution of Eq. (2.3) can be calculated exactly when hydrodynamic bead–bead interactions are negligible ($\boldsymbol{\Omega}_{\mu\nu} = 0$ for all $\mu, \nu = 1, \dots, N$) or equilibrium averaged ($\boldsymbol{\Omega}_{\mu\nu}$ is replaced with its average value at equilibrium) and the velocity gradient is time-independent and symmetric ($\boldsymbol{\kappa} = \boldsymbol{\kappa}^T$) [10, 23]. For other flows, Bird *et al.* [10] note that the analytical solution of Eq. (2.3) is in general a formidable problem.

2.3. Diffusion equation for a short-correlated random flow

The diffusion equation (2.3) for the general bead-rod-spring model holds for a time-dependent velocity gradient. Whereas it was steady in the previous chapter, the velocity gradient now fluctuates randomly in time, as in turbulent flows. This section then derives the diffusion equation for the case of a random flow $\boldsymbol{\kappa}(t)$ that is a delta-correlated-in-time ($d \times d$)-dimensional Gaussian stochastic process with zero mean and correlation:

$$\langle \kappa^{kl}(t) \kappa^{mn}(t') \rangle = \mathcal{K}^{klmn} \delta(t - t'), \quad (2.6)$$

where the specific form of the tensor \mathcal{K} depends on the statistical symmetries of the flow and δ is the Dirac-delta function. Under the assumption that the velocity gradient satisfies Eq. (2.6), Equation (2.3) is now stochastic and describes the evolution of $\Psi(\mathbf{q}; t)$ for a given realization of the flow; the velocity gradient $\boldsymbol{\kappa}(t)$ is a multiplicative noise and is interpreted in the Stratonovich sense. It is useful to repeat the comment in the introduction that while the assumption on the decorrelation of time is unrealistic, this simplification yields analytical results that in many instances nevertheless reflect the dynamics of the system.

A convenient way to derive the diffusion equation that takes into consideration two different sources of noise (the stochastic velocity field and the thermal fluctuations) requires two main steps. First, the corresponding Stratonovich SDE (stochastic differential equation) to Eq. (2.3) is written in its Itô form, and secondly, the resulting Itô form is converted into a diffusion equation, in which the coefficient \mathcal{K} will appear. At this point, the eager reader may wish to jump over the calculations to view the final result, which is given as the diffusion equation (2.21). The technical calculations that follow may be read at one's convenience.

The first step in the upcoming calculations requires the Stratonovich SDE associated with Eq. (2.3). This SDE is (see Ref. [38]):

$$dq^i = A^i dt + \mathbf{B}^{ij} \circ dW^j(t) + \mathbf{C}^{ikl} \circ d\Gamma^{kl}(t), \quad (2.7)$$

where $\mathbf{W}(t)$ is D -dimensional Brownian motion and $\boldsymbol{\Gamma}(t)$ is such that $\boldsymbol{\kappa}(t) = d\boldsymbol{\Gamma}(t)/dt$, i.e. $\boldsymbol{\Gamma}(t)$ is a Gaussian process with $\langle \Gamma^{kl}(t) \rangle = 0$ and $\langle \Gamma^{kl}(t) \Gamma^{mn}(t') \rangle = \mathcal{K}^{klmn} \min(t, t')$. The symbol ‘ \circ ’ indicates that the SDE is interpreted in the Stratonovich sense. The coefficients are

$$A^i = \tilde{\mathbf{G}}^{ij} (F^j + \mathfrak{F}^j) + KT \frac{\beta^{ia}}{\sqrt{h}} \frac{\partial}{\partial q^j} (\sqrt{h} \beta^{ja}), \quad (2.8)$$

$$\mathbf{B}^{ij} = \sqrt{2KT} \beta^{ij}, \quad (2.9)$$

$$\mathbf{C}^{ikl} = \tilde{\mathbf{G}}^{ij} \mathbf{M}^{jkl}. \quad (2.10)$$

In the above equations, β is such that $\beta \beta^\top = \tilde{\mathbf{G}}$ (it is assumed that $\tilde{\mathbf{G}}$ is positive definite—this condition is easily verified when the masses and the drag coefficients are the same for all beads).

2.3.1. Step 1: Converting into the Itô formulation. Following the strategy indicated above, the Itô version of Eq. (2.7) is derived in this subsection and culminates in Eq. (2.19); it is done formally by generalizing the standard transformation rules for SDEs to tensorial Brownian motion. Assume that the Itô version is:

$$dq^i(t) = \mathfrak{A}^i dt + \mathfrak{B}^{ij} dW^j(t) + \mathfrak{C}^{ikl} d\Gamma^{kl}(t), \quad (2.11)$$

where the coefficients \mathfrak{A} , \mathfrak{B} , \mathfrak{C} are to be determined. Equation (2.7) is first written in integral form:

$$q^i(t) = q^i(t_0) + \int_{t_0}^t A^i dt' + \int_{t_0}^t \mathbf{B}^{ia} \circ dW^a(t') + \int_{t_0}^t \mathbf{C}^{ikl} \circ d\Gamma^{kl}(t'). \quad (2.12)$$

Consider a partition of the interval $[t_0, t]$ into N subintervals $[t_{\tau-1}, t_\tau]$, $\tau = 1, \dots, N$. The Stratonovich integrals in Eq. (2.12) are, by definition:

$$\int_{t_0}^t \mathbf{B}^{ia} \circ dW^a(t') = \lim_{N \rightarrow \infty} \sum_{\tau=1}^N \mathbf{B}^{ia}(\mathbf{q}_\tau^S, t_{\tau-1}) \Delta W_\tau^a, \quad (2.13)$$

$$\int_{t_0}^t \mathbf{C}^{ikl} \circ d\Gamma^{kl}(t') = \lim_{N \rightarrow \infty} \sum_{\tau=1}^N \mathbf{C}^{ikl}(\mathbf{q}_\tau^S, t_{\tau-1}) \Delta \Gamma_\tau^{kl}, \quad (2.14)$$

where the limits are understood in the mean-square, and where the following shorthand notations are used:

$$\begin{aligned} \mathbf{q}_\tau^S &= \frac{1}{2}(\mathbf{q}_\tau + \mathbf{q}_{\tau-1}), \\ \mathbf{q}_\tau &= \mathbf{q}(t_\tau), \\ \Delta W_\tau^a &= W^a(t_\tau) - W^a(t_{\tau-1}), \\ \Delta \Gamma_\tau^{kl} &= \Gamma^{kl}(t_\tau) - \Gamma^{kl}(t_{\tau-1}). \end{aligned}$$

The following notations are also introduced $\Delta t_\tau = t_\tau - t_{\tau-1}$ and $\mathbf{X}_\tau^I = \mathbf{X}^I(\mathbf{q}_\tau, t_\tau)$ for any tensor \mathbf{X} and set of indices I . Define $\Delta \mathbf{q}_{\tau-1} = \mathbf{q}_\tau - \mathbf{q}_{\tau-1}$, whence

$$\mathbf{q}_\tau^S = \mathbf{q}_{\tau-1} + \Delta \mathbf{q}_{\tau-1}/2.$$

Expanding the coefficients in (2.13) and (2.14) at $\mathbf{q}_{\tau-1}$ in $\Delta \mathbf{q}_{\tau-1}$ yields:

$$\mathbf{B}^{ia}(\mathbf{q}_\tau^S, t_{\tau-1}) = \mathbf{B}_{\tau-1}^{ia} + \frac{\Delta q_{\tau-1}^j}{2} \frac{\partial \mathbf{B}_{\tau-1}^{ia}}{\partial q^j} + \text{h.o.t.}, \quad (2.15)$$

$$\mathbf{C}^{ikl}(\mathbf{q}_\tau^S, t_{\tau-1}) = \mathbf{C}_{\tau-1}^{ikl} + \frac{\Delta q_{\tau-1}^j}{2} \frac{\partial \mathbf{C}_{\tau-1}^{ikl}}{\partial q^j} + \text{h.o.t.} \quad (2.16)$$

The differences $\Delta q_{\tau-1}^j$ are now written according to its Itô discretization:

$$\Delta q_{\tau-1}^j = \mathfrak{A}_{\tau-1}^j \Delta t_\tau + \mathfrak{B}_{\tau-1}^{ja} \Delta W_\tau^a + \mathfrak{C}_{\tau-1}^{jmn} \Delta \Gamma_\tau^{mn} + \text{h.o.t.} \quad (2.17)$$

After substituting Eqs. (2.15), (2.16), (2.17) into Eqs. (2.13), (2.14) and using the formal rules $\Delta\Gamma^{kl} \times \Delta\Gamma^{mn} = \mathcal{K}^{klmn} \Delta t$, $\Delta W^j \times \Delta W^a = \delta^{ja} \Delta t$ and $\Delta W^j \times \Delta\Gamma^{kl} = 0$ (owing to the independence of the velocity gradient and thermal noise), Eqs. (2.13) and (2.14) can be written as:

$$\int_{t_0}^t \mathbf{B}^{ia} \circ dW^a(t') = \lim_{N \rightarrow \infty} \sum_{\tau=1}^N \left(\mathbf{B}_{\tau-1}^{ia} \Delta W_{\tau}^a + \frac{\mathfrak{B}_{\tau-1}^{ja}}{2} \frac{\partial \mathbf{B}_{\tau-1}^{ia}}{\partial q^j} \Delta t \right),$$

$$\int_{t_0}^t \mathbf{C}^{ikl} \circ d\Gamma^{kl}(t') = \lim_{N \rightarrow \infty} \sum_{\tau=1}^N \left(\mathbf{C}_{\tau-1}^{ikl} \Delta \Gamma_{\tau}^{kl} + \frac{1}{2} \mathcal{K}^{klmn} \mathfrak{C}_{\tau-1}^{jmn} \frac{\partial \mathbf{C}_{\tau-1}^{ikl}}{\partial q^j} \Delta t \right).$$

The first terms in the sums yield Itô stochastic integrals, whereas the second terms give ordinary integrals, hence:

$$\int_{t_0}^t \mathbf{B}^{ia} \circ dW^a(t') = \int_{t_0}^t \mathbf{B}^{ia} dW^a(t') + \int_{t_0}^t \frac{\mathfrak{B}^{ja}}{2} \frac{\partial \mathbf{B}^{ia}}{\partial q^j} dt',$$

$$\int_{t_0}^t \mathbf{C}^{ikl} \circ d\Gamma^{kl}(t') = \int_{t_0}^t \mathbf{C}^{ikl} d\Gamma^{kl}(t') + \int_{t_0}^t \mathcal{K}^{klmn} \mathfrak{C}^{jmn} \frac{\partial \mathbf{C}^{ikl}}{\partial q^j} dt'.$$

Therefore, for Eq. (2.11) to be equivalent to Eq. (2.7), the coefficients must satisfy $\mathfrak{B} = \mathbf{B}$, $\mathfrak{C} = \mathbf{C}$, and

$$\mathfrak{A}^i = A^i + \frac{1}{2} \mathbf{B}^{ja} \frac{\partial \mathbf{B}^{ia}}{\partial q^j} + \frac{1}{2} \mathcal{K}^{klmn} \mathbf{C}^{jmn} \frac{\partial \mathbf{C}^{ikl}}{\partial q^j}. \quad (2.18)$$

The Itô form of Eq. (2.7) is thus:

$$dq^i = \left(A^i + \frac{1}{2} \mathbf{B}^{ja} \frac{\partial \mathbf{B}^{ia}}{\partial q^j} + \frac{1}{2} \mathcal{K}^{klmn} \mathbf{C}^{jmn} \frac{\partial \mathbf{C}^{ikl}}{\partial q^j} \right) dt + \mathbf{B}^{ij} dW^j(t) + \mathbf{C}^{ikl} d\Gamma^{kl}(t). \quad (2.19)$$

2.3.2. Step 2: The diffusion equation. The immediately-preceding Itô SDE can then be converted into the desired diffusion equation. Denote by $p(\mathbf{q}; t)$ the PDF of the configuration of the polymer with respect to the realizations both of the velocity gradient and of thermal noise. Let $f(\mathbf{q})$ be a function of \mathbf{q} . Itô's lemma will first be generalized for a tensorial Brownian motion. The expansion gives

$$\Delta f = f(\mathbf{q} + \Delta \mathbf{q}) - f(\mathbf{q}) = \Delta q^i \frac{\partial f}{\partial q^i} + \frac{\Delta q^i \Delta q^j}{2} \frac{\partial^2 f}{\partial q^i \partial q^j} + \text{h.o.t.}$$

The substitution of Δq^i and Δq^j from Eq. (2.11) and the use of the formal rules then give:

$$\frac{df}{dt} = \left[\mathfrak{A}^i + \mathfrak{B}^{ia} \frac{dW^a(t)}{dt} + \mathfrak{C}^{ikl} \frac{d\Gamma^{kl}(t)}{dt} \right] \frac{\partial f}{\partial q^i} + \frac{1}{2} (\mathfrak{B}^{ia} \mathfrak{B}^{ja} + \mathcal{K}^{klmn} \mathfrak{C}^{ikl} \mathfrak{C}^{jmn}) \frac{\partial^2 f}{\partial q^i \partial q^j}.$$

The averaging over the noises and the application of the properties of the Itô integral then yield:

$$\left\langle \frac{df}{dt} \right\rangle = \frac{d}{dt} \langle f \rangle = \int f \left(\frac{\partial p}{\partial t} \right) d\mathbf{q},$$

$$= \int \left[\mathfrak{A}^i \frac{\partial f}{\partial q^i} + \frac{1}{2} (\mathfrak{B}^{ia} \mathfrak{B}^{ja} + \mathcal{K}^{klmn} \mathfrak{C}^{ikl} \mathfrak{C}^{jmn}) \frac{\partial^2 f}{\partial q^i \partial q^j} \right] p d\mathbf{q}.$$

Integrating the right-hand side by parts gives:

$$\int f \left(\frac{\partial p}{\partial t} \right) d\mathbf{q} = \int f \left[- \frac{\partial}{\partial q^i} (\mathfrak{A}^i p) + \frac{1}{2} \frac{\partial^2}{\partial q^i \partial q^j} \left(\mathfrak{B}^{ia} \mathfrak{B}^{ja} p + \mathcal{K}^{klmn} \mathfrak{C}^{ikl} \mathfrak{C}^{jmn} p \right) \right] d\mathbf{q}.$$

Since $f(\mathbf{q})$ is arbitrary, the expressions inside the brackets should be equal. This gives the diffusion equation corresponding to Eq. (2.19) when \mathfrak{A} , \mathfrak{B} and \mathfrak{C} are chosen as above:

$$\begin{aligned} \frac{\partial p}{\partial t} = - \frac{\partial}{\partial q^i} \left[\left(A^i + \frac{1}{2} \mathfrak{B}^{ja} \frac{\partial \mathfrak{B}^{ia}}{\partial q^j} + \frac{1}{2} \mathcal{K}^{klmn} \mathfrak{C}^{jmn} \frac{\partial \mathfrak{C}^{ikl}}{\partial q^j} \right) p \right] \\ + KT \frac{\partial^2}{\partial q^i \partial q^j} (\tilde{\mathfrak{G}}^{ij} p) + \frac{\mathcal{K}^{klmn}}{2} \frac{\partial^2}{\partial q^i \partial q^j} (\mathfrak{C}^{ikl} \mathfrak{C}^{jmn} p). \end{aligned} \quad (2.20)$$

The terms in Eq. (2.20) are then rearranged, leading to:

$$\boxed{\begin{aligned} \frac{\partial p}{\partial t} = \frac{\partial}{\partial q^i} \left\{ \frac{1}{2} \mathcal{K}^{klmn} \tilde{\mathfrak{G}}^{ia} \mathfrak{M}^{akl} \frac{\partial}{\partial q^j} (\tilde{\mathfrak{G}}^{jb} \mathfrak{M}^{bmn} p) \right. \\ \left. + \tilde{\mathfrak{G}}^{ij} \left[- (F^j + \mathfrak{F}^j) p + KT \sqrt{h} \frac{\partial}{\partial q^j} \left(\frac{p}{\sqrt{h}} \right) \right] \right\}. \end{aligned}} \quad (2.21)$$

Equation (2.21) determines the evolution of the PDF of the configuration of a general bead-rod-spring model in a short-correlated Gaussian random flow.

2.4. An example: the rhombus model

The PDF $p(\mathbf{q}; t)$ describing the configuration of any bead-rod-spring polymer satisfies the derived equation (2.21). This will be used in Chap. 3 to study the trumbbell in a random flow. Nevertheless, its utility in obtaining an exact calculation of the stationary solution is demonstrated here for a model even more complex than the trumbbell. Consider now a bead-rod-spring model that has both rigid and elastic links; to keep calculations simple, consider an elastic plane rhombus model [23] (see Fig. 2.2). It describes a finitely extensible polymer and consists of four coplanar identical beads connected by four rods and of an elastic spring between two opposing beads (Fig. 2.2). The angle $0 \leq \sigma \leq \pi/2$ between the spring and one of the rods describes the deformation of the rhombus. The spring is at rest if the rods are

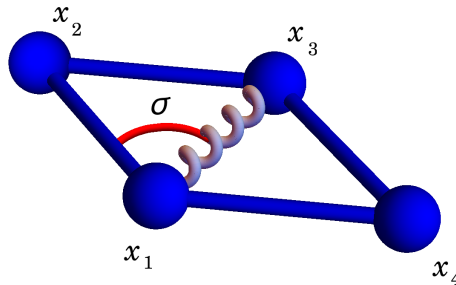


FIGURE 2.2. The elastic plane rhombus model consisting of four coplanar beads at position $\mathbf{x}_\nu, \nu = 1, \dots, 4$ connected by four rigid rods and an elastic spring between two opposing beads. The angle between the spring and one of the rods is denoted by σ .

perpendicular to each other. If $\sigma \neq \pi/4$, the spring stretches or compresses the rhombus back to its equilibrium; the force that it exerts on the beads is given by the harmonic potential

$$\phi(\sigma) = \frac{A}{2}(\sqrt{2} \cos \sigma - 1)^2, \quad (2.22)$$

where $A > 0$ is the magnitude of the potential.

To simplify calculations, all the beads are assumed to be identical, and hence they have the same masses and drag coefficients ($m_\mu = m$, $\zeta_\mu = \zeta$ for $\mu = 1, \dots, 4$); let ℓ be the length of the rods. In addition, hydrodynamical bead–bead interactions are disregarded ($\mathbf{\Omega}_{\mu\nu} = 0$), and no external forces act on the polymer ($\mathbf{f}_\mu = 0$). Under these assumptions, it follows that $\zeta_{\mu\nu} = \zeta \delta_{\mu\nu} \mathbf{1}$, $\mathfrak{F} = 0$, and the coefficients in (2.4) and (2.5) simplify to

$$\mathbf{M}^{jkl} = \zeta r_\mu^\ell \frac{\partial r_\mu^k}{\partial q^j}, \quad F^j = -\frac{\partial \phi}{\partial q^j}, \quad \tilde{\mathbf{H}}^{ij} = \zeta \frac{\partial r_\mu^k}{\partial q^i} \frac{\partial r_\mu^k}{\partial q^j}. \quad (2.23)$$

The contribution of rhombic particles to the viscoelastic properties of a solution, such as the normal stress coefficient and the viscosity, have been calculated exactly [23]. In particular, the addition of n rhombuses increases the viscosity by $3n\zeta\ell^2$; this result also holds for other variants of the rhombus model, such as that whose beads are non-planar and that which does not deform. The normal stress coefficient of the polymer solution, by contrast, varies according to the flexibility of the rhombus. In more recent literature, a fully elastic rhombus model has been used to investigate the motion of deformable active particles [57].

If the random flow is incompressible and statistically invariant under rotations and reflections, the components of \mathcal{K} take the form:

$$\mathcal{K}^{ijkl} = \frac{2\lambda}{d(d-1)} [(d+1)\delta^{ik}\delta^{jl} - \delta^{ij}\delta^{kl} - \delta^{il}\delta^{jk}], \quad (2.24)$$

where λ is the maximum Lyapunov exponent of the flow [35]. One can find a sketch of the derivation of \mathcal{K} in appendix 2.6.1. By denoting $\mathbf{G} = \zeta \tilde{\mathbf{G}}$, Eq. (2.20) can be written as a Fokker–Planck equation:

$$\frac{\partial p}{\partial t} = -\frac{\partial}{\partial q^i} (V^i p) + \frac{1}{2} \frac{\partial^2}{\partial q^i \partial q^j} (D^{ij} p), \quad (2.25)$$

where the drift and diffusion coefficients are

$$V^i = \mathbf{G}^{jb} r_\nu^n \frac{\partial r_\nu^m}{\partial q^b} \frac{\partial}{\partial q^j} \left(\frac{1}{2} \mathcal{K}^{klmn} \mathbf{G}^{ia} r_\mu^l \frac{\partial r_\mu^k}{\partial q^a} \right) - \frac{\mathbf{G}^{ij}}{\zeta} \frac{\partial \phi}{\partial q^j} + \frac{KT}{\zeta \sqrt{h}} \frac{\partial}{\partial q^j} \left(\mathbf{G}^{ij} \sqrt{h} \right), \quad (2.26)$$

and

$$D^{ij} = \mathcal{K}^{klmn} \mathbf{G}^{ia} r_\mu^l \frac{\partial r_\mu^k}{\partial q^a} \mathbf{G}^{jb} r_\nu^n \frac{\partial r_\nu^m}{\partial q^b} + \frac{2\mathbf{G}^{ij} KT}{\zeta}. \quad (2.27)$$

2.4.1. Two dimensions. In the case of a two-dimensional flow ($d = 2$), the rhombus may be described by the angular variables $\mathbf{q} = (\theta, \sigma)$, where θ gives the orientation of the spring $\mathbf{x}_3 - \mathbf{x}_1$ with respect to the horizontal axis. The vectors $\mathbf{r}_\mu = \mathbf{x}_\mu - \mathbf{x}_{\text{CM}}$ (as in Eq. (2.2)) can be expressed as:

$$\mathbf{r}_1 = \ell(-\cos \theta \cos \sigma, -\sin \theta \cos \sigma) = -\mathbf{r}_3, \quad (2.28)$$

$$\mathbf{r}_2 = \ell(-\sin \theta \sin \sigma, \cos \theta \sin \sigma) = -\mathbf{r}_4. \quad (2.29)$$

The coefficients appearing in the diffusion equation are $\mathbf{G}^{ij} = \delta_{ij}/2\ell^2$ and $h = 4\ell^2$. When time is rescaled by the characteristic time scale of the restoring potential

$$\tau = \zeta\ell^2/A \quad (2.30)$$

and Eqs. (2.28), (2.29) are replaced into Eqs. (2.26), (2.27), the drift and diffusion coefficients in Eq. (2.25) become:

$$V^\sigma = -\frac{1}{2}(\sqrt{2} - 2\cos\sigma)\sin\sigma, \quad (2.31)$$

$$D^{\theta\theta} = \frac{1}{Z} + \frac{Wi}{2}(5 + \cos 4\sigma), \quad (2.32)$$

$$D^{\sigma\sigma} = \frac{1}{Z} + \frac{Wi}{2}(1 - \cos 4\sigma), \quad (2.33)$$

where $Z = A/KT$ is the stiffness parameter that compares the strength of the restoring potential to the noise and the Weissenberg number $Wi = \lambda\tau$ measures the relative strength of the flow to that of the restoring potential $\phi(\sigma)$ defined in (2.22). The other coefficients $V^\theta, D^{\sigma\theta}, D^{\theta\sigma}$ are all zero. The fact that all the coefficients are independent of θ reflects the isotropy of the flow and implies that the long-time PDF of the configuration is a function of the angle σ alone. Given reflecting boundary conditions at $\sigma = 0$ and $\sigma = \pi/2$, the stationary PDF $p_{\text{st}}(\sigma)$ can be analytically calculated to be [38]

$$p_{\text{st}}(\sigma) \propto \frac{1}{D^{\sigma\sigma}} \exp\left(2 \int_0^\sigma \frac{V^\sigma(\sigma')}{D^{\sigma\sigma}(\sigma')} d\sigma'\right). \quad (2.34)$$

The explicit form of the PDF of σ can be evaluated as:

$$\boxed{p_{\text{st}}(\sigma) \propto \frac{1}{D^{\sigma\sigma}} \left| \frac{C_\sigma^2 - C_+^2}{C_\sigma^2 + C_-^2} \right|^{Z/4C_1} \exp\left\{ \frac{Z\sqrt{WiZ}}{2C_1} \times \left[\frac{\text{arctanh}(C_\sigma/C_+)}{C_+} + \frac{\text{arctan}(C_\sigma/C_-)}{C_-} \right] \right\}} \quad (2.35)$$

with $C_\sigma = \sqrt{2WiZ}\cos\sigma$, $C_1 = \sqrt{WiZ(WiZ+1)}$, and $C_\pm = \sqrt{C_1 \pm WiZ}$. The details of this calculation are given in the appendix 2.6.4. Figure 2.3 illustrates the graph of $p_{\text{st}}(\sigma)$ for $Z = 1$ and different values of Wi . The probability of the rhombus being fully stretched ($\sigma = 0$) or fully compressed ($\sigma = \pi/2$) increases with Wi , i.e. the rhombus exhibits an almost rodlike configuration when a very strong flow dominates the dynamics. However, the stretched configuration is favored compared to the compressed one, because the restoring force is weaker for $\sigma = 0$ than for $\sigma = \pi/2$.

2.4.2. Three dimensions. In a three-dimensional flow, the number of degrees of freedom of the elastic planar rhombus is $D = 4$ and the rhombus is represented by its angles: $\mathbf{q} = (\alpha, \beta, \gamma, \sigma)$, where the first three coordinates are the Euler angles that define the plane on which the rhombus lies (see Sec. (1.3.2)). The explicit expressions of the components of \mathbf{G} are [10, 23]:

$$\mathbf{G}^{11} = \frac{1 + \cos 2\gamma \cos 2\sigma}{\ell^2 \sin^2 \beta \sin^2 2\sigma}$$

$$\mathbf{G}^{12} = -\frac{\sin 2\gamma \cos 2\sigma}{\ell^2 \sin^2 \beta \sin^2 2\sigma} = \mathbf{G}^{21}$$

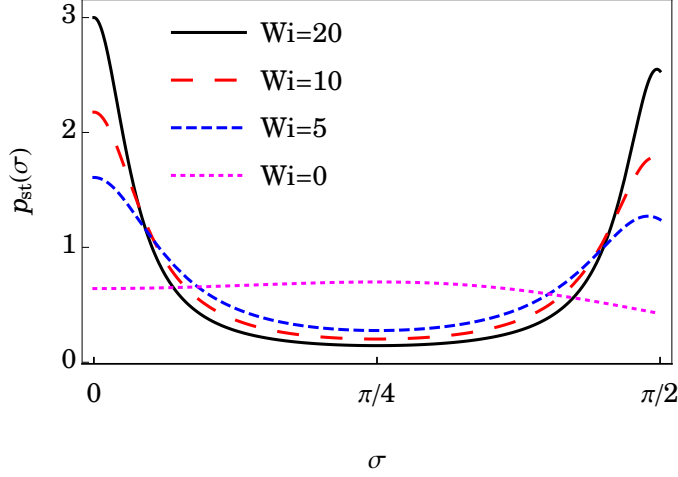


FIGURE 2.3. Stationary PDF $p_{\text{st}}(\sigma)$ for $d = 2$ and $Z = 1$, normalized such that $\int p_{\text{st}}(\sigma) d\sigma = 1$.

$$\begin{aligned}
\mathbf{G}^{13} &= -\cos \beta \mathbf{G}^{11} = \mathbf{G}^{31} \\
\mathbf{G}^{22} &= \frac{1 - \cos 2\gamma \cos 2\sigma}{\ell^2 \sin^2 2\sigma} \\
\mathbf{G}^{23} &= \frac{\cot \beta \cos 2\sigma \sin 2\gamma}{\ell^2 \sin^2 2\sigma} = \mathbf{G}^{32} \\
\mathbf{G}^{33} &= \frac{3 + 2 \cos(2(\gamma - \sigma)) + \cos 4\sigma + 2 \cos(2(\gamma + \sigma)) - 4 \csc^2 \beta (1 + \cos 2\gamma \cos 2\sigma)}{4\ell^2 \sin^2 2\sigma} \\
\mathbf{G}^{44} &= \frac{1}{2\ell^2} \\
\mathbf{G}^{14} &= \mathbf{G}^{24} = \mathbf{G}^{34} = \mathbf{G}^{41} = \mathbf{G}^{42} = \mathbf{G}^{43} = 0
\end{aligned}$$

while the determinant $h = \det \mathbf{G}^{-1}$ is $h = 4\ell^8 \sin^2 2\sigma \sin^2 \beta$. The PDF $p(\mathbf{q})$ of the configuration again satisfies a rescaled version of Eq. (2.25) by using the transformation $s = t/\tau$, where V^i and D^{ij} are given as follows:

$$\begin{aligned}
V^\alpha &= \frac{2}{Z} \sin 2\gamma \cot \beta \csc \beta \cot 2\sigma \csc 2\sigma, \\
V^\beta &= \cot \beta \csc^2 2\sigma \left[\frac{1}{Z} (1 + \cos 2\gamma \cos 2\sigma) + \frac{Wi}{3} (1 - \cos 4\sigma) \right], \\
V^\gamma &= -\frac{1}{2Z} (3 + \cos 2\beta) \csc^2 \beta \cot 2\sigma \csc 2\sigma \sin 2\gamma, \\
V^\sigma &= \frac{1}{Z} \cot 2\sigma - \frac{1}{2} (\sqrt{2} - 2 \cos \sigma) \sin \sigma.
\end{aligned}$$

The diffusion coefficients D^{ij} are:

$$\begin{aligned}
D^{\alpha\alpha} &= 4 \csc 2\beta V^\beta, \quad D^{\alpha\beta} = -\tan \beta V^\alpha, \quad D^{\alpha\gamma} = -2 \csc \beta V^\beta, \\
D^{\beta\beta} &= \frac{1}{Z} (\cos^2 \gamma \sec^2 \sigma + \sin^2 \gamma \csc^2 \sigma) + \frac{4Wi}{3}, \\
D^{\beta\gamma} &= \sin \beta V^\alpha, \quad D^{\sigma\sigma} = \frac{1}{Z} + \frac{Wi}{4} (1 - \cos 4\sigma)
\end{aligned}$$

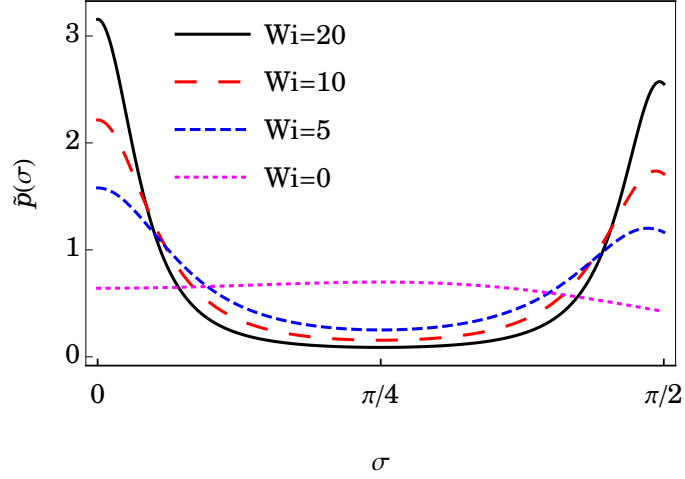


FIGURE 2.4. The function $\tilde{p}(\sigma)$ for $d = 3$ and $Z = 1$, normalized such that $\int \tilde{p}(\sigma) \sin 2\sigma d\sigma = 1$.

$$D^{\gamma\gamma} = 48 \csc^2 2\sigma \left\{ \frac{24}{Z} [4 (\cos 2\gamma \cos 2\sigma \cot^2 \beta + \csc^2 \beta - \cos 4\sigma) - 3] \right. \\ \left. + Wi [-3 \cos 8\sigma + 12 \cos 4\sigma + 32 \csc^2 \beta (1 - \cos 4\sigma) - 9] \right\}.$$

By symmetry, $D^{\beta\alpha} = D^{\alpha\beta}$, $D^{\gamma\alpha} = D^{\alpha\gamma}$, $D^{\gamma\beta} = D^{\beta\gamma}$. All the other coefficients are zero.

In view of the isotropy of the flow, assume that the stationary PDF of the configuration takes the form $p_{\text{st}}(\mathbf{q}) = \tilde{p}(\sigma) \sin \beta \sin 2\sigma$, where the factor $\sin \beta \sin 2\sigma$ is proportional to the Jacobian of the coordinate transformation from \mathbf{r}_μ to \mathbf{q} (see appendix 2.6.3 for a short explanation). Substituting $p_{\text{st}}(\mathbf{q})$ into Eq. (2.25) results into a Fokker–Planck equation in the variable σ alone:

$$0 = \frac{\partial p_{\text{st}}(\mathbf{q})}{\partial s} = -\frac{\partial}{\partial \sigma} (V^\sigma p_{\text{st}}) + \frac{1}{2} \frac{\partial^2}{\partial \sigma^2} (D^{\sigma\sigma} p_{\text{st}}), \quad (2.36)$$

where $s = t/\tau$. The partial derivatives with respect to the Euler angles indeed cancel each other. Under reflecting boundary conditions at $\sigma = 0$ and $\sigma = \pi/2$, the solution of Eq. (2.36) takes the form given in Eq. (2.34) with modified expressions for V^σ and $D^{\sigma\sigma}$. The exact form of the stationary PDF of the angle σ is derived in three dimensions:

$$\tilde{p}(\sigma) \propto \frac{1}{D^{\sigma\sigma} \sqrt{Wi Z \sin^2 2\sigma + 2}} \left| \frac{C_\sigma^2 - C_+^2}{C_\sigma^2 + C_-^2} \right|^{Z/4C_1} \\ \times \exp \left\{ \frac{Z \sqrt{Wi Z}/2}{2C_1} \left[\frac{\operatorname{arctanh}(C_\sigma/C_+)}{C_+} + \frac{\operatorname{arctan}(C_\sigma/C_-)}{C_-} \right] \right\} \quad (2.37)$$

with $C_\sigma = \sqrt{Wi Z} \cos \sigma$, $C_1 = \sqrt{Wi Z (Wi Z + 2)}/2$, and $C_\pm = \sqrt{C_1 \pm Wi Z}/2$. This can be obtained by following the same integration as in the 2D case (see Sec. 2.6.4). The graph of $\tilde{p}(\sigma)$ is shown in Fig. 2.4. The statistics of the internal angle σ is qualitatively the same for $d = 2$ and $d = 3$ (the curves in Figs. 2 and 3 indeed differ only slightly for the same Wi). This behaviour is attributed to the

fact that the rhombus can only deform in the plane to which it belongs and cannot undergo three-dimensional deformations, which makes its dynamics weakly sensitive to the dimension of the flow.

2.5. Concluding remarks and perspectives

Bead-rod-spring models are the foundation of the kinetic theory of polymer solutions. There is a broad literature on the analytic solutions of these models for laminar flows. In the case of fluctuating flows, such as turbulent flows, analytical results are restricted to dumbbells. Here, a general description of bead-rod-spring models in short-correlated random flows is given and its usage is demonstrated by exactly solving the elastic rhombus model under isotropic conditions. To the best of my knowledge, this is the first instance of an exact solution of a multibead model that include both elastic and rigid links and is transported by a randomly-fluctuating flow. The diffusion equation (2.21) for random flows that is obtained in this chapter will likewise be used for the trumbbell in the succeeding chapter, where bending dynamics will be studied in turbulent flows by using both analytical methods and direct numerical simulations.

A variety of approaches exists to study complex-shaped particles. For instance, several models exist for flexible particles, such as a series of beads connected by inertialess rodes (possibly freely-jointed) [10], a series of rods [94], or as a flexible beam as used in slender body theory [63]. It would be noteworthy to establish a comparison between models that aim to describe the same particle, and consider the availability and potential extension of each model to more general situations.

It is hoped that the tools developed in this chapter will stimulate new studies on the dynamics of complex-shaped particles in turbulent flows. For instance, the rhombus model (or a variant of it) could be used to examine how deformability influences the alignment and orientation statistics of microscopic particles in turbulent flows [73]. The stretching dynamics of bead-spring chains has also received attention in the context of nonequilibrium statistical mechanics [24]; the probability of work and entropy production have been studied for laminar gradient flows [61, 90, 100, 103]. It would be interesting to generalize those studies to the case considered here, where the velocity gradient is a tensorial noise (see, e.g., Ref. [20]).

2.6. Appendices

2.6.1. Components of a random flow. In the classical work [84], Robertson derived that the form of the tensor \mathbf{R} that gives the velocity correlation

$$R_{ik} = \frac{\langle u_i(\mathbf{x})u_k(\mathbf{x}') \rangle}{\langle \mathbf{u}^2 \rangle} \quad (2.38)$$

between the i th component of the velocity $\mathbf{u}(\mathbf{x})$ and the k th component of $\mathbf{u}(\mathbf{x}')$ (of two points \mathbf{x}, \mathbf{x}' in space) under the assumption of isotropic, homogenous, and parity-invariant turbulence is

$$R_{ik}(\mathbf{r}) = Q_1(r)r_i r_k + Q_2(r)\delta_{ik}, \quad (2.39)$$

where $Q_i(r)$ are even functions of the distance $r = |\mathbf{x} - \mathbf{x}'|$ between the two points. If the flow is incompressible, then $\partial R_{ik}/\partial x_k = 0$. Taking the divergence of the

preceding equation yields

$$0 = r \frac{\partial Q_1}{\partial r} + (d+1)Q_1 + \frac{1}{r} \frac{\partial Q_2}{\partial r}. \quad (2.40)$$

It is assumed that $Q_i(r)$ takes the form $Q_i(r) = \alpha_i r^2 + \beta_i$ because r is assumed to be much smaller than the relevant dissipation length scales. This yields

$$\alpha_1 = 0, \quad (2.41)$$

$$\alpha_2 = -\frac{\beta_1}{2}(d+1), \quad (2.42)$$

which is obtained by equating the constants and the coefficients of r^2 . Moreover, $\beta_2 = 1$ since $R_{ik}(0) = \delta_{ik}$. Hence, Eq (2.39) becomes

$$R_{ik}(\mathbf{r}) = \delta_{ik} - \frac{\beta_1}{2} [(d+1)\delta_{ik}r^2 - 2r_i r_k]. \quad (2.43)$$

The correlation of the velocity gradients $\nabla \mathbf{u}$ can be derived to be

$$\mathcal{K}_{ijkl}\delta(t-t') = \langle \partial_j u_i(x, t) \partial_l u_k(x', t') \rangle = -\partial_j \partial_l R_{ik}(\mathbf{0})\delta(t-t'), \quad (2.44)$$

and hence, \mathcal{K} takes the form

$$\mathcal{K}_{ijkl} = \beta_1 [(d+1)\delta_{ik}\delta_{jl} - \delta_{ij}\delta_{kl} - \delta_{il}\delta_{jk}], \quad (2.45)$$

where the coefficient β_1 is proportional to the Lyapunov exponent λ of the flow [35].

2.6.2. Lyapunov exponent of a flow. The Lyapunov exponent λ of a flow characterizes the average exponential growth rate of the distance between two particles in a flow. Suppose that two particles are separated by $\mathbf{R}(t)$. Then

$$\lambda = \lim_{t \rightarrow \infty} \left\langle \ln \frac{|\mathbf{R}(t)|}{|\mathbf{R}(0)|} \right\rangle, \quad (2.46)$$

where the average is taken over all particle pairs. A positive Lyapunov exponent means that on average the distance between two particles grows exponentially with time. It is thus used as an indicator and a measure of the chaoticity of a flow. In contrast, a negative Lyapunov exponent implies that the particles tend to coalesce. This exponent can be measured in numerical simulations, for instance, by performing averages of particle pair separations normalized with respect to their initial configuration, or by performing a QR algorithm [68].

2.6.3. Jacobian. Additional details on how to obtain the determinant J of the Jacobian matrix are given, where the transformation is from the Cartesian to the angular coordinates of the elastic planar rhombus model both in two and in three dimensions. The derivation for the Jacobian of the trumbbell model can be obtained similarly by associating χ with 2σ . Without loss of generality, let the centre of mass be the origin.

The rhombus is fully determined by specifying two of the vectors \mathbf{r}_ν , say \mathbf{r}_1 and \mathbf{r}_2 as in Eqs. (2.28),(2.29). This is equivalent, by some linear transformation, to specifying the two rods $\boldsymbol{\rho}_1 = \mathbf{r}_1 - \mathbf{r}_2 = \mathbf{x}_1 - \mathbf{x}_2$ and $\boldsymbol{\rho}_3 = \mathbf{r}_3 - \mathbf{r}_2 = \mathbf{x}_3 - \mathbf{x}_2$ that connect the beads. In two dimensions, these rods have four degrees of freedom and can be expressed as a function of $\mathbf{q} = \{\theta, \sigma, \rho_1, \rho_3\}$, where ρ_1 and ρ_3 specify the lengths of the rods and will later be considered as constants. Let \mathbf{p} be a vector whose components are the concatenated components of $\boldsymbol{\rho}_1, \boldsymbol{\rho}_3$. The Jacobian matrix $\partial p_i / \partial q_j$ is then calculated by first expressing each component of \mathbf{p} in terms of \mathbf{q}

using Eqs. (2.28),(2.29). The determinant of this Jacobian matrix is $\rho_1\rho_2 = \ell^2$. The Jacobian is then set, in two dimensions, to $J = 1$, and the constants will go into the normalization factor.

In three dimensions, the rods have six degrees of freedom and \mathbf{q} is taken to be $\mathbf{q} = \{\alpha, \beta, \gamma, \sigma, \rho_1, \rho_3\}$. In this case, the orientation vectors of the rods are expressed as

$$\boldsymbol{\rho}_1 = \rho_1(\sin \sigma \boldsymbol{\Sigma}_2 - \cos \sigma \boldsymbol{\Sigma}_1) \quad (2.47)$$

$$\boldsymbol{\rho}_3 = \rho_3(-\cos \sigma \boldsymbol{\Sigma}_1 - \sin \sigma \boldsymbol{\Sigma}_2) \quad (2.48)$$

where $\boldsymbol{\Sigma}_1$ and $\boldsymbol{\Sigma}_2$ are the first two rows, respectively, of the rotation matrix (1.23) that puts the plane on which the rhombus resides in as the new \mathbf{y} and \mathbf{z} axes. With \mathbf{p} defined as above, the Jacobian matrix $\partial p_i/\partial q_j$ is obtained and, after stipulating that ρ_1 and ρ_3 are constants, J is solved to be proportional to $\sin \beta \sin 2\sigma$.

2.6.4. Details of calculation in 2D. The details of the calculation of the stationary PDF in the 2D case is shown here. Note that from Eq. (2.34),

$$p_{\text{st}}(\sigma) \propto \frac{1}{D^{\sigma\sigma}(\sigma)} \exp\left(2 \int_0^\sigma \frac{V^\sigma(x)}{D^{\sigma\sigma}(x)} dx\right) \quad (2.49)$$

with

$$V^\sigma(x) = -\frac{1}{2}(\sqrt{2} - 2 \cos x) \sin x,$$

$$D^{\sigma\sigma}(x) = \frac{1}{Z} + \frac{Wi(1 - \cos 4x)}{2} = \frac{2 - Wi Z(8 \cos^4 x - 8 \cos^2 x)}{2Z}.$$

The main goal is to integrate the inner integral

$$\int \frac{V^\sigma(x)}{D^{\sigma\sigma}(x)} dx = \int_0^\sigma -\frac{Z(\sqrt{2} - 2 \cos x) \sin x}{2 - Wi Z(8 \cos^4 x - 8 \cos^2 x)} dx. \quad (2.50)$$

After substituting $u = \sqrt{2} \cos x$, the integral is then split into the sum

$$\int \frac{V^\sigma(x)}{D^{\sigma\sigma}(x)} dx = \text{I} + \text{II} \quad (2.51)$$

where

$$\text{I} = \frac{Z}{2} \int \frac{u}{Wi Z(u^2 - 1)^2 - (1 + Wi Z)} du \quad (2.52)$$

$$\text{II} = -\frac{Z}{2} \int \frac{1}{Wi Z(u^2 - 1)^2 - (1 + Wi Z)} du. \quad (2.53)$$

By using a substitution $v = u^2 - 1$ and Eq. (3.3.23) in Ref. [1], the integral I can be solved to be

$$\begin{aligned} \text{I} &= -\frac{Z}{4} \int \frac{1}{(Wi Z + 1) - Wi Z v^2} dv \\ &= -\frac{Z}{8\sqrt{Wi Z(Wi Z + 1)}} \ln \left| \frac{\sqrt{Wi Z + 1} + \sqrt{Wi Z} v}{\sqrt{Wi Z + 1} - \sqrt{Wi Z} v} \right| \\ &= -\frac{Z}{8\sqrt{Wi Z(Wi Z + 1)}} \ln \left| \frac{\sqrt{Wi Z + 1} + \sqrt{Wi Z}(2 \cos^2 x - 1)}{\sqrt{Wi Z + 1} - \sqrt{Wi Z}(2 \cos^2 x - 1)} \right| \end{aligned}$$

$$= \frac{Z}{4C_1} \ln \left| \frac{C_\sigma^2 - C_+^2}{C_\sigma^2 - C_-^2} \right|, \quad (2.54)$$

where the last step involves various algebraic manipulations and substitutions using the auxiliary variables

$$C_\sigma = \sqrt{2WiZ} \cos x, \quad (2.55)$$

$$C_1 = \sqrt{WiZ(WiZ + 1)}, \quad (2.56)$$

$$C_\pm = \sqrt{C_1 \pm WiZ}. \quad (2.57)$$

The other integral II can be integrated by first rewriting $B^2 = 1 + \frac{1}{WiZ}$:

$$\begin{aligned} \text{II} &= -\frac{1}{2Wi} \int \frac{1}{(u^2 - 1)^2 - B^2} du \\ &= -\frac{1}{4BWi} \int \frac{-1}{u^2 + (B-1)} + \frac{1}{u^2 - (B+1)} du. \end{aligned} \quad (2.58)$$

Since $B > 1$, the first term will have arctan as its antiderivative. The second term will require Eq. (3.3.23) of [1]. Rewriting this in terms of x gives:

$$\text{II} = \frac{1}{4BWi} \left[\frac{\arctan\left(\frac{\sqrt{2}\cos x}{\sqrt{B-1}}\right)}{\sqrt{B-1}} + \frac{1}{2\sqrt{B+1}} \ln \left| \frac{\sqrt{B+1} + \sqrt{2}\cos x}{\sqrt{B+1} - \sqrt{2}\cos x} \right| \right]. \quad (2.59)$$

The relation $\sqrt{B \pm 1}\sqrt{WiZ} = C_\pm$ and the application of Eq. (4.6.22) of Ref. [1] to the second term then gives

$$\text{II} = \frac{Z\sqrt{WiZ}}{2C_1} \left[\frac{\arctan(C_\sigma/C_-)}{C_-} + \frac{\operatorname{arctanh}(C_\sigma/C_+)}{C_+} \right]. \quad (2.60)$$

The sum of Eqs. (2.54) and (2.60) gives the solution of the integral in Eq. (2.49), which gives the PDF in Eq. (2.35). The solution to the three-dimensional case follows similarly.

Bending of semiflexible particles in turbulent flows

3.1. Introduction

The study of hydrodynamic turbulence and turbulent transport has received considerable impulse from the development of experimental, theoretical, and numerical Lagrangian techniques in which the particle is followed along its trajectory and observation is done “from the point-of-view of the particle” [35, 71, 87, 97]. This is in contrast to Eulerian techniques where the trajectories of the particles are seen from a third-person point-of-view. Lagrangian techniques are widely used in various applications to geophysics, astrophysics, and chemical engineering. The translational dynamics of tracer and inertial pointlike particles is, for instance, intimately related to the mixing properties of turbulent flows [4]. Taking cloud formation as an example, turbulent flow in the atmosphere results in increased collision rates and coalescence of smaller particles into larger ones [91]. Mixing is also present in oceans, where it allows a redistribution of salt concentrations and temperature, as evidenced by experimental studies cited in Ref. [96].

In recent years, increasing attention has been drawn to the Lagrangian dynamics in turbulent flows of microscopic objects that possess a complex shape or internal degrees of freedom, such as elastic dumbbells (Refs. [69] and references therein), solid spheroids and ellipsoids [13, 21, 41, 42, 73, 80, 101], crosses and jacks [66], helicoids [44], chiral dipoles [56], as discussed in the introduction to Part I. In this chapter, the Lagrangian statistics of yet another internal degree of freedom that as far as we know had not been explored before, i.e. the ability of a turbulent flow to bend a semiflexible particle, is examined.

As a minimal model, consider the trumbbell, which was introduced and studied in the context of extensional flows in Chap. 1. As a simple semiflexible object, it was verified that the trumbbell reproduces a coiling and stretching behaviour in a shear flow that manifests as a transition between extended and folded states and a tumbling motion occurring only in the folded state. Here, the trumbbell is regarded as a simple model that allows the isolation of the bending dynamics of a semiflexible particle from the evolution of other potential degrees of freedom. This approach thus gives the probability distribution function (PDF) of the bending angle analytically for laminar and random flows and numerically for fully-developed turbulence.

The stationary statistics of the bending internal angle will be shown to depend strongly on the dimension of the flow and on its turbulent character. In a two-dimensional (2D) homogeneous and isotropic, incompressible turbulent flow, the distribution of the bending angle is bimodal; the configurations in which the trumbbell is either extended or folded are most probable, with the folded configuration being the most likely for strong turbulence. By contrast, in three-dimensional (3D) turbulence, the extended configuration dominates and becomes increasingly probable

as the amplitude of the velocity gradient increases. Such a sensitivity of the bending statistics on the flow dimensionality is peculiar to fluctuating flows and is not observed in laminar stretching flows.

In Chap. 1, the orientational dynamics of the trumbbell was studied. This chapter considers the trumbbell in light of its bending dynamics, firstly in a laminar extensional flow in Sec. 3.2. The trumbbell's bending dynamics in both 2D and 3D turbulent flows is then predicted by subjecting it to a short-correlated random flow in Sec. 3.3; the diffusion equation for random flows (2.21) that was derived in the previous chapter is instrumental in this step. In Sec. 3.4, the analytical PDF for the bending angle is compared to the resulting PDFs obtained by performing direct numerical simulations of the trumbbell in 2D and 3D turbulent flows. Concluding remarks and perspectives are given thereafter.

3.2. Bending in the extensional flow

The trumbbell model, previously introduced in Sec. 1.2, is composed of three identical beads connected by two rigid rods. Recall that its configuration in the frame of reference of its center of mass can be described by the angular variables $\mathbf{q} = (\theta, \chi)$ in a two-dimensional space (where θ gives the orientation of one of the rods with respect to the \mathbf{x} axis of the frame of reference and χ is the internal angle) and $\mathbf{q} = (\alpha, \beta, \gamma, \chi)$ in a three-dimensional space (where α, β, γ are the Euler angles that give the orientation of the plane in which the trumbbell resides and χ is again the internal angle). In contrast to Chap. 1, however, the bending angle χ in this chapter is considered to lie in the interval $0 \leq \chi \leq \pi$ only. As before, an elastic hinge at the middle bead opposes the bending of the trumbbell and the force exerted by the hinge is described by a harmonic potential

$$\phi(\chi) = \frac{A}{2}(\chi - \pi)^2 \quad (3.1)$$

for some non-negative constant A that represents the magnitude of the potential. The PDF of \mathbf{q} still satisfies the diffusion equation (1.14) (for laminar flows). The trumbbell is also sufficiently small so that, when in a turbulent flow, the end-to-end length (2ℓ) is smaller than the Kolmogorov length of the flow.

Since a turbulent flow displays stretching locally, the effect of pure steady stretching on the statistics of the bending angle χ is first examined. Consider the trumbbell in a 2D extensional flow (see Fig. 3.1):

$$\mathbf{u} = \lambda(x, -y), \quad \lambda > 0.$$

Since the velocity gradient $\kappa_{ij} = \partial_j u_i$ satisfies $\boldsymbol{\kappa} = \boldsymbol{\kappa}^\top$, the stationary PDF of \mathbf{q} is known analytically and was given in Eq. (1.27). The statistics of χ varies according to the orientation θ of the trumbbell; however, the average effect of the flow can be understood by considering the marginal stationary PDF of χ :

$$\widehat{\Psi}_{\text{st}}(\chi) = J\widehat{\psi}_{\text{st}}(\chi) \quad (3.2)$$

with J the Jacobian of the transformation from the Cartesian to the angular coordinates ($J = 1$ in two dimensions and $J = \sin \chi \sin \beta$ in three dimensions as in Chap. 1) and

$$\widehat{\psi}_{\text{st}}(\chi) \propto \psi_0(\chi) \exp \left[-\frac{Z}{2}(\pi - \chi)^2 \right] I_0 \left(\frac{Z W_i}{3}(1 - 2 \cos \chi) \right), \quad (3.3)$$

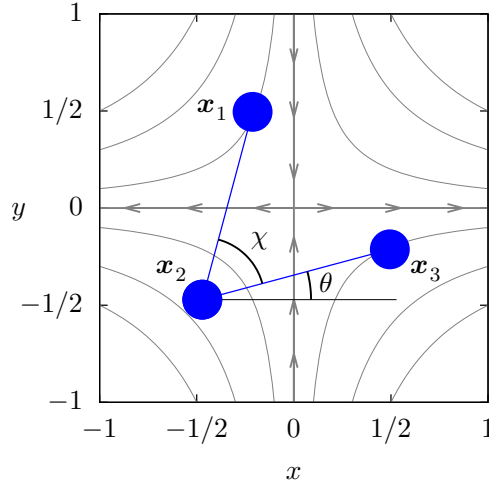


FIGURE 3.1. A trumbbell in an extensional flow (streamlines shown in gray) with stretching in the x - and compression in the y -direction.

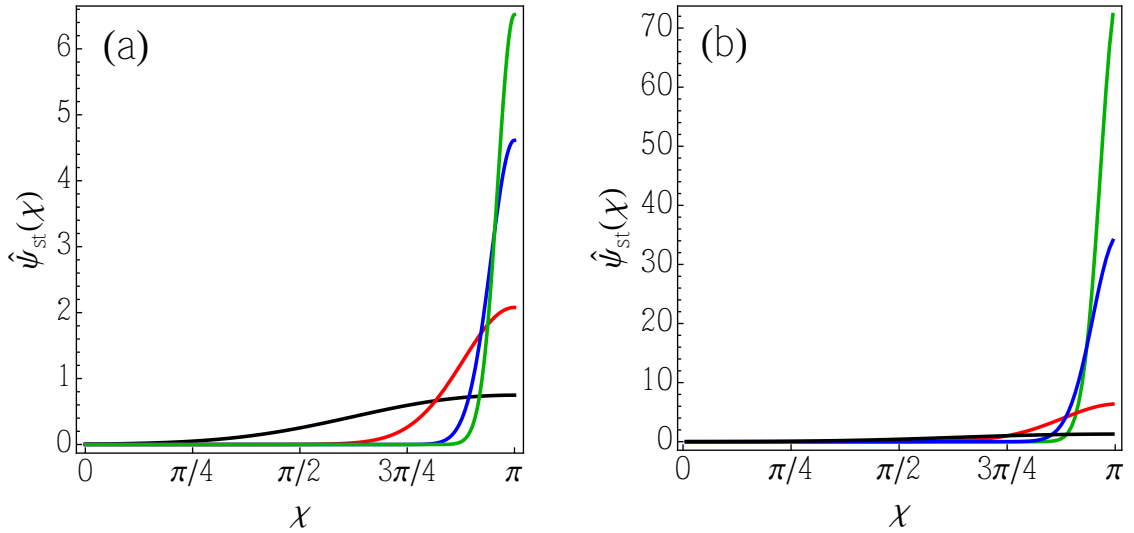


FIGURE 3.2. Extensional flow : $\hat{\psi}_{st}(\chi)$ (a) for $d = 2$ and (b) $d = 3$ and $Z = 1$, $Wi = 0$ (black), $Wi = 10$ (red), $Wi = 50$ (blue), $Wi = 100$ (green).

where I_0 is the modified Bessel function of the first kind of order 0,

$$\psi_0(\chi) \propto \sqrt{4 - \cos^2 \chi},$$

and the stiffness parameter Z and the Weissenberg number $Wi = \lambda\tau$ are as defined in Eqs. (1.23),(1.24) (τ is the characteristic time scale of the restoring potential). The product of Z and Wi yields the Péclet number Pe , as in (1.25). On average the 2D extensional flow favors the $\chi = \pi$ configuration, with this effect becoming stronger as Wi increases (see Fig. 3.2(a)). The linear stability analysis performed in Sec. 1.4 indeed shows that when the flow dominates over the restoring potential ($Wi \gg 1$) and thermal noise is disregarded, both the folded and the extended configurations are

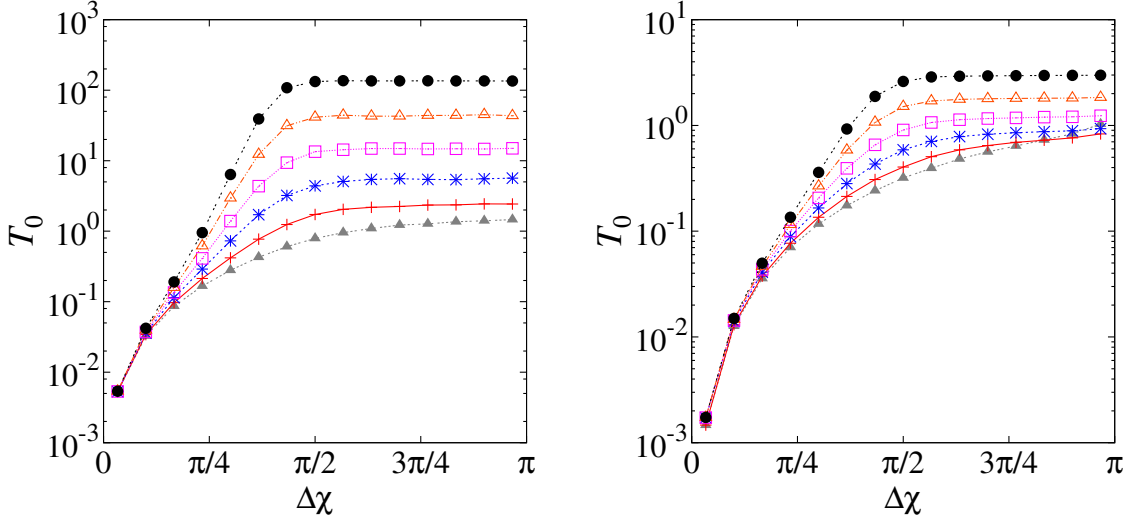


FIGURE 3.3. Extensional flow : T_0 vs $\Delta\chi$ for (a) $d = 2$, $Z = 0$ and from bottom to top $Pe = 4, 8, 12, 16, 20, 24$; (b) $d = 3$ and the same values of Z and Pe as in (a).

stable and their stability improves with increasing Wi , but the latter configuration is more attractive than the former for all Wi . For a 3D uniaxial extensional flow

$$\mathbf{u} = \lambda \left(x, -\frac{y}{2}, -\frac{z}{2} \right), \quad \lambda > 0,$$

the stationary PDF $\widehat{\psi}_{\text{st}}(\chi)$ can again be calculated by using $\boldsymbol{\kappa} = \boldsymbol{\kappa}^T$. It is shown in Fig. 3.2(b). Clearly, $\widehat{\psi}_{\text{st}}(\chi)$ has a similar shape in two and in three dimensions.

An inspection of the temporal dynamics of the trumbbell however reveals a strong dependence on the dimension of the flow. To illustrate this point, consider the situation in which the flow dominates over the restoring force ($Wi \gg 1$, $Z = 0$) and study the temporal evolution of $\chi(t)$ as a function of Pe . In particular, it is useful to analyze the first-passage time

T_0 : the average time it takes for an initially folded trumbbell ($\chi = 0$) to exit the interval $(0, \Delta\chi)$

The value of T_0 for various values of Pe is shown in Fig. 3.3 as a function of $\Delta\chi$. The time T_0 is calculated through a Monte Carlo simulation of the stochastic differential equations that govern the Lagrangian dynamics of the trumbbell for $d = 2$ and $d = 3$ (see Sec. 1.5). The first-passage time T_0 behaves similarly for $d = 2$ and $d = 3$.

- i. For small values of $\Delta\chi$, $T_0 \propto (\Delta\chi)^2$ because the dynamics is dominated by Brownian motion,
- ii. it keeps increasing as a function of $\Delta\chi$ until $\Delta\chi \approx \pi/2$;
- iii. it then becomes independent of $\Delta\chi$, because the average time required to completely unfold a trumbbell with $\chi > \pi/2$ is much shorter than the time it takes to unfold an initially folded trumbbell up to $\chi \approx \pi/2$.

However, for comparable values of Pe , the time T_0 is at least one order of magnitude longer in two dimensions than in three. The reason for this difference is geometrical: for $d = 2$ the degrees of freedom of the trumbbell are two, whereas they are four for $d = 3$; hence in the latter case it is easier for thermal noise to move the system away from the folded configuration. Such dependence of the dynamics on the spatial

dimension d does not affect the shape of $\widehat{\psi}_{\text{st}}(\chi)$ (see Fig. 3.2), because the velocity gradient $\boldsymbol{\kappa}$ is constant in time and the system has the time to evolve to its stationary configuration. However, the flow dimension may impact the stationary statistics of χ in a turbulent flow since $\boldsymbol{\kappa}$ fluctuates in such a flow.

3.3. Bending in a random flow

In order to investigate if the the dimension of the flow affects the statistics of the bending angle χ analytically, the trumbbell is subjected to the Kraichnan random flow in the Batchelor regime [55]. The same flow was used in the previous chapter to predict the configuration of an elastic planar rhombus in a turbulent flow (see Sec. 2.4). The velocity gradient is a δ -correlated-in-time ($d \times d$)-dimensional Gaussian stochastic process with zero mean and correlation: $\langle \kappa^{ij}(t) \kappa^{kl}(t') \rangle = \mathcal{K}^{ijkl} \delta(t - t')$, where

$$\mathcal{K}^{ijkl} = \frac{2\lambda}{d(d-1)} [(d+1)\delta^{ik}\delta^{jl} - \delta^{ij}\delta^{kl} - \delta^{il}\delta^{jk}] \quad (3.4)$$

and λ is now the Lyapunov exponent of the flow. The form of the tensor \mathcal{K} ensures that the flow is incompressible and statistically isotropic (see appendix 2.6.1 of the previous chapter). Let $P(\mathbf{q}; t)$ be the normalised PDF of the configuration of the trumbbell with respect to the realizations both of $\boldsymbol{\kappa}(t)$ and of thermal noise ($\int P(\mathbf{q}; t) d\mathbf{q} = 1$). Thanks to the lengthy calculations in Chap. 2 for general bead-rod-spring models, the diffusion equation (2.21) in a stochastic flow can be readily used for the trumbbell.

First consider the trumbbell in the 2D case. By using the angular variables $\mathbf{q} = (\theta, \chi)$ and the corresponding coefficient \mathbf{G} , Eq. (2.21) can be rewritten as a FPE in θ and χ . The drift and diffusion coefficients, however, do not depend on the absolute orientation θ but only on the internal angle χ because of statistical isotropy. Hence the stationary PDF of the configuration is a function of χ alone and so is the stationary solution of the following FPE:

$$\frac{\partial P}{\partial s} = -\frac{\partial}{\partial \chi}(VP) + \frac{1}{2} \frac{\partial^2}{\partial \chi^2}(DP), \quad (3.5)$$

with $s = t/\tau$, the drift term as

$$V(\chi) = \frac{12 \sin \chi}{Z(2 - \cos \chi)(2 + \cos \chi)^2} + \frac{6(\pi - \chi)}{(2 + \cos \chi)} + 2Wi \frac{\sin \chi [5 + \cos \chi - 11 \cos(2\chi) - \cos(3\chi)]}{(2 - \cos \chi)(2 + \cos \chi)^3}, \quad (3.6)$$

and the diffusion term as

$$D(\chi) = \frac{12}{Z(2 + \cos \chi)} + 16Wi \frac{\sin^2 \chi}{(2 + \cos \chi)^2}, \quad (3.7)$$

where now the Weissenberg number $Wi = \lambda\tau$ depends on the Lyapunov exponent λ . It is remarked that the other drift and diffusion coefficients are not all zero but they are unreported since under isotropic conditions the general FPE in \mathbf{q} (i.e. of a similar form to Eq. (1.20)) reduces to Eq. (3.5). The stationary solution of Eq. (3.5)

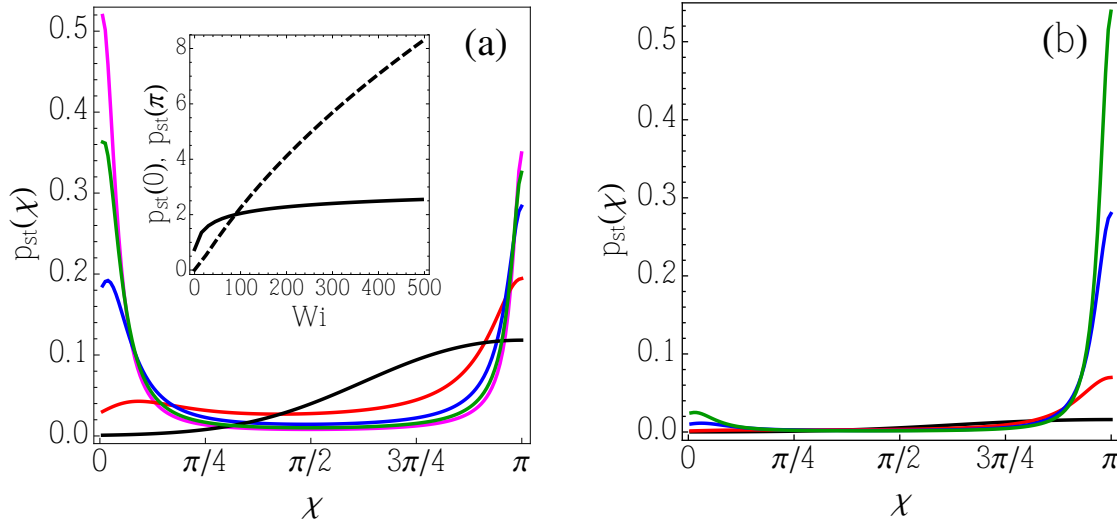


FIGURE 3.4. Batchelor-Kraichnan flow: (a) $p_{\text{st}}(\chi)$ for $d = 2$, $Z = 1$, and $Wi = 0$ (black), $Wi = 10$ (red), $Wi = 50$ (blue), $Wi = 100$ (green), $Wi = 150$ (magenta). The inset shows the values of $p_{\text{st}}(\chi)$ at $\chi = 0$ (dashed line) and $\chi = \pi$ (solid line) vs Wi ; (b) $p_{\text{st}}(\chi)$ for $d = 3$ and the same values of Z and Wi as in (a).

that satisfies periodic boundary conditions is [83]:

$$P_{\text{st}}(\mathbf{q}) = J p_{\text{st}}(\chi) \propto \frac{1}{D(\chi)} \exp\left(2 \int_0^\chi \frac{V(\eta)}{D(\eta)} d\eta\right). \quad (3.8)$$

The function $p_{\text{st}}(\chi)$ is plotted in Fig. 3.4(a) for different values of Wi . For small Wi , the most probable configuration is the $\chi = \pi$ one, as in the hyperbolic flow. However, as Wi increases, a second peak emerges near $\chi = 0$, while intermediate values of χ become less and less probable. At large Wi , $p_{\text{st}}(\chi)$ consists of two narrow peaks, one at $\chi = \pi$ and the other approaching $\chi = 0$, with the latter becoming more and more pronounced with increasing Wi .

In three dimensions, the same approach is done. The previously-derived diffusion equation Eq. (2.21) can once again be rewritten as a FPE for the trumbbell in a random flow, this time in the variables $\mathbf{q} = \{\alpha, \beta, \gamma, \chi\}$, where the first three angles give the orientation in space and χ is the bending angle. Owing to statistical isotropy, $P_{\text{st}}(\mathbf{q})$ is again the stationary solution of a FPE (3.5) in the variable χ alone (the other unreported coefficients cancel each other when the general FPE is simplified) and takes the form in Eq. (3.8) with

$$V(\chi) = \frac{3[4 + 13 \cos \chi - 4 \cos(2\chi) - \cos(3\chi)]}{2Z \sin \chi (2 - \cos \chi) (2 + \cos \chi)^2} + \frac{6(\pi - \chi)}{(2 + \cos \chi)} + Wi \frac{\sin \chi [63 \cos \chi - 15 \cos(3\chi) + 296 \sin^2 \chi]}{12(2 - \cos \chi)(2 + \cos \chi)^3} \quad (3.9)$$

and

$$D(\chi) = \frac{12}{Z(2 + \cos \chi)} + 26 Wi \frac{\sin^2 \chi}{3(2 + \cos \chi)^2}. \quad (3.10)$$

Figure 3.4(b) shows that a tiny peak at $\chi = 0$ emerges only for very large Wi and the $\chi = \pi$ configuration prevails for all Wi . Thus, the statistics of χ is different in two and in three dimensions. In particular only for $d = 3$ is the behaviour of $p_{\text{st}}(\chi)$ similar to that found for the extensional flow.

The difference in the stationary statistics of χ for $d = 2$ and $d = 3$ can again be understood by assuming $Wi \gg 1$ and $Z = 0$ and by considering the first-passage time from a folded configuration T_0 (from the previous section) and the first-passage time from an extended configuration, i.e.

T_π : the mean time it takes for an initially extended trumbbell ($\chi = \pi$) to exit the interval $(\pi - \Delta\chi, \pi)$ through the left.

The ratio T_0/T_π is plotted in Fig. 3.5 as a function of $\Delta\chi$ for increasing Pe . The first-passage times T_0 and T_π are calculated from a numerical simulation of the Itô SDE

$$\dot{\chi} = V(\chi) + \sqrt{D(\chi)}\xi(t) \quad (3.11)$$

associated to the FPE (3.5) for $d = 2$ (using Eqs. (3.6) and (3.7)), and the SDE on $\cos \chi$

$$\frac{d}{dt}(\cos \chi) = -\sin \chi V(\chi) - \frac{1}{2} \cos \chi D(\chi) - \sin \chi \sqrt{D(\chi)}\xi(t) \quad (3.12)$$

for $d = 3$ (using Eqs. (3.9),(3.10)). For $d = 3$, $\cos \chi$ is evolved instead of χ because the drift term (3.9) of $\dot{\chi}$ becomes singular when $\chi = 0$ because of a $\sin \chi$ in the denominator. In both $d = 2, 3$, $\xi(t)$ is white noise.

For small $\Delta\chi$, $T_0 > T_\pi$ both for $d = 2$ and $d = 3$, because in the folded configuration the end beads have very similar velocities and it is therefore difficult for the flow to separate them. However, T_0/T_π is greater for $d = 2$ than for $d = 3$; moreover, it grows fast as a function of Pe for $d = 2$ and is almost independent of Pe for $d = 3$. This is because for $d = 2$ the beads are confined to the plane and it is much more difficult for the flow to separate them compared to the 3D case.

When $\Delta\chi \approx \pi$, T_0 and T_π are comparable for $d = 2$, whereas $T_0 \ll T_\pi$ for $d = 3$, i.e., in this case the average time required to completely unfold an initially folded trumbbell is much shorter than that required to fold an initially extended one. The reason for this is once again geometrical; it is indeed more difficult to fold two rods whose orientations fluctuate in a three-dimensional space than to fold two rods that are confined to a plane.

The above discussion explains why, for $d = 2$, $p_{\text{st}}(\chi)$ shows a second peak near to $\chi = 0$ and this peak dominates for a strong flow, whereas $p_{\text{st}}(\chi)$ does not enjoy the same property for $d = 3$.

3.4. Direct numerical simulations

To ensure that the qualitative properties of the statistics of the bending angle χ do not depend on the Gaussianity and temporal decorrelation of the Batchelor–Kraichnan flow, Lagrangian direct numerical simulations of the trumbbell model in 2D and 3D incompressible, isotropic turbulence were performed on a 2π -periodic domain. Since the trumbbells are considered as passive, the code consists of two decoupled parts. First, the velocity gradients are obtained from the evolution of the Navier–Stokes equation by using a standard pseudospectral method; these Lagrangian trajectories are developed in collaboration with S.S. Ray. The second part of the code consists of seeding the flow with 10^5 trumbbells in two dimensions and

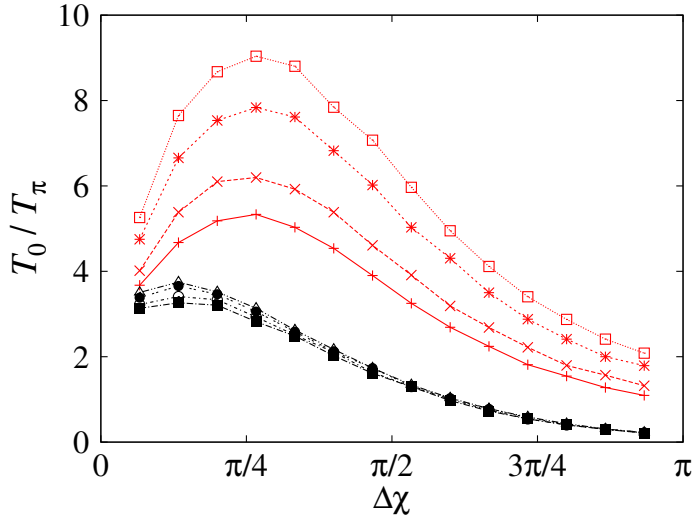


FIGURE 3.5. Batchelor-Kraichnan flow: T_0/T_π vs $\Delta\chi$ for $d = 2$ (red) and $d = 3$ (black), $Z = 0$, and from bottom to top $Pe = 30, 50, 100, 150$.

with 10^6 trumbbells in three dimensions. By coupling the Lagrangian velocity gradients obtained from the pseudospectral method to the Lagrangian code simulating the SDEs for the configuration of the trumbbell (the same code used in Chap. 1), the statistics of χ is then computed. Further details on the pseudospectral method used, how the Lagrangian trajectories are obtained, and how the Lyapunov exponent of the flow is calculated from it are available in the appendix of this chapter.

The Weissenberg number of the turbulent flow is defined in the same manner as for the random flow, i.e., $Wi = \lambda\tau$, where now λ is the Lyapunov exponent of the turbulent flow in the simulations. The numerical results shown in Fig. 3.6 confirm the predictions based on the Batchelor-Kraichnan flow. In particular, for $d = 2$, the $\chi = \pi$ configuration is favoured at small Wi . As Wi increases, the probability of a folded configuration grows significantly and eventually, at extremely large Wi , $p_{st}(\chi)$ displays strong peaks at $\chi \approx 0$ and $\chi \approx \pi$, with the former peak prevailing over the latter. For $d = 3$, $p_{st}(\chi)$ has a maximum at $\chi = \pi$, which grows with increasing Wi ; a very small peak near to $\chi = 0$ only appears for very large Wi .

3.5. Concluding remarks and perspectives

The bending statistics of semiflexible particles has been studied in laminar and turbulent flows by considering the trumbbell as a minimal model. In both 2D and 3D laminar extensional flows, two stable configurations of the trumbbell are found, albeit one is much more dominant than the other, thereby producing a PDF strongly skewed with a preference for the extended configuration. To predict the trumbbell's bending behaviour in turbulent flows it was subjected to a short-correlated random flow; a difference in the PDFs between $d = 2$ and $d = 3$ manifested for large values of Wi by the appearance of a second (even higher) peak in the folded $\chi = 0$ configuration in the 2D case, whereas the 3D flow revealed a PDF essentially similar to the laminar case. Finally, direct numerical simulations confirm the analytical predictions that the stationary distribution of the bending internal angle depends strongly on whether the flow is laminar or turbulent and, in the turbulent case, is sensitive to the flow

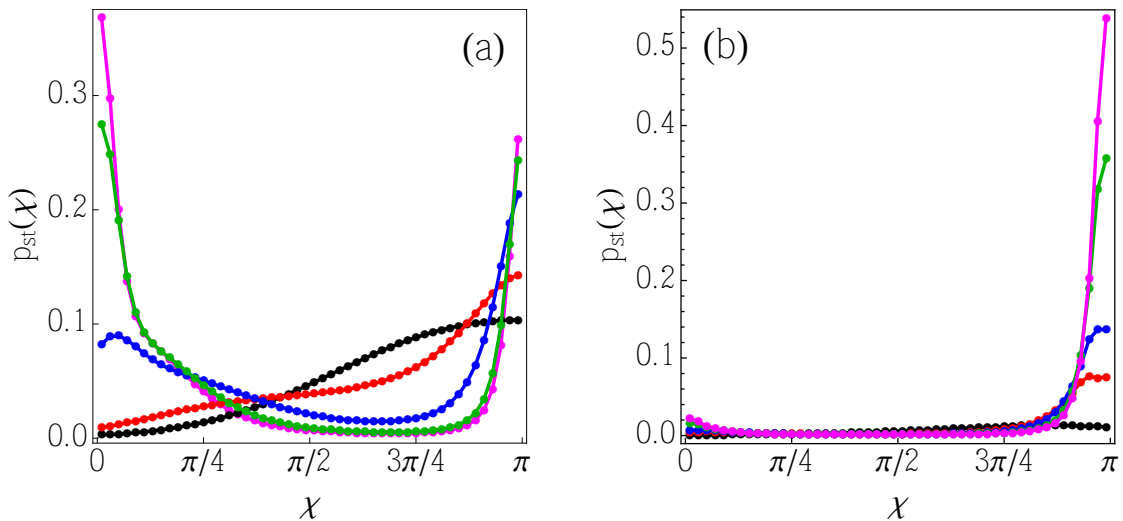


FIGURE 3.6. Homogeneous isotropic turbulence: (a) $p_{st}(\chi)$ for $d = 2$, $Z = 1$, and $Wi = 0.04$ (black), $Wi = 17.53$ (red), $Wi = 45.3$ (blue), $Wi = 54$ (green), $Wi = 102$ (magenta); (b) $p_{st}(\chi)$ for $d = 3$, $Z = 1$, and $Wi = 3.3$ (black), $Wi = 26.3$ (red), $Wi = 49.3$ (blue), $Wi = 131.4$ (green), $Wi = 197.1$ (magenta).

dimensionality. This behaviour is explained in terms of the first-passage times from the folded and the extended configurations of the trumbbell.

These results suggest that the rheology of suspensions of semiflexible particles may also exhibit an analogous strong dependence on the properties of the flow. For instance, the two-peaked PDF in a 2D turbulent flow suggest frequent folding and unfolding, which may in turn exert more stress on the flow. How would a suspension behave differently between two and three dimensions in the presence of these bending and unbending particles? The advent of 3D printing coupled with the Lagrangian experimental techniques of following particles allow the observation of complex particle dynamics and deformation even in turbulent flows [97]; it would be desirable to confirm the effect of dimensionality reported here. Furthermore, a generalization to particles with multiple bending modes or a comparison with actin filaments and elastic fibers will prove instrumental in characterizing the bending dynamics of semiflexible particles [63]. Indeed it is hoped this work would lead to further experiments directed towards the study of the Lagrangian dynamics of semiflexible particles in turbulent flows and the non-Newtonian properties of turbulent suspensions of such particles.

3.6. Appendix

The pseudospectral method performs a portion of the evolution of a PDE in the spectral space with the aim of simplifying the calculations, in particular, differentiation. Multiplications are however done in real space because they become convolutions, and hence more costly, in spectral space. The cost in computation will then largely involve performing the Fourier and inverse Fourier transforms of the variables. In both simulations, the 2/3-dealiasing rule was used to avoid misrepresenting the flow which may occur due to the nonlinear terms: the multiplication of two or more functions in real space may result in the activation of modes higher than

those that can be represented in the Fourier modes, and these larger modes manifest as additional input in the smaller modes.

The codes themselves may involve several optimisations and various technical details, some of which are detailed below. The code in two dimensions, for instance, works via the stream function $\psi = \nabla^{-1}\omega$, where $\omega = |\nabla \times \mathbf{u}|$ is the vorticity of the incompressible velocity field \mathbf{u} . The Navier–Stokes equation is then considered in the following form:

$$\partial_t \omega + \mathcal{J}(\psi, \omega) = \nu \Delta \omega + f - a\omega \quad (3.13)$$

where $\mathcal{J}(\psi, \omega) = (\partial_x \psi)(\partial_y \omega) - (\partial_x \omega)(\partial_y \psi)$, ν is the kinematic viscosity ($\nu = 10^{-5}$), f is a forcing (in this case, the force term was $f(x, y) = -F_0 k_f \cos(k_f x)$ injected at wavenumber $k_f = 4$ and with amplitude $F_0 = 5 \times 10^{-3}$), and the last term is an air-drag induced Ekman friction (coefficient set to $a = 0.01$). An initial vorticity ω in Fourier space is given and then evolved using the equation in Fourier space by using a time integrator. A second-order (exponential) Runge–Kutta method was used: Each timestep dt involves two steps. First, an intermediate value $\hat{\omega}(k)$ of the vorticity (in the Fourier space, hence k) is obtained by advancing only with $dt/2$. Then, by using the updated intermediate value of the velocity $\hat{\mathbf{u}}$ associated to $\hat{\omega}$, the new value of ω can be obtained by evolving the intermediate value by another $dt/2$. Each $dt/2$ -step requires performing an inverse Fourier of the velocities to perform the multiplication in real space and a Fourier transform of the product to obtain the (intermediate) value of $\hat{\omega}$. The force term is only added at the end of each timestep dt and is done in real space. The velocity can then be computed from the vorticity via the spectral form of the relation $\mathbf{u} = (-\partial_y \psi, \partial_x \psi)$ together with the relation $\hat{\psi}(k) = k^{-2} \hat{\omega}(k)$. The choice of the parameters [74, 82] yields a Taylor-microscale Reynolds number $Re_{\text{Tay}} = u_{\text{rms}} l_{\text{Tay}} / \nu = 827$, $l_{\text{Tay}} = 0.1$ in the non-equilibrium, statistically steady state, where u_{rms} is the root-mean-square of the velocity and l_{Tay} is the Taylor microscale (the Taylor-microscale Reynolds number is written as Re_{Tay} and not the more common Re_λ because λ is defined in this chapter as the Lyapunov exponent of the flow). The number of collocation points is 1024^2 .

For $d = 3$, the Navier–Stokes equation

$$\partial_t \mathbf{u} + \mathbf{u} \cdot \nabla \mathbf{u} = -\nabla p + \nu \Delta \mathbf{u} + \mathbf{f}, \quad (3.14)$$

where p is pressure, has been evolved by using the Runge–Kutta method; the kinematic viscosity is set to $\nu = 10^{-3}$. The forcing \mathbf{f} has a fixed energy input and forced at scales less than or equal to $k_f = 2$ such that the mean energy dissipation balances the power input (see Refs. [58, 86] for further details on the forcing and the numerical simulations). The parameters chosen give a Taylor microscale $l_{\text{Tay}} = 0.35$ and the associated Reynolds number $Re_{\text{Tay}} = 121$. A total of 512^3 collocation points were used.

The trumbbell considered is a tracer particle and its transport in space is simply the transport of its centre of mass \mathbf{x}_{CM} . Note that the evolution of \mathbf{x}_{CM} follows Eq. (1.8), but the noise is disregarded because it is negligible compared to the turbulent diffusivity. These Lagrangian trajectories (and their gradients) may then be obtained independently of the trumbbell. The Lagrangian trajectories that advects \mathbf{x}_{CM} may be obtained from the Eulerian velocities calculated above by using a bilinear-interpolation scheme [74, 78, 82]; if \mathbf{x}_{CM} does not lie on a gridpoint, the scheme estimates its velocity by a weighted average of the four nearest gridpoints.

The Weissenberg number of the turbulent flow is defined in the same manner as for the random flow, i.e., $Wi = \lambda\tau$, where now λ is the Lyapunov exponent of the turbulent flow in the simulations. The exponent λ of the turbulent flow is calculated via a QR factorization [26, 68] given the Lagrangian velocities $\mathbf{u}(\mathbf{x}, t)$

$$\dot{\mathbf{x}} = \mathbf{u}(\mathbf{x}, t). \quad (3.15)$$

The QR code factorizes $\nabla\mathbf{u}$ into an orthogonal matrix \mathbf{Q} and an upper triangular matrix \mathbf{R} , and the largest Lyapunov exponent is

$$\lambda = \lim_{t \rightarrow \infty} \left\langle \frac{1}{t} \log R_{11}(t) \right\rangle, \quad (3.16)$$

where the averaging $\langle \cdot \rangle$ is done over the different particle trajectories. This QR factorization is directly performed on the previously-calculated velocity gradients $\nabla\mathbf{u}$.

Bibliography - Part I

- [1] Abramowitz M, Stegun IA. *Handbook of Mathematical Functions*. National Bureau of Standards, U.S. Government Printing Office (1964).
- [2] Ahmad A, Vincenzi D. Polymer stretching in the inertial range of turbulence. *Phys. Rev. E* **93**, 052605 (2016).
- [3] Balkovsky E, Fouxon A, Lebedev V. Turbulent dynamics of polymer solutions. *Phys. Rev. Lett.* **84**, 4765 (2000).
- [4] Bec J, Biferale L, Boffetta G, Cencini M, Musacchio S, Toschi F. Lyapunov exponents of heavy particles in turbulence. *Phys. Fluids* **18**, 091702 (2006).
- [5] Benzi R, L'vov VS, Procaccia I, Tiberkevich V. Saturation of turbulent drag reduction in dilute polymer solutions. *Euroophys. Lett.* **68**, 825 (2004).
- [6] Benzi R, Ching ESC, Lo TS, L'vov VS, Procaccia I. Additive equivalence in turbulent drag reduction by flexible and rodlike polymers. *Phys. Rev. E* **72**, 016305 (2005).
- [7] Berthet H, Fermigier M, Lindner A. Single fiber transport in a confined channel: Microfluidic experiments and numerical study. *Phys. Fluids* **25**, 103601 (2013).
- [8] Biben T, Misbah C. Tumbling of vesicles under shear flow within an advected-field approach. *Phys. Rev. E* **67**, 031908 (2003).
- [9] Biben T, Kassner K, Misbah C. Phase-field approach to three-dimensional vesicle dynamics. *Phys. Rev. E* **72**, 041921 (2005).
- [10] Bird RB, Curtiss CF, Armstrong RC, Hassager O. *Dynamics of Polymeric Liquids*. John Wiley and Sons, Inc. Vol. 2 (1987).
- [11] Bretherton FP. The motion of rigid particles in a shear flow at low Reynolds number. *J. Fluid Mech.* **14**, 284 (1962).
- [12] Brouzet C, Verhille G, Le Gal P. Flexible fiber in a turbulent flow: A macroscopic polymer. *Phys. Rev. Lett.* **112**, 074501 (2014).
- [13] Byron M, Einarsson J, Gustavsson K, Voth G, Mehlig B, Variano E. Shape-dependence of particle rotation in isotropic turbulence. *Phys. Fluids* **27**, 035101 (2015).
- [14] Celani A, Musacchio S, Vincenzi D. Polymer transport in random flow. *J. Stat. Phys.* **118**, 531 (2005).
- [15] Celani A, Puliafito A, Turitsyn K. Polymers in linear shear flow: A numerical study. *Europhys. Lett.* **70**, 464 (2005).
- [16] Celani A, Puliafito A, Vincenzi D. Dynamical slowdown of polymers in laminar and random flows. *Phys. Rev. Lett.* **97**, 118301 (2006).
- [17] Cencini M, Bec J, Biferale L, Boffetta G, Celani A, Lanotte A, Musacchio S, Toschi F. Dynamics and statistics of heavy particles in turbulent flows. *J. Turbulence* **7**, 1 (2006).
- [18] Chertkov M. Polymer stretching by turbulence. *Phys. Rev. Lett.* **84**, 4761 (2000).
- [19] Chertkov M, Kolokolov I, Lebedev V, Turitsyn K. Polymer statistics in a random flow with mean shear. *J. Fluid Mech.* **531**, 251 (2005).

- [20] Chetrite R, Gawędzki K. Fluctuation relations for diffusion processes. *Commun. Math. Phys.* **282**, 469 (2008).
- [21] Chevillard L, Meneveau C. Orientation dynamics of small, triaxial-ellipsoidal particles in isotropic turbulence. *J. Fluid Mech.* **737**, 571 (2013).
- [22] Cruz C, Chinesta F, Réigner G. Review on the Brownian dynamics simulation of bead-rod-spring models encountered in computational rheology. *Arch. Comput. Methods Eng.* **19**, 227 (2012).
- [23] Curtiss CF, Bird RB, Hassager O. Kinetic theory and rheology of macromolecular solutions, in *Adv. Chem. Phys.* **35**, 31 (John Wiley & Sons, NJ, 1976).
- [24] Dhar A. Work distribution functions in polymer stretching experiments. *Phys. Rev. E* **71**, 036126 (2005).
- [25] Diaz FG, Garcia de la Torre J. Simulation of the rotational Brownian dynamics of a simple segmentally flexible model: The elastic trumbbell. *J. Chem. Phys.* **88**, 7698 (1988).
- [26] Dieci L, Russell RD, van Vleck ES. On the computation of Lyapunov exponents for continuous dynamical systems. *SIAM J. Numer. Anal.* **34**, 402 (1997).
- [27] Dupire J, Socol M, Viallat A. Full dynamics of a red blood cell in shear flow. *Proc. Natl Acad. Sci.* **109**, 20808 (2012).
- [28] E W, Vanden-Eijnden E. Transition-path theory and path-finding algorithms for the study of rare events. *Annu. Rev. Phys. Chem.* **61**, 391 (2010).
- [29] E W, Ren W, Vanden-Eijnden E. String method for the study of rare events. *Phys. Rev. B* **66**, 052301 (2002).
- [30] E W, Ren W, Vanden-Eijnden E. Simplified and improved string method for computing the minimum energy paths in barrier-crossing events. *J. Chem. Phys.* **126**, 164103 (2007).
- [31] Einarsson J, Johansson A, Mahata SK, Mishra Y, Angilella JR, Hanstorp D, Mehlig B. Aperiodic tumbling of microrods advected in a microchannel flow. *Acta Mechanica* **224**, 2281 (2013).
- [32] Einarsson J, Candelier F, Lundell F, Angilella JR, Mehlig B. Effect of weak fluid inertia upon Jeffery orbits. *Phys. Rev. E* **91**, 041002(R) (2015).
- [33] Einarsson J, Mihiretie BM, Laas A, Ankardal S, Angilella JR, Hanstorp D, Mehlig B. Tumbling of asymmetric microrods in a microchannel flow. *Phys. Fluids* **28**, 013302 (2016).
- [34] Elgeti J, Winkler RG, Gompper G. Physics of microswimmers—single particle motion and collective behaviour: a review. *Rep. Prog. Phys.* **78**, 056601 (2015).
- [35] Falkovich G, Gawędzki K, Vergassola M. Particles and fields in fluid turbulence, *Rev. Mod. Phys.* **73**, 913 (2001).
- [36] Freidlin MI, Wentzell AD. *Random Perturbations of Dynamical Systems*. Springer (2012).
- [37] Garcia de la Torre J. Hydrodynamics of segmentally flexible macromolecules. *Eur. Biophys. J.* **23**, 307 (1994).
- [38] Gardiner CW. *Handbook of Stochastic Methods*. Springer (1985).
- [39] Gerashchenko S, Chevillard C, Steinberg V. Single-polymer dynamics: Coil-stretch transition in a random flow. *Europhys. Lett.* **71**, 221 (2005).
- [40] Gerashchenko S, Steinberg V. Statistics of tumbling of a single polymer molecule in shear flow. *Phys. Rev. Lett.* **96**, 038304 (2006).
- [41] Gupta A, Vincenzi D, Pandit R. Elliptical tracers in two-dimensional, homogeneous, isotropic fluid turbulence: The statistics of alignment, rotation, and

- nematic order. *Phys. Rev. E* **89**, 021001(R) (2014).
- [42] Gustavsson K, Einarsson J, Mehlig B. Tumbling of small axisymmetric particles in random and turbulent flows. *Phys. Rev. Lett.* **112**, 014501 (2014).
- [43] Gustavsson K, Biferale L. Clustering of chiral particles in flows with broken parity invariance. Proceedings of the 15th European Turbulence Conference (25–28 August, Delft, 2015), N. 103. <http://www.etc15.nl/proceedings/proceedings/documents/103.pdf>.
- [44] Gustavsson K, Biferale L. Preferential sampling of helicity by isotropic helicoids. *Phys. Rev. Fluids* **1**, 054201 (2016).
- [45] Harasim M, Wunderlich B, Peleg O, Kröger M, Bausch AR. Direct observation of the dynamics of semiflexible polymers in shear flow. *Phys. Rev. Lett.* **110**, 108302 (2013).
- [46] Hassager O. Kinetic theory and rheology of bead-rod models for macromolecular solutions. I. Equilibrium and steady flow properties, *J. Chem. Phys.* **60**, 2111 (1974); Kinetic theory and rheology of beadrods models for macromolecular solutions. II. Linear unsteady flow properties, *ibid.* **60**, 4001 (1974).
- [47] Hinch EJ, Leal LG. Rotation of small non-axisymmetric particles in a simple shear flow. *J. Fluid Mech.* **92**, 591 (1979).
- [48] Hinch EJ. Brownian motion with stiff bonds and rigid constraints. *J. Fluid Mech.* **271**, 219 (1994).
- [49] Horel J, Crosman E, Blayblock B, Arens S, Long A, Sohl J. Summer ozone concentrations in the vicinity of the Great Salt Lake. *Atmospheric Sci. Lett.* **17**, 480 (2016).
- [50] Huang CC, Sutmann G, Gompper G, Winkler RG. Tumbling of polymers in semidilute solution under shear flow. *Europhys. Lett.* **93**, 54004 (2011).
- [51] Jeffery GB. The motion of ellipsoidal particles immersed in a viscous fluid. *Proc. R. Soc. Lond. A* **102**, 161 (1922).
- [52] Kantsler C, Steinberg V. Transition to tumbling and two regimes of tumbling motion of a vesicle in shear flow. *Phys. Rev. Lett.* **96**, 036001 (2006).
- [53] Kaya T, Koser H. Characterization of hydrodynamic surface interactions of *Escherichia coli* cell bodies in shear flow. *Phys. Rev. Lett.* **103**, 138103 (2009).
- [54] Kloeden PE, Platen E. *Numerical Solutions of Stochastic Differential Equations*. Springer (1999).
- [55] Kraichnan RH. Small-scale structure of a scalar field convected by turbulence, *Phys. Fluids* **11**, 945 (1968).
- [56] Kramel S, Voth GA, Tymphel S, Toschi F. Preferential rotation of chiral dipoles in isotropic turbulence, *Phys. Rev. Lett.* **117**, 154501 (2016).
- [57] Küchler N, Löwen H, Menzel AM. Getting drowned in a swirl: Deformable bead-spring model microswimmers in external flow fields. *Phys. Rev. E* **93**, 022610 (2016).
- [58] Lamorgese AG, Caughey DA, Pope SB. Direct numerical simulation of homogeneous turbulence with hyperviscosity. *Phys. Fluids* **17**, 015106 (2005).
- [59] Larson RG. *The Structure and Rheology of Complex Fluids*. Oxford University Press (1999).
- [60] Larson RG. The rheology of dilute solutions of flexible polymers: Progress and problems. *J. Rheol.* **49**, 1 (2005).
- [61] Latinwo F, Hsiao K-W, Schroeder CM. Nonequilibrium thermodynamics of dilute polymer solutions in flow. *J. Chem. Phys.* **141**, 174903 (2014).

- [62] Lewis RJ, Allison SA, Eden D, Pecora R. Brownian dynamics simulations of a three-subunit and a ten-subunit worm-like chain: Comparison of results with trumbell theory and with experimental results from DNA. *J. Chem. Phys.* **89**, 2490 (1988).
- [63] Lindner A, Shelley M. Elastic fibers in flows. In *Fluid-Structure Interactions in Low Reynolds-Number Flows* (eds. C. Duprat and H. Stone), pp. 168–192, Royal Society of Chemistry (2016).
- [64] Liu Y, Steinberg V. Single polymer dynamics in a random flow. *Macromol. Symp.* **337**, 34 (2014).
- [65] López HM, Hulin J-P, Auradou H, D'Angelo MV. Deformation of a flexible fiber in a viscous flow past an obstacle. *Phys. Fluids* **27**, 013102 (2015).
- [66] Marcus GG, Parsa S, Kramel S, Ni R, Voth GA. Measurements of the solid-body rotation of anisotropic particles in 3D turbulence. *New J. Phys.* **16**, 102001 (2014).
- [67] Martins Afonso M, Vincenzi D. Nonlinear elastic polymers in random flow. *J. Fluid Mech.* **540**, 99 (2005).
- [68] McDonald EJ, Higham DJ. Error analysis of QR algorithms for computing Lyapunov exponents. *Elec. Trans. on Num. Anal.* **12**, 234 (2001).
- [69] Musacchio S, Vincenzi D. Deformation of a flexible polymer in a random flow with long correlation time. *J. Fluid Mech.* **670**, 326 (2011).
- [70] Öttinger HC. *Stochastic Processes in Polymeric Fluids*. Springer (1996).
- [71] Pandit R, Perlekar P, Ray SS. Statistical properties of turbulence: an overview. *Pramana* **73**, 157 (2009).
- [72] Parsa S, Guasto JS, Kishore M, Ouellette NT, Gollub JP, Voth GA. Rotation and alignment of rods in two-dimensional chaotic flow. *Phys. Fluids* **23**, 043302 (2011).
- [73] Parsa S, Calzavarini E, Toschi F, Voth GA. Rotation rate of rods in turbulent fluid flow. *Phys. Rev. Lett.* **109**, 134501 (2012).
- [74] Perlekar P, Ray SS, Mitra D, Pandit R. Persistence problem in two-dimensional fluid turbulence. *Phys. Rev. Lett.* **106**, 054501 (2011).
- [75] Pham J, Morozov A, Crosby AJ, Lindner A, du Roure O. Deformation and shape of flexible, microscale helices in viscous flow. *Phys. Rev. E*, **92**, 011004(R) (2016).
- [76] Plan ELC VI M, Ali A, Vincenzi D. Bead-rod-spring models in random flows, *Phys. Rev. E*, **94**, 020501(R) (2016).
- [77] Plan ELC VI M, Vincenzi D. Tumbling of a Brownian particle in an extensional flow. *Proc. Royal Soc. A* **472**, 20160226 (2016).
- [78] Press WH, Teukolsky SA, Vetterlin WT, Flannery BP. *Numerical Recipes in Fortran: The Art of Scientific Computing*. Cambridge University Press, Cambridge (1992).
- [79] Puliafito A, Turitsyn K. Numerical study of polymer tumbling in linear shear flows. *Physica D* **211**, 9 (2005).
- [80] Pumir A, Wilkinson M. Orientation statistics of small particles in turbulence. *New J. Phys.* **13**, 093030 (2011).
- [81] Quennoz N, Shelley M, du Roure O, Lindner A. Transport and buckling dynamics of an elastic fibre in a viscous cellular flow. *J. Fluid Mech.* **769** 387(2015).
- [82] Ray SS, Mitra D, Perlekar P, Pandit R. Dynamic multiscaling in two-dimensional fluid turbulence. *Phys. Rev. Lett.* **107**, 184503 (2011).

- [83] Risken H. *The Fokker-Planck Equation*. Springer-Verlag, Berlin/Heidelberg/New York (1989).
- [84] Robertson, HP. The invariant theory of isotropic turbulence. *Math. Proc. Cambridge Phil. Soc.* **36**, 209 (1940).
- [85] Roitman DB. The elastic trumbbell model for dynamics of stiff chains, in *Rotational dynamics of small and macromolecules*, Proceedings of a workshop held at the Zentrum für interdisziplinäre Forschung Universität Bielefeld, Bielefeld, edited by Th. Dormfüller and R. Pecora, Lecture Notes in Physics, Vol. 293, p. 192 (Springer, Berlin Heidelberg, 1987)
- [86] Sahoo G, Perlekar P, Pandit R. Systematics of the magnetic-Prandtl-number dependence of homogeneous, isotropic magnetohydrodynamic turbulence. *New J. Phys.* **13**, 013036 (2011).
- [87] Salazar JPLC, Collins LR. Two-particle dispersion in isotropic turbulent flows. *Annu. Rev. Fluid Mech.* **41**, 405 (2009).
- [88] Schroeder CM, Teixeira RE, Shaqfeh ESG, Chu S. Characteristic periodic motion of polymers in shear flow. *Phys. Rev. Lett.* **95**, 018301 (2005).
- [89] Shaqfeh ESG, Koch DL. Polymer stretch in dilute fixed beds of fibres or spheres. *J. Fluid Mech.* **244**, 17 (1992).
- [90] Sharma R, Cherayil BJ. Work fluctuations in an elastic dumbbell model of polymers in planar elongational flow. *Phys. Rev. E* **83**, 041805 (2011).
- [91] Shaw RA. Particle-turbulence interactions in atmospheric clouds. *Ann. Rev. Fluid Mech.* **35**, 183 (2013).
- [92] Sinha K, Graham MD. Dynamics of a single red blood cell in simple shear flow. *Phys. Rev. E* **92**, 042710 (2015).
- [93] Smith DE, Babcock HP, Chu S. Single-polymer dynamics in steady shear flow. *Science* **283**, 1724 (1999).
- [94] Tanniemola B, Liverpool B. Dynamics of inextensible semiflexible filaments. *Phys. Rev. E* **72**, 021805 (2005).
- [95] Thiffeault J-L. Finite extension of polymers in turbulent flow. *Phys. Lett. A* **308**, 445 (2003).
- [96] Thiffeault J-L. Braids of entangled particle trajectories. *Chaos* **20**, 017516 (2010).
- [97] Toschi F, Bodenschatz E. Lagrangian properties of particles in turbulence. *Annu. Rev. Fluid Mech.* **41**, 375 (2009).
- [98] Touchette H. The large deviation approach to statistical mechanics. *Phys. Rep.* **478**, 1 (2009).
- [99] Turitsyn KS. Polymer dynamics in chaotic flows with a strong shear component. *J. Expl Theor. Phys.* **105**, 3, 655 (2007).
- [100] Turitsyn K, Chertkov M, Chernyak VY, Puliafito A. Statistics of entropy production in linearized stochastic systems *Phys. Rev. Lett.* **98**, 180603 (2007).
- [101] Vincenzi D. Orientation of non-spherical particles in an axisymmetric random flow. *J. Fluid Mech.* **719**, 465 (2013).
- [102] Voth GA and Soldati A. Anisotropic particles in turbulence. *Ann. Rev. Fluid Mech.* **49**, 249 (2017).
- [103] Vucelja M, Turitsyn KS, Chertkov M. Extreme-value statistics of work done in stretching a polymer in a gradient flow. *Phys. Rev. E* **91**, 022123 (2015).
- [104] Walter J, Salsac AV, Barthès-Biesel D. Ellipsoidal capsules in simple shear flow: prolate versus oblate initial shapes. *J. Fluid Mech.* **676**, 318 (2011).

- [105] Watanabe T, Gotoh T. Coil-stretch transition in an ensemble of polymers in isotropic turbulence. *Phys. Rev. E* **81**, 066301 (2010).
- [106] Yarin AL, Gottlieb O, Roisman IV. Chaotic rotation of triaxial ellipsoids in simple shear flow. *J. Fluid Mech.* **340**, 83 (1997).
- [107] Young YN, Shelley SJ. Stretch-coil transition and transport of fibers in cellular flows. *Phys. Rev. Lett.* **99**, 058303 (2007).

Part II

Chaotic dynamics at low Reynolds number

Introduction

In the experiment performed by Groisman and Steinberg [36], a viscous sugar syrup is injected with a dilute solution (80 ppm by weight) of high-molecular-weight polyacrylamide and placed in between two concentric parallel plates that are 10 mm apart from each other (see Fig. II.1(a)); the lower plate of diameter 43.6 mm is fixed while the upper plate of diameter 38 mm is rotating. By further seeding the flow with light-reflecting flakes, the flow can be visualized. Snapshots were taken from the upper plate (see Fig. II.1(b)) and they show the formation of swirls and a chaotic behaviour reminiscent of turbulence. In this experiment the Reynolds number is

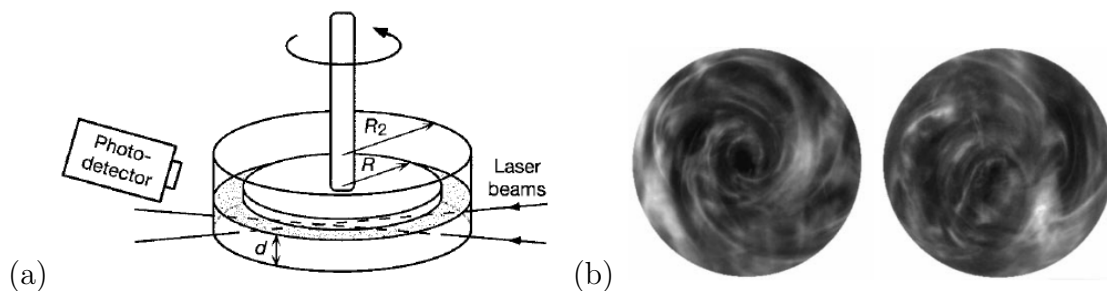


FIGURE II.1. The experimental set-up (a) and the resulting flow visualization (b) in the experiment of Groisman and Steinberg. Reprinted by permission from Macmillan Publishers Ltd: *Nature* **405**, 53, copyright (2000) (Ref. [36]).

$Re = 0.7$. Since Re is small, the turbulent-like behaviour is attributed to the elastic forces at play.

Indeed, one of the most remarkable properties of viscoelastic fluids such as polymer solutions is the formation of instabilities at very low Reynolds numbers [47, 68]. Such instabilities are of a purely elastic nature; they occur when inertial forces are negligible and elastic forces are strong. The relevant dimensionless number is the Weissenberg number Wi (the ratio of the polymer relaxation time and the typical time scale of the flow). As described above, elastic instabilities eventually lead to a chaotic regime known as elastic turbulence if Wi is sufficiently high [36].

Since the pioneering work by Groisman and Steinber [36], various microfluidic experiments have been performed to study elastic turbulence. It is easily observed in curved flow structures [17, 18, 37, 38, 63, 79] and is recently also observed in pipe flows [15] and channel flows [10, 58]. Other than in polymer solutions containing the usual high-molecular weight polymers (polyacrylamide, polyethylene oxide), the turbulentlike behaviour has also been observed in complex fluids, in particular, using wormlike micelles for the elastic particles. Micelles are likewise elastic but which break into smaller molecules and recombine into longer structures [4, 31].

Experimental studies reveal that the emergence of this regime is characterized by a fast growth of the Lyapunov exponent of the flow [16]. In addition, the kinetic-energy spatial and temporal spectra have a power-law behaviour, which indicates the presence of a large number of active scales in the flow. The spatial spectrum, k^{-a} with $a > 3$, is however steeper than for Newtonian turbulence, where the exponent is $-5/3$ in three dimensions, i.e. velocity fluctuations in elastic turbulence are concentrated at small wave numbers [19, 36]. This chaotic regime is associated to polymers stretching in the flow [18, 36]. Indeed, it is argued that the flow stretches and injects energy into the polymers, which then feedback to the flow until a stationary state is achieved.

The experimental findings are enriched further from the numerical and theoretical point of view. Striking similarities between the equations for viscoelastic polymer solutions and that for magnetohydrodynamics are identified in the literature [8, 32, 56]. Filaments dubbed as elastic waves were observed in the vorticity field in numerical simulations and bring to mind the Alfvén waves in magnetohydrodynamics [8]. Moreover, elastic turbulence can also be numerically reproduced in simulations using polymer solution models, for instance using the two-dimensional Oldroyd-B model with a Kolmogorov force [7, 8]. The Oldroyd-B model, which will be further described in the upcoming chapter, is one of the simplest constitutive models and is characterized by linear elasticity. The Kolmogorov flow is a parallel flow and produces a sinusoidal mean flow even in the presence of elastic polymers. The presence of a critical Reynolds number under which inertial forces are negligible in the Kolmogorov flow points to the role of elastic forces in creating the chaotic regime [12]. Other constitutive models have been used to simulate elastic turbulence, such as those with a nonlinear elastic force (see, e.g., [41]). Numerical and theoretical studies considering different flow configurations (e.g. plane Couette, Poiseuille or cellular flows) also display the presence of these elastic instabilities, [41, 50, 53]. Consistent with experimental results, numerical simulations indicate that the polymers stretch and exert stronger elastic forces on the flow if Wi is sufficiently high. Snapshots of the vorticity field (see Fig. II.2) and the observed increase in the Lyapunov exponents (see, e.g. Ref. [7]) also point to the presence of mixing.

Elastic turbulence has found important applications in microfluidics in view of the fact that it can create chaotic flows and strongly enhance mixing in devices that, owing to their microscopic size, are characterized by a low Reynolds number [1, 18, 45, 62, 75]. Indeed, viscoelastic solutions are considered as alternatives to the more traditional methods of passively inducing mixing by introducing curves and obstacles on the geometry of the flow, and of actively perturbing the flow, for instance, mechanically or by thermal or electrokinetic instabilities [57, 69, 70]. Since elastic turbulence is chaotic but remains spatially smooth, further insight into particle dynamics below the dissipation scale of hydrodynamic turbulence can be obtained from the elastic-turbulent regime generated in microfluidics experiments where observations are easier to perform [44]. Moreover, the potential use of elastic turbulence in the oil industry has recently emerged as a very promising application. Aqueous polymer solutions are indeed used to recover the oil that remains trapped inside the pores of reservoir rocks after an initial water flooding, and elastic turbulence has been proposed as a mechanism to explain the unexpectedly high efficiency of this oil recovery method [20, 51].

This second part of the thesis studies elastic turbulence in two different orientations.

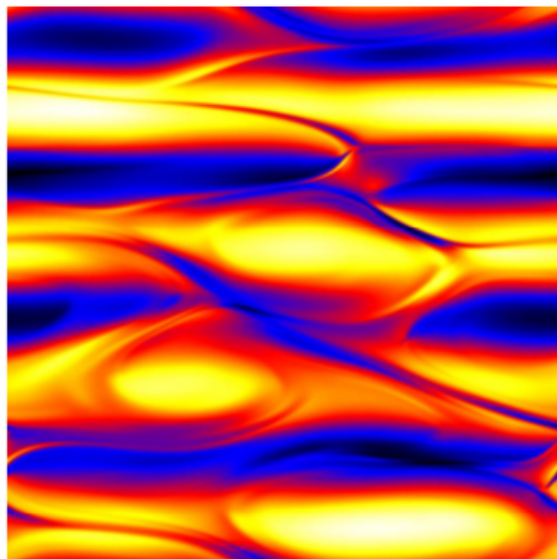


FIGURE II.2. Vorticity field in numerical simulations of the two-dimensional Oldroyd-B model at low $Re = 0.7$ and $Wi = 22.4$ and with a Kolmogorov forcing. Black (white) represents maximum (minimum) vorticity. From Ref. [8]. Reprinted figure with permission from Berti S, Boffetta G, *Phys. Rev. E* **82**, 036314 (2010). Copyright (2010) by the American Physical Society.

Chapter 4

This chapter poses the question of the quantitative characterization of this chaotic regime via its number of degrees of freedom. To this end, the Oldroyd-B model is used being the simplest constitutive model that reproduces elastic turbulence. The Lyapunov dimension of the attractor (in the solution space) of the Oldroyd-B model is estimated as a function of Wi by combining a mathematical analysis of the model with direct numerical simulations.

Chapter 5

This subpart of the thesis is motivated by experimental and numerical results of polymer solutions in the high- Re regime that show that elasticity of polymers is dispensable to produce drag reduction. The (un)necessity of elasticity so as to enhance mixing in the low- Re regime is examined by simulating a solution of rodlike polymers. The results show the emergence of a chaotic regime that manifests through an increase in the flow resistance and a power-law in the kinetic-energy spectrum. The significant polymer contribution to the total stress paired with a negligible Reynolds stress imply that the chaotic regime is not caused by inertial forces but rather by the presence of the rodlike polymers.

CHAPTER 4

Lyapunov dimension of elastic turbulence

4.1. Introduction

The simplest constitutive model of polymer solutions is the Oldroyd-B model [55], in which the dissolved polymer phase is described by a symmetric tensor field, termed the polymer conformation tensor, which represents the moment of inertia of polymers averaged over thermal fluctuations. The Oldroyd-B model is thus a system of partial differential equations (PDEs) that describes the joint evolution of the velocity and the polymer conformation tensor. In particular, the polymer feedback on the flow is given by a stress term proportional to the conformation tensor. The relevant dimensionless number is the Weissenberg number Wi , i.e. the ratio of the polymer relaxation time and the typical time scale of the flow. The main limitations of this model are that it assumes a single polymer relaxation time and linear elasticity. The latter, in extensional flows and in the absence of polymer feedback, can lead to an unbounded growth of the conformation tensor and hence of polymer stresses. In spite of its simplicity, the model successfully reproduces the main features of elastic turbulence, as just discussed in the introduction [7, 8, 32, 35]. In particular numerical simulations show that elastic turbulence is observed also in two-dimensional settings. Other than attracting the physicists for its dynamical interest and the industry for its possible applications, elastic turbulence has also attracted much attention in the mathematical community over the last two decades. Mathematicians have focused on the existence, uniqueness and regularity of solutions (see, e.g., Refs. [3, 24, 29, 43, 49] for some recent studies).

This chapter aims at providing an analytic and quantitative characterization of the chaotic regime due to elastic instabilities in two dimensions via the Oldroyd-B model. A mathematical definition of the number of degrees of freedom of PDEs is given by the dimension of its global attractor in the functional space of the solution, where the global attractor is defined as the set of solutions to which any solution converges to [66]. For the two-dimensional Oldroyd-B model the bounds found by Constantin and Kliegl [24] on the L^2 -norms of the vorticity ω and the polymer conformation tensor σ , $\|\omega\|_2$ and $\|\sigma\|_2$, are exponential in time (and double exponential for $\|\nabla\sigma\|_2$). Thus, no bounded long-time averages $\langle \cdot \rangle = \lim_{T \rightarrow \infty} \frac{1}{T} \int_0^T \cdot dt$ have been found to exist and therefore, in a strictly rigorous sense, no global attractor is known to exist. However, numerical simulations of elastic turbulence suggest that $\|\omega\|_2$, $\|\sigma\|_2$ and $\|\nabla\sigma\|_2$ are indeed bounded in time for various values of Wi (see Fig. 4.1 and Sec. 4.5). One practical way of progressing is to work under the following technical assumption with a subsequent strategy:

- i. Given that numerical calculations of $\|\omega\|_2$, $\|\sigma\|_2$ and $\|\nabla\sigma\|_2$ are finite in time, as shown in Sec. 4.5, the existence of a global attractor \mathcal{A} is assumed;

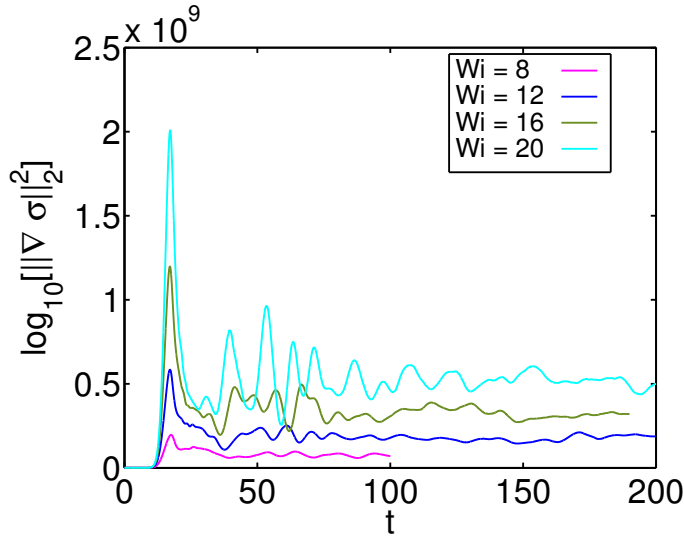


FIGURE 4.1. Time series for $\|\nabla\sigma\|_2^2$ for a simulation of the two-dimensional Oldroyd-B model with a cellular forcing $f = -f_0n[\cos(nx) + \cos(ny)]$ with $n = 4$ and $f_0 = 0.16$ for different values of Wi .

- ii. Based on (i), the Lyapunov dimension of \mathcal{A} is estimated. The estimate will use the long-time averages $\langle\|\omega\|_2\rangle$, $\langle\|\sigma\|_2\rangle$ and $\langle\|\nabla\sigma\|_2\rangle$; the numerical bounds found for these quantities in terms of Wi are used in the estimates.

An introduction to the method used to estimate the Lyapunov dimension is provided in Sec. 4.2. The equations of the Oldroyd-B model are given in Sec. 4.3, and the estimation, which involves a number of technical steps, follows in Sec. 4.4. The numerical simulations that complete the study and justify the assumed attractor is found in Sec. 4.5. Concluding remarks and perspectives follow thereafter.

4.2. Lyapunov exponents of dynamical systems

This section extends the methods to estimate the Lyapunov dimension of ordinary differential equations (ODEs) to PDEs. Indeed, a connection between the system dynamics and the attractor dimension is provided by the notion of the Lyapunov exponents via the Kaplan–Yorke formula. For ODEs, the Lyapunov exponents control the exponential growth or contraction of volume elements in phase space, and the Kaplan–Yorke formula expresses the balance between volume growth and contraction realized on the attractor. The Kaplan–Yorke formula, which originated as a phase-space argument for ODEs, has been nevertheless rigorously applied to global attractors in PDEs by Constantin and Foias [22] (see also Ref. [33]). It is important to note that the definition of the Lyapunov exponents, defined before in Chap. 2 as the exponential growth rate between two trajectories in the space, will be extended to a more general notion: it will define the exponential growth rate between trajectories *in the solution space of a PDE* (e.g. L^2 space). The next subsections will go through the Kaplan–Yorke formula and the extension to PDEs via the ‘trace formula’.

4.2.1. The Kaplan–Yorke formula. The Kaplan–Yorke formula is used to define the Lyapunov dimension of the attractor of a dynamical system and is the

following: for Lyapunov exponents $\mu_1 \geq \mu_2 \geq \dots \geq \mu_n \geq \dots$, the Lyapunov dimension $d_L(\mathcal{A})$ is given by

$$d_L(\mathcal{A}) = N - 1 + \frac{\mu_1 + \dots + \mu_{N-1}}{-\mu_N}, \quad (4.1)$$

where the number N of μ_n is chosen to satisfy

$$\sum_{n=1}^{N-1} \mu_n \geq 0 \quad \text{but} \quad \sum_{n=1}^N \mu_n < 0. \quad (4.2)$$

Note that according to the definition of N , the ratio of exponents in (4.1) satisfies

$$0 \leq \frac{\mu_1 + \dots + \mu_{N-1}}{-\mu_N} < 1. \quad (4.3)$$

In simple terms, the value of N that turns the sign of the sum of the Lyapunov exponents as in (4.2) is that value that bounds above $d_L(\mathcal{A})$ such that

$$N - 1 \leq d_L(\mathcal{A}) < N. \quad (4.4)$$

The preceding inequalities mean that there are $(N - 1)$ dimensional volumes in the phase-space that grow larger in time whereas any N -dimensional volume contracts over time.

4.2.2. The trace formula. In the PDE case the phase space is infinite-dimensional. To use the method for PDEs to find an estimate for $d_L(\mathcal{A})$, it is necessary to extend the idea of the Lyapunov exponents to *global* Lyapunov exponents via a trace formula, whose derivation is demonstrated here [26, 66].

The following derivation will seem to be performed for an ODE on \mathbf{q} (it is also valid for ODEs). For PDEs, however, \mathbf{q} is not in the real d -dimensional space (e.g. \mathbb{R}^d). Rather, \mathbf{q} lies in an infinite-dimensional space associated to the *solution space* of the PDE. By taking the Fourier transform of a PDE, \mathbf{q} can for instance be taken to account for the different wavenumbers characterizing the basis functions that define the solution. The following derivation then will be defined for an arbitrary large N -dimensional (truncated) system; the value of N can be increased until indefinitely. Indeed, the goal is to identify the value N that turns the sign of the PDE counterpart of $\sum_{n=1}^N \mu_n$ and thus gives inequality (4.4).

Consider an N -dimensional (truncated) system in the *solution space* of a PDE. Then \mathbf{q} evolves as

$$\frac{d\mathbf{q}}{dt} = \mathbf{G}(\mathbf{q}, t) \quad (4.5)$$

for some sufficiently smooth function \mathbf{G} associated to the PDE on the variable \mathbf{q} . Let $\mathbf{q}(0)$ be an initial point on the attractor \mathcal{A} . To quantify the growth of infinitesimal “volumes” in the solution space around the point $\mathbf{q}(0)$, consider an initial perturbation $\mathbf{q}(0) + \delta\mathbf{q}_i(0)$ for N orthogonal vectors $\delta\mathbf{q}_i, i = 1, \dots, N$ and see how the N -volume or parallelepiped of volume

$$V_N(t) = |\delta\mathbf{q}_1 \wedge \delta\mathbf{q}_2 \wedge \dots \wedge \delta\mathbf{q}_N| \quad (4.6)$$

evolves with the evolution of $\delta\mathbf{q}_i$ (see Fig. 4.2). This volume is given by

$$V_N(t)^2 = \det \mathbf{M}(t) \quad (4.7)$$

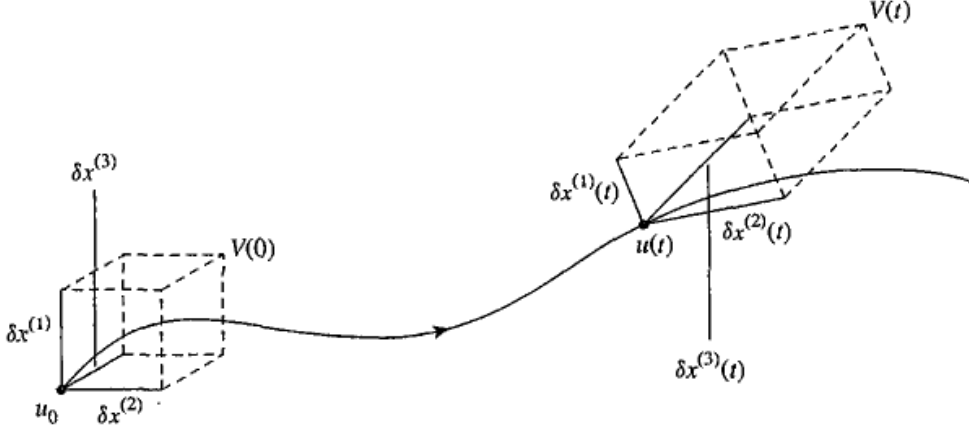


FIGURE 4.2. Illustration of the evolution of an initial N -parallelepiped ($N = 3$) over time. Note the difference of notation: $\delta \mathbf{q}$ in the text is equivalent to $\delta \mathbf{x}$ in the illustration. From Ref. [66].

where $M_{ij}(t) = \delta \mathbf{q}_i(t) \cdot \delta \mathbf{q}_j(t)$. Taking the logarithm of Eq. (4.7), differentiating over time and using the property that $\log \det \mathbf{M} = \text{Tr}[\log \mathbf{M}]$ yields

$$2 \frac{d \log V_N}{dt} = \frac{d}{dt} \log \det \mathbf{M} = \frac{d}{dt} \text{Tr}[\log \mathbf{M}] = \text{Tr} \left[\mathbf{M}^{-1} \frac{d\mathbf{M}}{dt} \right]. \quad (4.8)$$

The evaluation of the trace in the equation above requires a time-dependent orthogonal set of basis vectors $\{\phi_i\}$, $i = 1, \dots, N$ that also span the space spanned by $\{\delta \mathbf{q}_i\}$ and which permits the definition of a matrix \mathbf{m}

$$\mathbf{m}_{ij} = \phi_i \cdot \delta \mathbf{q}_j, \quad (4.9)$$

whose components are the projections of $\delta \mathbf{q}_j$ onto ϕ_i , and which satisfies the relations

$$\mathbf{M} = \mathbf{m}^\top \mathbf{m}. \quad (4.10)$$

Now under an assumption on the smoothness of \mathbf{G} in Eq. (4.5), the evolution of the $\delta \mathbf{q}_i(t)$ over time follows the linearised evolution

$$\frac{d}{dt} \delta \mathbf{q}_i = \mathbf{A} \delta \mathbf{q}_i \quad (4.11)$$

where \mathbf{A} is the linearised operator associated to \mathbf{G} . The evolution of the orthogonal basis $\{\phi_i\}$ can then be expressed in terms of

$$\mathbf{a}_{ij} = \phi_i \cdot \mathbf{A} \phi_j. \quad (4.12)$$

Taking the derivative of Eq. (4.10) and using Eqs. (4.11) and (4.12) yields

$$\begin{aligned} \frac{dM_{ij}}{dt} &= \frac{d\delta \mathbf{q}_i}{dt} \cdot \delta \mathbf{q}_j + \delta \mathbf{q}_i \cdot \frac{d\delta \mathbf{q}_j}{dt} \\ &= \mathbf{A} \delta \mathbf{q}_i \cdot \delta \mathbf{q}_j + \delta \mathbf{q}_i \cdot \mathbf{A} \delta \mathbf{q}_j \\ &= (\delta \mathbf{q}_i \cdot \phi_l) (\mathbf{A} \phi_l \cdot \phi_k) (\phi_k \cdot \delta \mathbf{q}_j) + (\delta \mathbf{q}_i \cdot \phi_l) (\phi_l \cdot \mathbf{A} \phi_k) (\phi_k \cdot \delta \mathbf{q}_j) \\ &= \mathbf{m}_{li} (\mathbf{a}_{kl} + \mathbf{a}_{lk}) \mathbf{m}_{kj}, \end{aligned}$$

whence,

$$\frac{d\mathbf{M}}{dt} = \mathbf{m}^\top (\mathbf{a}^\top + \mathbf{a}) \mathbf{m}, \quad (4.13)$$

where one of the steps used the fact that $\{\phi_i\}$ is an orthonormal basis. Hence, thanks to the expressions in Eqs. (4.10) and (4.13), Eq. (4.8) can be written as

$$\begin{aligned} \frac{d}{dt} \log V_N(t) &= \frac{1}{2} \text{Tr} \left[\mathbf{M}^{-1} \frac{d\mathbf{M}}{dt} \right] \\ &= \frac{1}{2} \text{Tr} [\mathbf{m}^{-1} (\mathbf{m}^\top)^{-1} \mathbf{m}^\top (\mathbf{a}^\top + \mathbf{a}) \mathbf{m}] \\ &= \frac{1}{2} \text{Tr} [\mathbf{m}^{-1} (\mathbf{a}^\top + \mathbf{a}) \mathbf{m}] \\ &= \text{Tr} [\mathbf{a}]. \end{aligned} \quad (4.14)$$

Then from Eq. (4.12)

$$\begin{aligned} \text{Tr}[\mathbf{a}] &= \phi_i \cdot \mathbf{A} \phi_i = (\phi_j \cdot \mathbf{A} \phi_i) (\phi_i \cdot \phi_j) \\ &= \text{Tr}[\mathbf{A} \mathbf{P}_N], \end{aligned} \quad (4.15)$$

where $\mathbf{P}_N(\mathbf{u}) = \phi_i (\phi_i \cdot \mathbf{u})$ is the operator that projects a vector \mathbf{u} onto $\{\phi_i\}$. Integrating for the volume from Eq. (4.14) up to a time t and by using the preceding equation gives

$$\begin{aligned} V_N(t) &= V_N(0) \exp \left[\int_0^t \text{Tr}[\mathbf{A}(\tau) \mathbf{P}_N(\tau)] d\tau \right] \\ &= V_N(0) \exp \left[t \left(\frac{1}{t} \int_0^t \text{Tr}[\mathbf{A}(\tau) \mathbf{P}_N(\tau)] d\tau \right) \right] \\ &= V_N(0) \exp [t \langle \text{Tr}[\mathbf{A} \mathbf{P}_N] \rangle], \end{aligned} \quad (4.16)$$

where $\langle \cdot \rangle = \lim_{T \rightarrow \infty} \frac{1}{T} \int_0^T \cdot dt$ is the time average. The sum of the first N Lyapunov exponents, which characterize the exponential growth rate of an N -volume, is then taken to be the

$$\sum_{n=1}^N \mu_n = \langle \text{Tr}[\mathbf{A} \mathbf{P}_N] \rangle. \quad (4.17)$$

Clearly if the time average of the trace is negative, the volume decays to zero and the definition in (4.17) would be consistent with the definition of the Lyapunov exponents as in the subsection 4.2.1.

It is useful to remark that the trace formula (4.17) had already been utilised to obtain the attractor dimension for the 2D Navier–Stokes equation in terms of the Grashof number. Given an incompressible velocity field \mathbf{u} defined on a periodic domain $[0, L]^2$, the 2D Navier–Stokes equation is

$$\partial_t \mathbf{u} + \mathbf{u} \cdot \nabla \mathbf{u} = -\nabla p + \nu \Delta \mathbf{u} + \mathbf{F}, \quad (4.18)$$

where p is pressure, ν is kinematic viscosity, \mathbf{F} is a (divergence-free) body force. The Lyapunov dimension of its global attractor \mathcal{A} is estimated as [23, 25]:

$$d_L(\mathcal{A}) \leq c \mathcal{G}^{2/3} (1 + \ln \mathcal{G})^{1/3}, \quad (4.19)$$

where $\mathcal{G} = L^2 \|\mathbf{F}\|_2 / \nu^2$ is the Grashof number and c is a generic constant.

The Lyapunov dimension further gives an insight into the resolution length required to fully capture the dynamics of the system. For a d -dimensional system of size L , the resolution length ℓ_{res} of the smallest feature in the dynamics is connected to $d_L(\mathcal{A})$ by $d_L(\mathcal{A}) \sim (L/\ell_{\text{res}})^d$ [67]. Indeed, the formalism for calculating the Lyapunov dimension was developed to obtain a mathematically rigorous estimate of

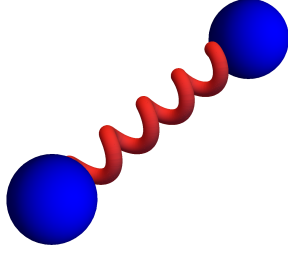


FIGURE 4.3. Illustration of a single extensible dumbbell.

the number of degrees of freedom of a system with the goal of verifying the available estimates based on dimensional or empirical arguments. In the case of the 2D Navier–Stokes equation, the associated resolution scale obtained from the Lyapunov dimension corresponds to the Kraichnan length [26]

$$\lambda_{Kr} = \left(\frac{\nu^3}{\chi} \right)^{1/6}, \quad (4.20)$$

which is the unique length scale that can be derived by using dimensional analysis based on the viscosity ν and then average enstrophy dissipation rate $\chi = \nu \langle \|\nabla \omega\|_2^2 \rangle / L^2$. Indeed, in 2D turbulence, enstrophy plays the role that energy takes in 3D turbulence and by analogy, it is λ_{Kr} that determines the cut-off value in the enstrophy spectrum. The estimate of the Lyapunov dimension thus supports the existing dimensional estimates for the theory of turbulence. This chapter extends the use of these formulas to estimate the Lyapunov dimension in a more complex setting by coupling two PDEs: one for the velocity field and another for the polymer conformation tensor.

4.3. The 2D Oldroyd-B model for polymer solutions

The method to estimate the Lyapunov dimension discussed above can be applied to any dynamical system. The choice for the two-dimensional Oldroyd-B model lies in the fact that it is one of the simplest constitutive models of polymer solutions that can reproduce elastic turbulence in numerical simulations. In the Oldroyd-B model, a polymer is described by a dumbbell whose end-to-end vector \mathbf{R} captures its length and orientation in space (see Fig. 4.3). Under the effect of an incompressible linear velocity field \mathbf{u} , the evolution of \mathbf{R} obeys the equation

$$\frac{d}{dt} R_i = R_k \partial_k u_i - \frac{f(\mathbf{R}^2)}{2\tau} R_i + \sqrt{\frac{R_0^2}{\tau}} \xi_i(t), \quad (4.21)$$

where R_0 is the equilibrium length of the polymer, $f(\mathbf{R}^2)$ is a force, τ is the polymer relaxation time and $\boldsymbol{\xi}(t)$ is white noise. In particular, the choice of $f(\mathbf{R}^2) = 1$ will, in the continuum, give rise to the Oldroyd-B model. An ensemble of these particles can be represented by the symmetric polymer conformation tensor $\sigma_{ij} = \langle R_i R_j \rangle_{\xi} / R_0^2$, where $\langle \cdot \rangle_{\xi}$ is an average over thermal noise. The evolution of $\boldsymbol{\sigma}$ follows by first using

the rules of stochastic calculus for Itô differential integrals

$$\frac{d}{dt}(R_i R_j) = (\nabla u)_{ik} R_k R_j + (\nabla u)_{jk} R_k R_i - \frac{R_0^2}{\tau} \left(\frac{R_i R_j}{R_0^2} - \delta_{ij} \right) + \sqrt{\frac{R_0^2}{\tau}} (\xi_i R_j + \xi_j R_i), \quad (4.22)$$

where $(\nabla u)_{ij} = \partial_j u_i$. Taking the average over noise eliminates the last term. The polymer feedback to the flow is modeled by an additional stress term in the Navier–Stokes equation. On the periodic unit square $\Omega = [0, 1]^2$, the dimensionless form of the Oldroyd-B model is then given by

$$\partial_t \mathbf{u} + \mathbf{u} \cdot \nabla \mathbf{u} = -\nabla p + \frac{1}{Re} \Delta \mathbf{u} + \frac{\beta}{Wi Re} \nabla \cdot \boldsymbol{\sigma} + \mathbf{F}, \quad (4.23a)$$

$$\partial_t \boldsymbol{\sigma} + \mathbf{u} \cdot \nabla \boldsymbol{\sigma} = (\nabla \mathbf{u}) \boldsymbol{\sigma} + \boldsymbol{\sigma} (\nabla \mathbf{u})^\top - \frac{1}{Wi} (\boldsymbol{\sigma} - \mathbf{l}) + \frac{1}{Pe} \Delta \boldsymbol{\sigma}, \quad (4.23b)$$

where p is pressure and where $Re = UL/\nu$, $Pe = UL/\kappa$ and $Wi = U\tau/L$ are the Reynolds, Péclet and Weissenberg numbers respectively with L and U as the characteristic lengths and velocities of the flow and κ as the diffusion coefficient of the centre of mass of the polymers. Indeed the Laplacian term in Eq. (4.23b) originates from the diffusion of the centre of mass of polymers [30]; it ensures the global regularity of the two-dimensional Oldroyd-B model [24] and improves the stability of numerical simulations, even though the values of Pe used in practice are considerably lower than its realistic values [71, 74]. The first two (Re , Pe) of these dimensionless numbers describe the ratio of the inertial forces to the viscous forces and to the rate of diffusion of the centre of mass, respectively, while the last dimensionless number (Wi) compares the time scale of the flow to the relaxation time of the polymer. The positive constant β is proportional to the polymer concentration and equilibrium extension. The forcing \mathbf{F} is time-independent, periodic and divergence-free ($\nabla \cdot \mathbf{F} = 0$).

In two dimensions, Eqs. (4.23) can be rewritten in terms of the scalar vorticity $\omega = \hat{\mathbf{z}} \cdot (\nabla \times \mathbf{u})$:

$$\partial_t \omega + \mathbf{u} \cdot \nabla \omega = \frac{1}{Re} \Delta \omega + \frac{\beta}{Wi Re} \hat{\mathbf{z}} \cdot \nabla \times (\nabla \cdot \boldsymbol{\sigma}) + f, \quad (4.24a)$$

$$\partial_t \boldsymbol{\sigma} + \mathbf{u} \cdot \nabla \boldsymbol{\sigma} = (\nabla \mathbf{u}) \boldsymbol{\sigma} + \boldsymbol{\sigma} (\nabla \mathbf{u})^\top - \frac{1}{Wi} (\boldsymbol{\sigma} - \mathbf{l}) + \frac{1}{Pe} \Delta \boldsymbol{\sigma}, \quad (4.24b)$$

where $f = \hat{\mathbf{z}} \cdot (\nabla \times \mathbf{F})$ and $\mathbf{u} = \nabla^\perp \Delta^{-1} \omega$ with $\nabla^\perp \equiv (-\partial_y, \partial_x)$. Since \mathbf{F} is periodic, the spatial average of ω is zero, and the inverse Laplacian of ω is properly defined. Figure 4.4 shows snapshots of the ω and $\text{Tr } \boldsymbol{\sigma}$ fields from a numerical simulation of Eqs. (4.24) in the elastic-turbulence regime using a cellular forcing $f = -f_0 n [\cos(nx) + \cos(ny)]$ with $n = 4$ and $f_0 = 0.16$. Note that $\text{Tr } \boldsymbol{\sigma}$ is concentrated over very thin regions, which is associated with large gradients in the polymer-conformation-tensor field.

4.4. Estimating the Lyapunov dimension

It is possible to estimate the Lyapunov dimension of the Oldroyd-B model in Eqs. (4.24) via the trace formula discussed in Sec. 4.2.2, which estimates the growth rate of N -dimensional volumes in the space of the solutions $(\omega, \boldsymbol{\sigma})$. To use the trace formula in Eq. (4.17) requires the methods of Refs. [22],[23],[25] and, in particular,

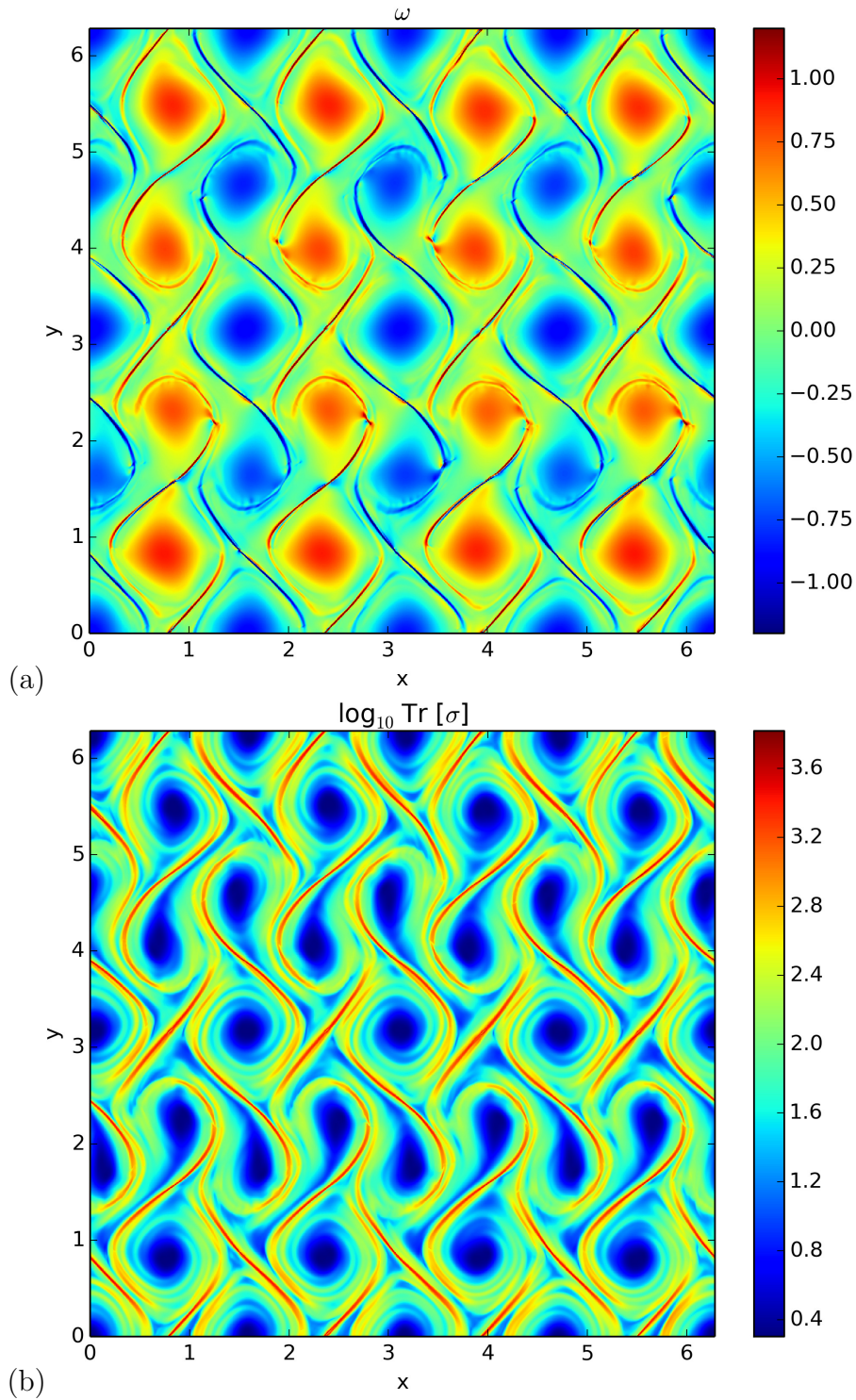


FIGURE 4.4. Pseudocolor plot of: (a) ω and (b) $\log_{10} \text{Tr} \sigma$ for $Re = Re_c/\sqrt{2}$, $Wi = 20$, $\beta = 0.2$; and a cellular forcing with $n = 4$ and $f_0 = 0.16$ (see Sec. 4.5 for the details).

the L^∞ -estimates of Ref. [21]. These references will be cited during the crucial steps of the calculation.

Denote by $\mathbf{q} = (\omega, \boldsymbol{\sigma})$ a solution of system (4.24) and denote by $\delta\mathbf{q} = (\delta\omega, \delta\boldsymbol{\sigma})$ the infinitesimal displacement about \mathbf{q} in the solution space. As in Eq. (4.11) the displacements $\delta\mathbf{q}$ satisfy the linearized set of equations from Eqs. (4.24):

$$\frac{d}{dt}\delta\mathbf{q} = \mathbf{A}(t)\delta\mathbf{q} = \begin{pmatrix} -\mathbf{u} \cdot \nabla \delta\omega + \frac{1}{Re} \Delta \delta\omega - \delta\mathbf{u} \cdot \nabla \omega + \frac{\beta}{Wi Re} \hat{\mathbf{z}} \cdot \nabla \times (\nabla \cdot \delta\boldsymbol{\sigma}) \\ (\nabla \delta\mathbf{u})\boldsymbol{\sigma} + \boldsymbol{\sigma}(\nabla \delta\mathbf{u})^\top - \delta\mathbf{u} \cdot \nabla \boldsymbol{\sigma} - \mathbf{u} \cdot \nabla \delta\boldsymbol{\sigma} + \dots \\ + (\nabla \mathbf{u})\delta\boldsymbol{\sigma} + \delta\boldsymbol{\sigma}(\nabla \mathbf{u})^\top - \frac{\delta\boldsymbol{\sigma}}{Wi} + \frac{1}{Pe} \Delta \delta\boldsymbol{\sigma} \end{pmatrix}, \quad (4.25)$$

where the explicit form of the operator $\mathbf{A}(t)$ can be obtained by using $\mathbf{u} = \nabla^\perp \Delta^{-1} \omega$ to express \mathbf{u} and $\delta\mathbf{u}$ in terms of ω and $\delta\omega$, respectively. Following the discussion in Sec. 4.2, take different sets of initial conditions $\mathbf{q}(0) + \delta\mathbf{q}_i(0)$ which evolve into $\mathbf{q}(t) + \delta\mathbf{q}_i(t)$ for $i = 1, \dots, N$. If they are chosen to be linearly independent, these $\delta\mathbf{q}_i$ form an N -dimensional parallelepiped of volume $V_N(t)$ which changes over time as (see Eq. 4.16)

$$V_N(t) = V_N(0) \exp \{t \langle \text{Tr} [\mathbf{A}\mathbf{P}_N] \rangle\}, \quad (4.26)$$

where, as before, $\langle \cdot \rangle$ is the time average and \mathbf{P}_N is the L^2 -orthogonal projection onto the finite dimensional subspace span $\{\delta\mathbf{q}_1, \delta\mathbf{q}_2, \dots, \delta\mathbf{q}_N\}$.

To estimate the Lyapunov dimension requires finding the value of N that turns the sign of $\langle \text{Tr} [\mathbf{A}\mathbf{P}_N] \rangle$. This value of N bounds above $d_L(\mathcal{A})$ as in inequality (4.4). In elastic turbulence it is assumed that $Pe \gg 1$, $Wi \gg 1$ and $0 < Re < Re_c$, where Re_c is the critical value for the appearance of inertial instabilities in a flow. The whole calculation is divided into three parts simply to allow the reader to pause after a series of technical steps; some inequalities that will be used in the derivation are provided in the appendix. The technical details may be skipped and the reader is redirected to Eqs. (4.46a) and (4.46b) (Sec. 4.4.3), which give the sufficient conditions for N so that the time average in Eq. (4.26) is negative.

4.4.1. Estimating the trace: Part I. The trace $\text{Tr} [\mathbf{A}\mathbf{P}_N]$ can be expressed as (e.g. Refs. [22, 26, 66])

$$\text{Tr} [\mathbf{A}\mathbf{P}_N] = \sum_{n=1}^N \int_{\Omega} \boldsymbol{\Phi}_n \cdot \mathbf{A}\boldsymbol{\Phi}_n \, d\mathbf{x}, \quad (4.27)$$

where $\{\boldsymbol{\Phi}_n\}_{n=1}^N = \{(\phi_n^\omega, \phi_n^\sigma)\}_{n=1}^N$ with $(\phi_n^\sigma)^\top = \phi_n^\sigma$ is an orthonormal set spanning the subspace generated by the displacements $\{(\delta\omega_n, \delta\boldsymbol{\sigma}_n)\}_{n=1}^N$. The orthonormality of $\{\boldsymbol{\Phi}_n\}_{n=1}^N$ should be interpreted as follows:

$$\int_{\Omega} \phi_m^\omega \phi_n^\omega \, d\mathbf{x} + \int_{\Omega} \phi_m^\sigma : \phi_n^\sigma \, d\mathbf{x} = \delta_{mn}, \quad (4.28)$$

whence

$$\sum_{n=1}^N \int_{\Omega} |\boldsymbol{\Phi}_n|^2 \, d\mathbf{x} = \sum_{n=1}^N \int_{\Omega} (|\phi_n^\omega|^2 + |\phi_n^\sigma|^2) \, d\mathbf{x} = N. \quad (4.29)$$

The symbol ‘ \cdot ’ denotes the inner product between matrices, $\boldsymbol{\sigma} : \boldsymbol{\sigma}' \equiv \text{Tr}[\boldsymbol{\sigma}^\top \boldsymbol{\sigma}']$ and where $|\phi_n^\sigma|^2 = \phi_n^\sigma : \phi_n^\sigma = \sum_{i,j} |(\phi_n^\sigma)_{ij}|^2$. The following inequality (e.g. Ref. [66], see

also inequality (4.52) in Appendix 4.7.1) will also be used when the norms of $\phi_n^\omega, \phi_n^\sigma$ or of their gradients are estimated:

$$\Theta \equiv \text{Tr} [-\Delta \mathbf{P}_N] = - \sum_{n=1}^N \int_{\Omega} \left(\phi_n^\omega \Delta \phi_n^\omega + \phi_n^\sigma : \Delta \phi_n^\sigma \right) d\mathbf{x} \geq cN^2, \quad (4.30)$$

where c is henceforth regarded as a generic, positive, dimensionless constant. The terms appearing in Eq. (4.27) can be explicitly listed as (the terms that follow from $\mathbf{u} \cdot \nabla \delta \omega$ and $\mathbf{u} \cdot \nabla \delta \sigma$ vanish because of the incompressibility of \mathbf{u})

$$\text{Tr} [\mathbf{A} \mathbf{P}_N] = \frac{1}{Re} \sum_{n=1}^N \int_{\Omega} \phi_n^\omega \Delta \phi_n^\omega d\mathbf{x} + \frac{1}{Pe} \sum_{n=1}^N \int_{\Omega} \phi_n^\sigma : \Delta \phi_n^\sigma d\mathbf{x} \quad (4.31a)$$

$$- \sum_{n=1}^N \int_{\Omega} \phi_n^\omega \mathbf{v}_n \cdot \nabla \omega d\mathbf{x} - \sum_{n=1}^N \int_{\Omega} \phi_n^\sigma : (\mathbf{v}_n \cdot \nabla \sigma) d\mathbf{x} \quad (4.31b)$$

$$+ \frac{\beta}{Wi Re} \sum_{n=1}^N \int_{\Omega} \phi_n^\omega \hat{\mathbf{z}} \cdot (\nabla \times \nabla \cdot \phi_n^\sigma) d\mathbf{x} - \frac{1}{Wi} \sum_{n=1}^N \int_{\Omega} |\phi_n^\sigma|^2 d\mathbf{x} \quad (4.31c)$$

$$+ \sum_{n=1}^N \int_{\Omega} \phi_n^\sigma : [(\nabla \mathbf{v}_n) \sigma + \sigma (\nabla \mathbf{v}_n)^\top] d\mathbf{x} \quad (4.31d)$$

$$+ \sum_{n=1}^N \int_{\Omega} \phi_n^\sigma : [(\nabla \mathbf{u}) \phi_n^\sigma + \phi_n^\sigma (\nabla \mathbf{u})^\top] d\mathbf{x}, \quad (4.31e)$$

where $\mathbf{v}_n = \nabla^\perp \Delta^{-1} \phi_n^\omega$. By using (4.30), the Laplacian terms in (4.31a) can be shown to satisfy (under the assumption $Pe > Re$)

$$\frac{1}{Re} \sum_{n=1}^N \int_{\Omega} \phi_n^\omega \Delta \phi_n^\omega d\mathbf{x} + \frac{1}{Pe} \sum_{n=1}^N \int_{\Omega} \phi_n^\sigma : \Delta \phi_n^\sigma d\mathbf{x} \leq -\frac{1}{Re} \Theta. \quad (4.32)$$

The advective terms (4.31b) are treated by using the result of Ref. [21] and its subsequent use in Ref. [25]: i.e. a Cauchy–Schwarz inequality, an L^∞ bound for the terms involving \mathbf{v}_n (see inequality (4.53) in the appendix or Refs. [21, 25]), and inequality (4.30)

$$\left| \sum_{n=1}^N \int_{\Omega} \left[\phi_n^\omega \mathbf{v}_n \cdot \nabla \omega + \phi_n^\sigma : (\mathbf{v}_n \cdot \nabla \sigma) \right] d\mathbf{x} \right| \leq c(1 + \ln \Theta)^{1/2} \Theta^{1/4} (\|\nabla \omega\|_2 + \|\nabla \sigma\|_2), \quad (4.33)$$

where $\|\cdot\|_2^2 = \int_{\Omega} |\cdot|^2 d\mathbf{x}$ and $|\nabla \sigma|^2 = \sum_{i,j,k} |\partial_k \sigma_{ij}|^2$.

To estimate the feedback term in (4.31c), integration by parts, the Cauchy–Schwarz inequality, the relations $|\nabla \times (\phi_n^\omega \hat{\mathbf{z}})| = |\nabla \phi_n^\omega|$ and $|\nabla \cdot \phi_n^\sigma|^2 \leq |\nabla \phi_n^\sigma|^2$, and inequality (4.30) are used:

$$\left| \sum_{n=1}^N \int_{\Omega} \phi_n^\omega \hat{\mathbf{z}} \cdot (\nabla \times \nabla \cdot \phi_n^\sigma) d\mathbf{x} \right| \leq \sum_{n=1}^N \int_{\Omega} |\nabla \phi_n^\omega| |\nabla \phi_n^\sigma| d\mathbf{x} \leq \Theta. \quad (4.34)$$

The second term in (4.31c) satisfies

$$\frac{1}{Wi} \sum_{n=1}^N \int_{\Omega} |\phi_n^\sigma|^2 d\mathbf{x} = \frac{b}{Wi}, \quad 0 < b < N \leq c\Theta^{1/2}. \quad (4.35)$$

The stretching term that involves $\nabla \mathbf{v}_n$ in (4.31d) is first integrated by parts. The Cauchy-Schwarz inequality is then applied twice to obtain

$$\left| \sum_{n=1}^N \int_{\Omega} \phi_n^{\sigma} : [(\nabla \mathbf{v}_n) \boldsymbol{\sigma} + \boldsymbol{\sigma} (\nabla \mathbf{v}_n)^{\top}] \, d\mathbf{x} \right| \leq 2 \sum_{n=1}^N \int_{\Omega} (|\phi_n^{\sigma}| |\nabla \boldsymbol{\sigma}| |\mathbf{v}_n| + |\nabla \phi_n^{\sigma}| |\boldsymbol{\sigma}| |\mathbf{v}_n|) \, d\mathbf{x}.$$

The same techniques employed to get inequality (4.33) are used to obtain:

$$\left| \sum_{n=1}^N \int_{\Omega} \phi_n^{\sigma} : [(\nabla \mathbf{v}_n) \boldsymbol{\sigma} + \boldsymbol{\sigma} (\nabla \mathbf{v}_n)^{\top}] \, d\mathbf{x} \right| \leq c(1 + \ln \Theta)^{1/2} (\Theta^{1/2} \|\boldsymbol{\sigma}\|_2 + \Theta^{1/4} \|\nabla \boldsymbol{\sigma}\|_2). \quad (4.36)$$

The other stretching term (4.31e) is estimated by first applying the Cauchy–Schwarz inequality and inequality (4.30):

$$\left| \sum_{n=1}^N \int_{\Omega} \phi_n^{\sigma} : [(\nabla \mathbf{u}) \phi_n^{\sigma} + \phi_n^{\sigma} (\nabla \mathbf{u})^{\top}] \, d\mathbf{x} \right| \leq 2 \|\nabla \mathbf{u}\|_2 \left| \int_{\Omega} \left(\sum_{n=1}^N |\Phi_n|^2 \right)^2 \, d\mathbf{x} \right|^{1/2}.$$

Then note that in two dimensions $\|\nabla \mathbf{u}\|_2 = \|\omega\|_2$ and use the Lieb–Thirring inequality for the set of orthonormal functions $\{\Phi_n\}_{n=1}^N$ (see inequality (4.51) in appendix 4.7.1 or Ref.[23])

$$\left| \sum_{n=1}^N \int_{\Omega} \phi_n^{\sigma} : [(\nabla \mathbf{u}) \phi_n^{\sigma} + \phi_n^{\sigma} (\nabla \mathbf{u})^{\top}] \, d\mathbf{x} \right| \leq c \|\omega\|_2 \Theta^{1/2}. \quad (4.37)$$

Using (4.32)–(4.37), the trace $\text{Tr} [\mathbf{A}\mathbf{P}_N]$ can now be estimated in terms of Θ as follows

$$\begin{aligned} \text{Tr} [\mathbf{A}\mathbf{P}_N] &\leq \left(\frac{\beta}{Wi} - 1 \right) \frac{1}{Re} \Theta - \frac{b}{Wi} + c(1 + \ln \Theta)^{1/2} \Theta^{1/2} \|\boldsymbol{\sigma}\|_2 \\ &\quad + c(1 + \ln \Theta)^{1/2} \Theta^{1/4} (\|\nabla \boldsymbol{\sigma}\|_2 + \|\nabla \omega\|_2) + c \|\omega\|_2 \Theta^{1/2}. \end{aligned} \quad (4.38)$$

4.4.2. Estimating the trace: Part II. After estimating each of the terms in (4.31), the goal is now to express the time average of the trace in terms of $\langle \Theta \rangle$, which from (4.30) will provide an estimate for the value of N that makes the $\langle \text{Tr} [\mathbf{A}\mathbf{P}_N] \rangle < 0$.

In the third term in the right-hand side of inequality (4.38), it is useful to write $\Theta^{1/2} = \Theta^a \Theta^{1/2-a}$ with $0 < a < 1/2$. Taking the time average of inequality (4.38) and applying the Cauchy–Schwarz and Hölder’s inequalities on the time variable yields

$$\begin{aligned} \langle \text{Tr} [\mathbf{A}\mathbf{P}_N] \rangle &\leq \left(\frac{\beta}{Wi} - 1 \right) \frac{1}{Re} \langle \Theta \rangle - \frac{b}{Wi} + c \langle \|\omega\|_2^2 \rangle^{1/2} \langle \Theta \rangle^{1/2} \\ &\quad + c \langle (1 + \ln \Theta)^{3/2} \Theta^{3a} \rangle^{1/3} \langle \Theta^{3(1/2-a)} \rangle^{1/3} \langle \|\boldsymbol{\sigma}\|_2^3 \rangle^{1/3} \\ &\quad + c \langle (1 + \ln \Theta) \Theta^{1/2} \rangle^{1/2} (\langle \|\nabla \boldsymbol{\sigma}\|_2^2 \rangle^{1/2} + \langle \|\nabla \omega\|_2^2 \rangle^{1/2}). \end{aligned} \quad (4.39)$$

The bound in (4.39) can be further improved by estimating $\langle \|\nabla \omega\|_2^2 \rangle$. First multiply Eq. (4.24a) by ω , integrate over space, and take the time average (noting that is necessary to use the assumption that $\|\omega\|_2$ is finite and hence $\langle \partial_t \|\omega\|_2^2 \rangle = 0$):

$$\frac{1}{Re} \langle \|\nabla \omega\|_2^2 \rangle = \left\langle \int_{\Omega} \omega \hat{\mathbf{z}} \cdot \nabla \times \mathbf{F} \, d\mathbf{x} \right\rangle + \frac{\beta}{Wi Re} \left\langle \int_{\Omega} \omega \hat{\mathbf{z}} \cdot \nabla \times (\nabla \cdot \boldsymbol{\sigma}) \, d\mathbf{x} \right\rangle. \quad (4.40)$$

Then integrate by parts and apply the Cauchy–Schwarz inequality, first in space and then in time, to obtain

$$\langle \|\nabla\omega\|_2^2 \rangle^{1/2} \leq Re\|\mathbf{F}\|_2 + \frac{\beta}{Wi} \langle \|\nabla\sigma\|_2^2 \rangle^{1/2}. \quad (4.41)$$

Moreover, Jensen’s inequality for concave functions (see inequality (4.54) in appendix 4.7.1) allows us to express (4.39) as a function of $\langle\Theta\rangle$:

$$\begin{aligned} \langle \text{Tr}[\mathbf{A}\mathbf{P}_N] \rangle &\leq \left(\frac{\beta}{Wi} - 1 \right) \frac{1}{Re} \langle\Theta\rangle - \frac{b}{Wi} + c \langle \|\omega\|_2^2 \rangle^{1/2} \langle\Theta\rangle^{1/2} \\ &\quad + c(1 + \ln\langle\Theta\rangle)^{1/2} \langle\Theta\rangle^{1/2} \langle \|\sigma\|_2^3 \rangle^{1/3} + cRe(1 + \ln\langle\Theta\rangle)^{1/2} \langle\Theta\rangle^{1/4} \|\mathbf{F}\|_2 \\ &\quad + c(1 + \beta Wi^{-1})(1 + \ln\langle\Theta\rangle)^{1/2} \langle\Theta\rangle^{1/4} \langle \|\nabla\sigma\|_2^2 \rangle^{1/2}. \end{aligned} \quad (4.42)$$

Note that for this last inequality to hold, a must be such that $\Theta^{3(1/2-a)}$ and $(1 + \ln\Theta)^{3/2}\Theta^{3a}$ are concave functions. The choice $a = 1/5$ guarantees that $\Theta^{3(1/2-a)}$ is concave for all values of Θ and $(1 + \ln\Theta)^{3/2}\Theta^{3a}$ is concave for $\Theta > 5$. This restriction on Θ is justified since $\Theta \geq cN^2$ and in elastic turbulence N is large. The trace $\langle \text{Tr}[\mathbf{A}\mathbf{P}_N] \rangle$ is thus guaranteed to be negative if, by using Jensen’s inequality and inequality (4.41), $\langle\Theta\rangle$ satisfies

$$\begin{aligned} \left(1 - \frac{\beta}{Wi} \right) \langle\Theta\rangle &\geq cRe \langle \|\omega\|_2^2 \rangle^{1/2} \langle\Theta\rangle^{1/2} + cRe^2(1 + \ln\langle\Theta\rangle)^{1/2} \langle\Theta\rangle^{1/4} \|\mathbf{F}\|_2 \\ &\quad + cRe(1 + \ln\langle\Theta\rangle)^{1/2} \left\{ \langle\Theta\rangle^{1/2} \langle \|\sigma\|_2^3 \rangle^{1/3} \right. \\ &\quad \left. + \left(1 + \beta \frac{1}{Wi} \right) \langle\Theta\rangle^{1/4} \langle \|\nabla\sigma\|_2^2 \rangle^{1/2} \right\}. \end{aligned} \quad (4.43)$$

4.4.3. Estimating the trace: Part III. The inequality (4.43) that must be satisfied holds if $(1 - \beta Wi^{-1})\langle\Theta\rangle \approx \langle\Theta\rangle$ is greater than each of the terms in the right hand side. While it may look daunting to handle five inequalities, many of the terms will not contribute significantly in the elastic-turbulence regime. Under the assumptions that $0 < Re < Re_c$ and $Wi \gg 1$, it is easy to see that $(1 - \beta Wi^{-1})\langle\Theta\rangle \approx \langle\Theta\rangle$ is greater than each of the terms in the first line of (4.43). As $\|\mathbf{F}\|_2$ is independent of Wi , $\langle\Theta\rangle$ dominates the forcing term. In the elastic-turbulence regime of the Oldroyd-B model, the kinetic-energy spectrum decays rapidly as a function of the wave number [7, 8], and $\|\omega\|_2$ is expected to be small as Wi increases. Therefore, $\langle\Theta\rangle$ also controls the enstrophy term in (4.43)—this is confirmed numerically in Fig. 4.6.

The number of significant terms in (4.43) is thus reduced to two. Direct numerical simulations of the Oldroyd-B model show that in elastic turbulence $\text{Tr}\sigma$ grows as Wi increases and σ develops strong gradients [7, 8]. Therefore, both $\|\sigma\|_2$ and $\|\nabla\sigma\|_2$ are expected to increase with Wi . To analyze the σ - and $\nabla\sigma$ -terms in (4.43), it is useful to note that for any \mathcal{M} independent of $\langle\Theta\rangle^{1/2}$ and any $0 < \lambda < 3/2$ the following holds

$$\langle\Theta\rangle^{1/2} \geq c\mathcal{M}^{1/(2-\lambda)}(1 + \ln\mathcal{M})^{1/2(2-\lambda)} \implies \langle\Theta\rangle \geq c\mathcal{M}\langle\Theta\rangle^{\lambda/2}(1 + \ln\langle\Theta\rangle)^{1/2}. \quad (4.44)$$

The proof is given in appendix 4.7.2. Here, this implication was used for $\lambda = 1$ for the σ - term and $\lambda = 1/2$ for the $\nabla\sigma$ - term. The inequalities below are thus sufficient conditions for (4.43) to hold:

$$\langle\Theta\rangle^{1/2} > cRe \langle \|\sigma\|_2^3 \rangle^{1/3} (1 + \ln Re + \ln \langle \|\sigma\|_2^3 \rangle^{1/3})^{1/2}, \quad (4.45a)$$

$$\langle \Theta \rangle^{1/2} > cRe^{2/3} \langle \|\nabla \boldsymbol{\sigma}\|_2^2 \rangle^{1/3} (1 + \ln Re + \ln \langle \|\nabla \boldsymbol{\sigma}\|_2^2 \rangle^{1/2})^{1/3}, \quad (4.45b)$$

Since $\Theta \geq cN^2$ (see inequality (4.30)), these can be converted into sufficient conditions on N for the growth rate $\langle \text{Tr}[\mathbf{A}\mathbf{P}_N] \rangle$ to be negative and the N -volume V_N to contract:

$$N > cRe \langle \|\boldsymbol{\sigma}\|_2^3 \rangle^{1/3} (1 + \ln Re + \ln \langle \|\boldsymbol{\sigma}\|_2^3 \rangle^{1/3})^{1/2}, \quad (4.46a)$$

$$N > cRe^{2/3} \langle \|\nabla \boldsymbol{\sigma}\|_2^2 \rangle^{1/3} (1 + \ln Re + \ln \langle \|\nabla \boldsymbol{\sigma}\|_2^2 \rangle^{1/2})^{1/3}, \quad (4.46b)$$

where, again, $\|\cdot\|_2^2 = \int_{\Omega} |\cdot|^2 d\mathbf{x}$, $|\boldsymbol{\sigma}|^2 = \sum_{i,j} |\sigma_{ij}|^2$ and $|\nabla \boldsymbol{\sigma}|^2 = \sum_{i,j,k} |\partial_k \sigma_{ij}|^2$. These conditions depend on estimates for $\langle \|\boldsymbol{\sigma}\|_2^3 \rangle$ and $\langle \|\nabla \boldsymbol{\sigma}\|_2^2 \rangle$. It has been shown in Ref. [24] that these are at least exponential in time and thus cannot be used. Until these bounds are improved, direct numerical simulations will be necessary to find their behaviour in terms of Wi .

4.5. Direct numerical simulations of elastic turbulence

The conditions that the time average in Eq. (4.26) must satisfy (so that any N -dimensional volume contracts) were reduced after a series of estimations to two inequalities (4.46a) and (4.46b), which have terms that currently do not have practical analytical bounds. Direct numerical solutions will then be used to obtain estimates for the terms $\langle \|\boldsymbol{\sigma}\|_2^3 \rangle$ and $\langle \|\nabla \boldsymbol{\sigma}\|_2^2 \rangle$. These simulations were performed in collaboration with A. Gupta.

The solutions of the Oldroyd-B model in Eqs. (4.24) are simulated using the approach described in Refs. [40] and [41]. For the time integration, the fourth-order Runge–Kutta scheme with timestep $\delta t = 10^{-4}$ was used, while the fourth-order central-finite-difference scheme with 1024^2 collocation points is employed for the spatial derivatives. To accurately resolve the steep gradients of the polymer conformation tensor $\boldsymbol{\sigma}$, the Kurganov–Tadmor scheme was applied to the advection term in Eq. (4.24b) [46] (see Ref. [76] for the application of this scheme to viscoelastic fluids), which allows us to set $Pe = \infty$ in (4.24b). The velocity is calculated from the vorticity via the Poisson equation $\Delta \psi = \omega$, where ψ is the stream function: $\mathbf{u} = \nabla^\perp \psi$. The pseudospectral method is used to solve the Poisson equation in Fourier space. The simulations were performed on $[0, 2\pi]^2$ and the solutions were rescaled appropriately.

Three kinds of forcing are considered: a cellular forcing

$$f = -f_0 n [\cos(nx) + \cos(ny)]$$

with $n = 4$, a cellular forcing with $n = 10$, and a Kolmogorov forcing

$$f = -f_0 n \cos(nx)$$

with $n = 8$ (see Fig. 4.4 for a snapshot of a simulation in the cellular flow in the presence of polymers). In all simulations f_0 is chosen so that the resulting Re is below the critical Reynolds number Re_c above which inertial instabilities occur, in particular, $Re = Re_c/\sqrt{2}$ (see also Sec. 5.2 for more details on the Kolmogorov flow). Hence in the absence of polymers ($\beta = 0$) the stationary vorticity field shows alternating vortices and antivortices for the cellular forcing and a parallel sinusoidal flow for the Kolmogorov forcing. The parameter β is set to $\beta = 0.2$. A different value of β simply rescales the value of Wi in the simulations. It was checked that in

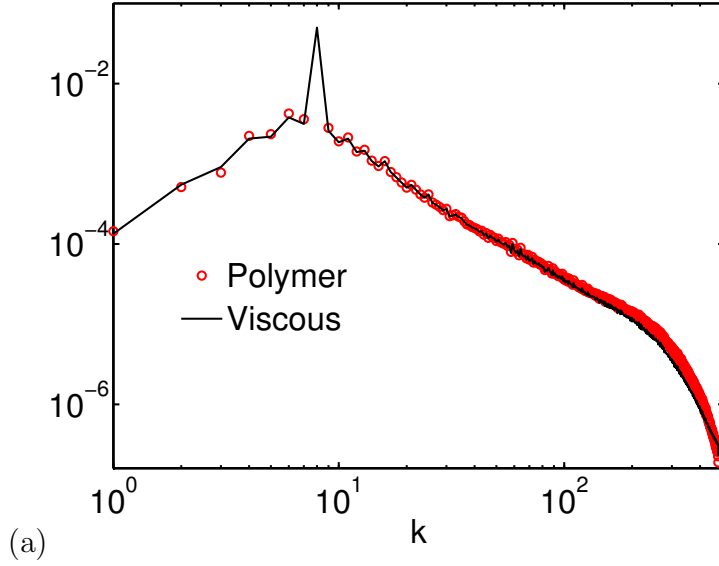


FIGURE 4.5. The kinetic-energy balance in wave-number space is written: $\partial_t E(k) + T(k) = T_p(k) - 2\nu k^2 E(k) + F(k)$, where $T(k)$ is the energy transfer due to inertia, $T_p(k)$ is the polymer contribution, and $F(k)$ is the forcing term. $T_p(k)$ (red) and $2\nu k^2 E(k)$ (black) are shown in the steady state for a Kolmogorov forcing ($n = 8, f_0 = 1.28$) and $Re = 0.7Re_c$ (see Fig. 4.6(c))

the elastic-turbulence regime, the kinetic-energy transfer due to the fluid inertia is negligible, so the chaotic dynamics is entirely due to polymer stresses (see Fig. 4.5).

The numerical simulations show that $\langle \|\nabla \sigma\|_2^2 \rangle^{1/3}$ is greater than $\langle \|\sigma\|_2^3 \rangle^{1/3}$ and, at large Wi , $\langle \|\nabla \sigma\|_2^2 \rangle^{1/3} \sim Wi^\alpha$ with $\alpha \approx 0.7$ for the three different forcings considered here (see Fig. 4.6 (a)–(c)). This result is in agreement with the observation of large gradients in the polymer conformation field in Fig. 4.4 as well in previous numerical simulations [7, 8]. It follows that the value of N such that N -volumes contract is determined by inequality (4.46b). The conclusion is that in the elastic-turbulence regime and under the specified assumptions, the two-dimensional Oldroyd-B model has a finite-dimensional global attractor with Lyapunov dimension

$$d_L(\mathcal{A}) \leq \mathcal{N}, \quad (4.47)$$

where \mathcal{N} is the minimum value of N satisfying (4.46b). Thus, up to logarithmic corrections,

$$\boxed{d_L(\mathcal{A}) \lesssim cRe^{2/3} \langle \|\nabla \sigma\|_2^2 \rangle^{1/3} \sim C Wi^\alpha}, \quad (4.48)$$

where $\alpha \approx 0.7$ and C depends on Re . Further numerical simulations at smaller values of $Re = 0.35Re_c$ indicate that α does not depend on Re . It is worth noting that since $\|\nabla \sigma\|$ grows with Wi , inequality (4.46a) and (4.46b) implies that lower Re requires higher Wi to obtain the same attractor dimension. This is in agreement with the stability analysis of the Oldroyd-B model, according to which the critical Wi for the appearance of elastic instabilities increases as Re decreases (e.g., Refs. [12, 47]).

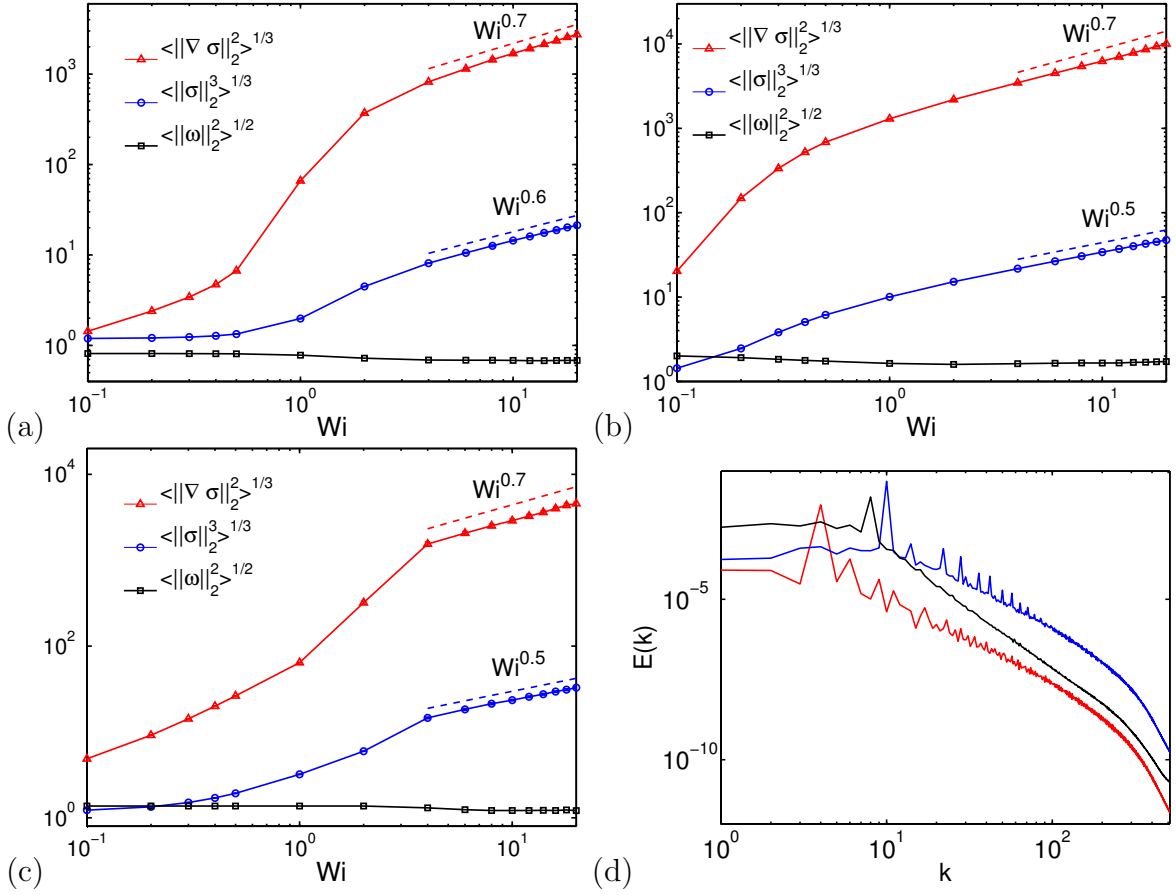


FIGURE 4.6. Plot of $\langle \|\omega\|_2^2 \rangle^{1/2}$ (black squares), $\langle \|\sigma\|_2^3 \rangle^{1/3}$ (blue circles) and $\langle \|\nabla \sigma\|_2^2 \rangle^{1/3}$ (red triangles) as a function of Wi for $Re = Re_c/\sqrt{2}$, $\beta = 0.2$, and (a) cellular forcing with $n = 4$, $f_0 = 0.16$, (b) cellular forcing with $n = 10$, $f_0 = 2.50$, (c) Kolmogorov forcing with $n = 8$, $f_0 = 1.28$; (d) Kinetic-energy spectrum for $Wi = 20$ for case (a) in red, case (b) in blue and case (c) in black. The spectrum shows a power-law behaviour $E(k) \simeq k^{-a}$ with $a \approx 3.1$ for case (a), $a \approx 3.0$ for case (b) and $a \approx 3.7$ for case (c).

4.6. Conclusions and perspectives

Through a mathematical and numerical analysis of the two-dimensional Oldroyd-B model in the elastic-turbulence regime, a practical estimate of the dimension of its (assumed) global attractor is provided. The estimate shows that the complexity of the attractor is related to the formation of large gradients in the polymer conformation field.

The asymptotic power-law dependence of $d_L(\mathcal{A})$ on Wi was found to be the same for different forcings considered. The potential universality of the exponent α still remains to be confirmed. Likewise the study assumed a periodic boundary condition. It would be interesting to investigate if the exponent α depends on the forcing and the boundary conditions.

As mentioned in the introduction of this chapter, the main limitation of the Oldroyd-B model is the absence of a maximum polymer elongation. Other constitutive models of polymer solutions, such as the FENE-P model, overcome this limitation by introducing in Eq. (4.21) a nonlinear elastic force $f(\mathbf{R}^2) = (1 - \mathbf{R}^2/R_{\max})^{-1}$ that diverges when $\text{Tr } \boldsymbol{\sigma} = R^2$ approaches the square of the maximum elongation R_{\max} . Indeed, FENE-P stands for “finitely-extensible nonlinear elastic” dumbbell model using the Peterlin approximation in the averaging over thermal noise (see Refs. [41, 73] for the application of the FENE-P model to the study of elastic turbulence). However, using a nonlinear elastic force does not prevent the formation of large gradients in the $\boldsymbol{\sigma}$ -field [73]. In other words, large values of $\nabla \boldsymbol{\sigma}$ seem to occur independently of the form of the force that describes the elasticity of polymers. The estimate (4.48) depends on $\|\nabla \boldsymbol{\sigma}\|_2$ rather than $\|\boldsymbol{\sigma}\|_2$. This fact suggests that even if the estimate (4.48) is based on the Oldroyd-B model, it may also be relevant to other constitutive models.

Our analysis can be adapted to the Oldroyd-B model coupled with the unsteady Stokes equations,

$$\partial_t \mathbf{u} = -\nabla p + \frac{1}{Re} \Delta \mathbf{u} + \frac{\beta}{Wi Re} \nabla \cdot \boldsymbol{\sigma} + \mathbf{F} \quad (4.49)$$

in which the $\mathbf{u} \cdot \nabla \mathbf{u}$ term is set to zero. The estimates for N given in (4.46a) and (4.46b) are unchanged. The $Re = 0$ case, in which (4.23a) is replaced with the Stokes equations [72, 73],

$$0 = -\nabla p + \frac{1}{Re} \Delta \mathbf{u} + \frac{\beta}{Wi Re} \nabla \cdot \boldsymbol{\sigma} + \mathbf{F} \quad (4.50)$$

requires by contrast a separate mathematical analysis and a new set of numerical simulations, because ω depends on $\boldsymbol{\sigma}$ via a time-independent differential relation and the system (4.24) reduces to a dynamical system in the $\boldsymbol{\sigma}$ -space only.

Lastly, elastic turbulence is observed at low Re and high Wi . When both Re and Wi are high, the addition of polymers to a two-dimensional turbulent flow suppresses large-scale velocity fluctuations [2]. This phenomenon is once again correctly reproduced by the Oldroyd-B model [11]. Estimate (4.43), which gives a sufficient condition for the contraction of N -volumes, holds for all values of Re . It would be interesting to investigate the implications of this estimate for the attractor dimension in the high- Re regime.

4.7. Appendices

4.7.1. Useful inequalities.

Lieb–Thirring inequality. The Lieb–Thirring inequality was used, for instance, in inequality (4.37). It states that for orthonormal functions $\phi_i, n = 1, \dots, N$ in d dimensions [26, 48]

$$\int_{\Omega} \left(\sum_{n=1}^N |\phi_n|^2 \right)^{\frac{d+2}{d}} d\mathbf{x} \leq c \sum_{n=1}^N \int_{\Omega} |\nabla \phi_n|^2 d\mathbf{x}. \quad (4.51)$$

Inequality (4.30). The Lieb–Thirring inequality can also be used to prove the inequality on the trace $\text{Tr}[-\Delta \mathbf{P}_N]$ in (4.30) by first using Cauchy–Schwarz inequality:

$$N^2 = \left[\int_{\Omega} \sum_{n=1}^N |\phi_n|^2 d\mathbf{x} \right]^2 \leq \left[1 \cdot \left(\int_{\Omega} \left(\sum_{n=1}^N |\phi_n|^2 \right)^2 d\mathbf{x} \right)^{1/2} \right]^2 = \int_{\Omega} \left(\sum_{n=1}^N |\phi_n|^2 \right)^2 d\mathbf{x}$$

Then by using the Lieb–Thirring inequality,

$$N^2 \leq \int_{\Omega} \left(\sum_{n=1}^N |\phi_n|^2 \right)^2 d\mathbf{x} \leq c \sum_{n=1}^N \int_{\Omega} |\nabla \phi_n|^2 d\mathbf{x} = c \text{Tr}[-\Delta \mathbf{P}_N] \quad (4.52)$$

The reader is reminded that the constant c may differ from equation to equation.

L^∞ estimate. The L^∞ estimate for functions \mathbf{v}_n with orthonormal gradients and defined over the periodic box $[0, L]^2$ is [21]

$$\left\| \sum_{n=1}^N |\mathbf{v}_n|^2 \right\|_{\infty} \leq c (1 + \ln(L^2 \text{Tr}[-\Delta \mathbf{P}_N])). \quad (4.53)$$

In this chapter, $L = 1$. A proof may be found in Refs. [21, 25].

Jensen’s inequality. Lastly, Jensen’s inequality for a *concave* function states that for any function g and a concave function h defined on the domain Ω :

$$h\left(\frac{1}{|\Omega|} \int_{\Omega} g(\mathbf{x}) d\mathbf{x}\right) \geq \frac{1}{|\Omega|} \int_{\Omega} h(g(\mathbf{x})) d\mathbf{x}, \quad (4.54)$$

where $|\Omega| = \int_{\Omega} 1 d\mathbf{x}$.

4.7.2. Proof of Statement (4.44). Here a proof of (4.44) is provided under the assumption that $\mathcal{N} \geq 4$, which holds for a chaotic regime: for any $0 \leq \lambda < 3/2$ and expression \mathcal{M}

$$\mathcal{N} \geq c\mathcal{M}^{1/(2-\lambda)}(1 + \ln \mathcal{M})^{1/2(2-\lambda)} \implies \mathcal{N}^2 \geq c\mathcal{M}\mathcal{N}^\lambda(1 + \ln \mathcal{N}^2)^{1/2} \quad (4.55)$$

Suppose, on the contrary, that

$$\mathcal{N}^2 < c\mathcal{M}\mathcal{N}^\lambda(1 + \ln \mathcal{N}^2)^{1/2}, \quad (4.56)$$

then

$$\begin{aligned} \frac{\mathcal{N}^{2(2-\lambda)}}{1 + \ln \mathcal{N}^2} &< c^2 \mathcal{M}^2 \\ (4 - 2\lambda) \ln \mathcal{N} - \ln(1 + 2 \ln \mathcal{N}) &< 2 \ln |\mathcal{M}| + 2 \ln c \\ \frac{3 - 2\lambda}{2} \ln \mathcal{N}^2 &< 2 \ln |\mathcal{M}| + 2 \ln c \end{aligned}$$

where the fact that $\ln \mathcal{N} \geq \ln(1 + 2 \ln \mathcal{N})$ if $\mathcal{N} \geq 4$ was used. Then,

$$\begin{aligned} 1 + \ln \mathcal{N}^2 &< \frac{4}{3 - 2\lambda} \ln |\mathcal{M}| + \frac{4}{3 - 2\lambda} \ln c + 1 \\ 1 + \ln \mathcal{N}^2 &< c(1 + \ln |\mathcal{M}|) \end{aligned} \quad (4.57)$$

Putting Eqs. (4.56),(4.57) together, then

$$\mathcal{N}^2 < c\mathcal{M}\mathcal{N}^\lambda(1 + \ln |\mathcal{M}|)^{1/2} \quad (4.58)$$

which contradicts the left side of the implication in (4.55). The assumption (4.56) is then invalid and the implication (4.55) holds.

Emergence of chaos in a viscous solution of rodlike polymers

5.1. Introduction

In a laminar flow the dispersion of substances occurs by molecular diffusion, which operates on extremely long time scales. Microfluidic flows, such as those used in biochemistry, are typically laminar because of their small Reynolds number (Re) and are thus ineffective in mixing. Various strategies have therefore been developed to accelerate mixing and dispersion at low fluid inertia [57, 69, 70]. The available strategies are commonly divided into two classes, passive or active, according to whether the desired effect is obtained through the geometry of the device or through an oscillatory forcing within the device itself [70]. An alternative method for improving the mixing properties of low-Reynolds-number flows was proposed by Groisman and Steinberg [37] and uses elastic turbulence (see the introduction of Part II). The effectiveness of this mixing method can be seen in Fig. 5.1, where in particular, the lower left panel is a snapshot of a completely Newtonian fluid that did not mix whereas a polymer solution exhibited mixing (right panel) under exactly the same set-up (see Refs. [1, 18, 45, 62, 75] for other experiments using elastic turbulence to facilitate mixing).

It is well-known that when the Reynolds number is large elastic- and rigid-polymer solutions exhibit remarkably similar macroscopic behaviour (see, e.g., Refs. [5, 34, 60, 77]). In both cases the turbulent drag is considerably reduced compared to that of the solvent alone, according to a phenomenology that seems to depend little on the microscopic structure of the solution. In particular, when either type of polymer is added in sufficiently high concentrations to a turbulent channel flow of a Newtonian fluid, the velocity profile continues to depend logarithmically on the distance from the walls of the channel, but the mean velocity increases to a value known as maximum-drag-reduction asymptote. It would then be valid to ask if the similarity between elastic- and rigid-polymer solutions that is present in regimes at high values of Re carries over to the low- Re regime, i.e. can chaos be generated at low Reynolds numbers via the addition of *rigid* polymers? An affirmative answer to this question would identify an alternative mechanism for generating chaos in low-inertia polymer solutions that does not rely on elasticity.

Section 5.2 first revisits the model for rodlike polymer solutions that was used by Benzi et al. [5] to numerically simulate drag reduction and then reintroduces the Kolmogorov flow. Details on the numerical simulation of the coupled set of equations describing the velocity and rigid polymers in a low- Re number regime is presented in Sec. 5.3. The results presented in Sec. 5.4 reveal that the addition of rodlike polymers produce a chaotic regime in an otherwise laminar flow. Concluding remarks on the comparison of the chaotic regime to elastic turbulence and on possible extensions of this work are then provided at the end.

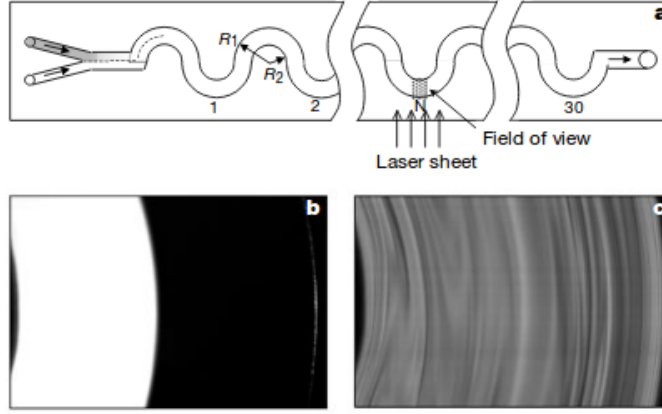


FIGURE 5.1. (a) An experimental microfluidic set-up of curved rings where two identical fluids (one is dyed) are injected before the curve labeled 1. The depth of the channel is 3 mm, and the rings have an inner radius of 3 mm and an outer radius of 6 mm. The snapshots indicate the state of mixing of (b) a Newtonian fluid (65% saccharose and 1% NaCl in water) and (c) a viscoelastic fluid polymer solution (80 ppm of polyacrylamide) with $Wi = 6.7$, both at $Re = 0.16$ and taken at curve labeled 29. Further details are available in Ref. [37]. White regions in (b) and (c) indicate the dyed fluid. Reprinted by permission from Macmillan Publishers Ltd: *Nature* **410**, 905, copyright (2001) (Ref. [37]).

5.2. The model of rodlike-polymer solutions

To highlight the role of rigidity, consider a dilute solution of inertialess rodlike polymers. The polymer phase is described by a symmetric unit-trace tensor field

$$\mathcal{R}_{ij}(\mathbf{x}, t) = \overline{n_i n_j}, \quad (5.1)$$

where \mathbf{n} is the orientation of a rigid polymer and the average is taken over the polymers contained in a volume element at position \mathbf{x} . The evolution of \mathbf{n} follows Jeffery's equation:

$$\partial_t n_i + u_k \partial_k n_i = (\delta_{ik} - n_i n_k) \partial_l u_k n_l. \quad (5.2)$$

The coupled evolution of the conformation tensor $\mathcal{R}(\mathbf{x}, t)$ and the incompressible velocity field $\mathbf{u}(\mathbf{x}, t)$ is then given by the following equations [27, 64]:

$$\partial_t u_i + u_k \partial_k u_i = -\partial_i p + \nu \partial^2 u_i + \partial_k \sigma_{ik} + f_i, \quad (5.3a)$$

$$\partial_t \mathcal{R}_{ij} + u_j \partial_j \mathcal{R}_{ij} = (\partial_k u_i) \mathcal{R}_{kj} + \mathcal{R}_{ik} (\partial_k u_j) - 2\mathcal{R}_{ij} (\partial_l u_k) \mathcal{R}_{kl}, \quad (5.3b)$$

where $\partial_k = \partial/\partial x_k$, p is pressure, ν is the kinematic viscosity, and \mathbf{f} is a body-force. The polymer stress tensor $\boldsymbol{\sigma}$ takes the form [27]:

$$\sigma_{ij} = 6\nu\eta_p \mathcal{R}_{ij} (\partial_l u_k) \mathcal{R}_{kl}, \quad (5.4)$$

where η_p is proportional to the polymer concentration (the definition of η_p here is a factor of the η_p in Ref. [6]). Its value determines the amplitude of the polymer feedback on the flow. First note that the differences of Eqs. (5.3) to that of the Oldroyd-B model in Eqs. (4.23) stem even from how the end-to-end orientation vector \mathbf{n} is modeled from that in Eq. (4.21). To remind the reader of this difference, the

notation \mathcal{R} is instead used for the conformation tensor of rigid rods. Also, Eqs. (5.3) and (5.4) are based on a quadratic approximation proposed by Doi and Edwards [27]. More sophisticated closures have been used in the literature (see *e.g.* Ref. [52] and references therein); here, the simplest model that may display instabilities at low Reynolds (Re) number is considered. Indeed, such a handy approximation did not prevent this model from exhibiting drag reduction [5]. In addition, the rotational diffusion of polymers is disregarded to ensure that any instability originates from the presence of polymers alone.

For large values of the Re , the system described by Eqs. (5.3) has been shown to reproduce the main features of drag reduction in turbulent solutions of rodlike polymers [5, 6, 64]. Here, the same system is studied but at small values of the Reynolds number. Equations (5.3) are solved over a two-dimensional 2π -periodic box and \mathbf{f} is taken to be the Kolmogorov force

$$\mathbf{f} = \left(0, F \sin \left(\frac{x}{L} \right) \right), \quad (5.5)$$

where L gives the scale of the forcing. In the absence of polymers ($\eta_p = 0$) the flow has the laminar solution

$$\mathbf{u} = \left(0, U_0 \sin \left(\frac{x}{L} \right) \right) \quad (5.6)$$

with $U_0 = FL^2/\nu$, which becomes unstable when $Re = U_0L/\nu$ exceeds the critical value $Re_c = \sqrt{2}$ and turbulent when Re is further increased [54]. Even in the turbulent regime, the mean flow has the sinusoidal form

$$\langle \mathbf{u} \rangle = \left(0, U \sin \left(\frac{x}{L} \right) \right), \quad (5.7)$$

where $\langle \cdot \rangle$ denotes an average over the variable y and over time.

The Kolmogorov force has been previously used in the context of non-Newtonian fluid dynamics to theoretically and numerically study turbulent drag reduction [13], the formation of low- Re instabilities in viscoelastic [9, 12] and rheopectic flows [14], and in elastic turbulence [7, 8]. In these studies, there is an extra stress tensor in the evolution of the flow field that couples it to the evolution of the conformation tensor, as in Eq. (5.3a). In the presence of elastic Oldroyd-B polymers, a non-trivial stability diagram on the Re - Wi phase space was drawn (as in Chap. 4, Wi is the Weissenberg number); increasing Wi and keeping $Re < Re_c$ induces elastic instabilities [12]. Moreover, the resulting mean flow remains sinusoidal both in the elastic turbulence and in the drag reduction regime [7, 8, 9]. There is, at present, no reason to expect that the mean flow will remain sinusoidal in the presence of rodlike polymers—this assumption is confirmed in the simulations described below.

Under the action of the forcing (5.5) and decoupling the polymer feedback ($\eta_p = 0$) results to a sinusoidal laminar flow as in Eq. (5.7); the conformation tensor at equilibrium is

$$\mathcal{R} = \begin{pmatrix} 0 & 0 \\ 0 & 1 \end{pmatrix}, \quad (5.8)$$

which was derived by setting the time derivative in Eq. (5.3b) to zero and keeping the mean dimensionless length of the rods at 1.

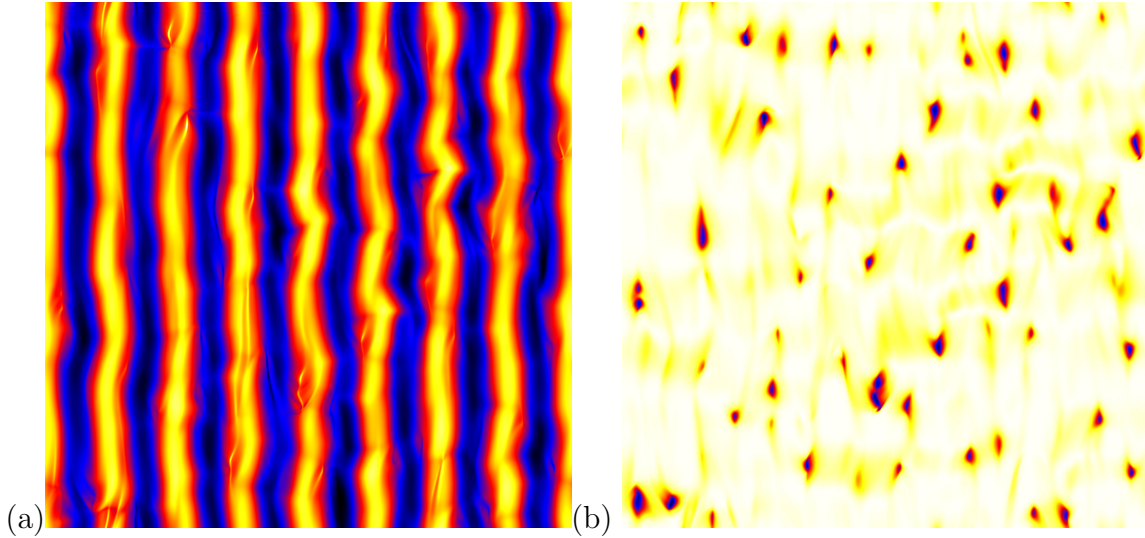


FIGURE 5.2. (a) Snapshot of the vorticity field ω for polymer concentration $\eta_p = 3$ and forcing scale $L = 1/8$. Black (white) represents regions of negative (positive) vorticity. (b) Snapshot of the component \mathcal{R}_{11} of the conformation tensor \mathcal{R} corresponding to the vorticity field. Black represents one, white represents zero.

5.3. Numerical simulations

To see if a chaotic regime manifests in a polymer solution of rigid rods, numerical simulations of Eqs. (5.3) with a Kolmogorov forcing (5.5) are then performed by using a dealiased pseudospectral method with 1024^2 gridpoints. The time-integration uses a fourth-order Runge-Kutta method with timestep $dt = 10^{-5}$ or smaller—the stiffness of the equations indeed increases with η_p . The viscosity is set to $\nu = 1$, the length scale of the forcing is either $L = 1/4$ or $L = 1/8$, and F is chosen so as to keep $Re = 1$ fixed below Re_c in the absence of rods, i.e. a stable laminar flow results if $\eta_p = 0$. The feedback coefficient is varied from $\eta_p = 1$ to $\eta_p = 5$ to explore the effect of polymer concentration on the stability of the flow. Initially, the flow is a weak perturbation of the $\eta_p = 0$ stable solution, while the components of the conformation tensor \mathcal{R} are randomly distributed. The latter permits a shorter transient than from the stable configuration of the $\eta_p = 0$ case (see Eq. (5.8)), in which all polymers are aligned with the shear direction.

An inspection of the vorticity field $\omega = |\nabla \times \mathbf{u}|$ reveals that the flow is strongly modified by the presence of the rods (see Fig. 5.2(a)). The streamlines wiggle over time and thin filaments form. These filaments correspond to appreciable localized perturbations of the tensor \mathcal{R} away from the laminar fixed point (see Fig. 5.2(b)) and are due to the rods being unaligned with the shear direction. A movie showing the vorticity during the transition from a quasiperiodic state to a chaotic regime with $\eta_p = 3$ and $L = 1/4$ is available at <http://math.unice.fr/~elcplan/transition.gif>. In the movie, black (white) represents negative (positive) vorticity.

5.4. Analysis

To quantify the effect of the rods on the flow and see if they induce forces similar to the elastic forces in the case of viscoelastic solutions, the amount of polymer stress

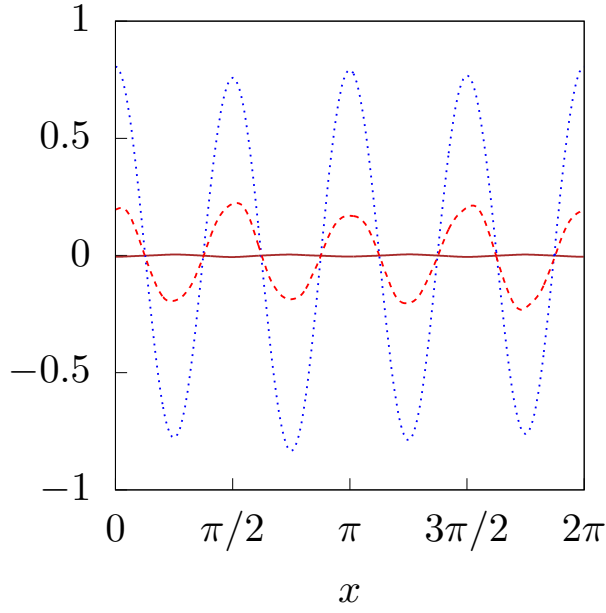


FIGURE 5.3. Profiles of Reynolds stress Π_r (brown, solid), viscous stress Π_ν (blue, dotted), and polymer stress Π_p (red, dashed), divided by the amplitude of the total stress Π_{tot} for $L = 1/4$ and $\eta_p = 3$.

η_p	L	Π_r/Π_{tot}	Π_ν/Π_{tot}	Π_p/Π_{tot}
1	1/8	0.001	0.996	0.004
2	1/8	0.004	0.887	0.110
3	1/4	0.005	0.787	0.209
3	1/8	0.005	0.795	0.200
4	1/8	0.007	0.710	0.284
5	1/8	0.006	0.647	0.347

TABLE 5.1. The stresses Π_r , Π_ν , and Π_p divided by the total stress Π_{tot} for different values of the concentration η_p and forcing scale L .

contribution is calculated and compared to the viscous stress. In the steady state the momentum budget can be obtained by averaging Eq. (5.3a) over y and time:

$$\partial_x \Pi_r = \partial_x (\Pi_\nu + \Pi_p) + f_y, \quad (5.9)$$

where $\Pi_r = \langle u_x u_y \rangle$, $\Pi_\nu = \nu \partial_x \langle u_y \rangle$, and $\Pi_p = \langle \sigma_{xy} \rangle$ are the Reynolds, viscous, and polymer stress, respectively. Remarkably these profiles were found to be sinusoidal as in the $\eta_p = 0$ case, namely $\Pi_r = -S \cos(x/L)$, $\Pi_\nu = \nu U L^{-1} \cos(x/L)$ and $\Pi_p = \Sigma \cos(x/L)$ (see Fig. 5.3). Equation (5.9) then yields the following relation between the amplitudes S, U and Σ of the different contributions to the stress:

$$S + \frac{\nu U}{L} + \Sigma = FL. \quad (5.10)$$

The contributions for different values of the concentration η_p are given in Table 5.1 and the inset of Fig. 5.4. The results confirm that the polymer contribution to the total stress increases with η_p whereas that of the viscous stress decreases.

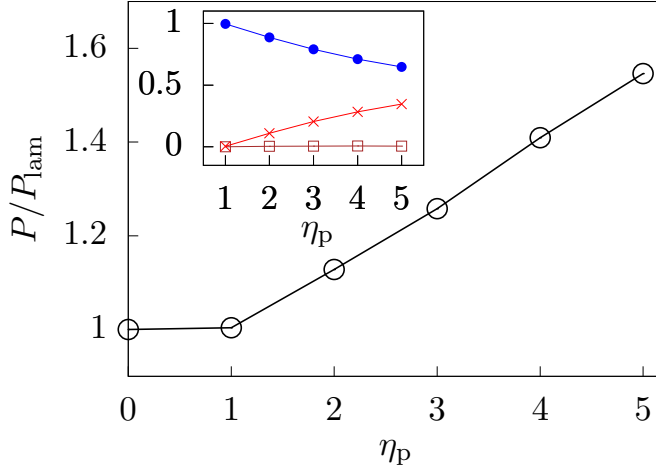


FIGURE 5.4. The normalized mean power injected P/P_{lam} as a function of η_p . Inset: The amplitudes of the stresses Π_r (brown \square), Π_ν (blue \bullet), and Π_p (red \times) divided by the amplitude of the total stress Π_{tot} for $L = 1/8$ and different values of η_p (see Table 5.1).

The contribution of the Reynolds stress is extremely small (less than 10^{-2}), which demonstrates that inertial effects remain negligible as η_p is increased.

That this increase in the polymer contribution to the stress translates to a chaotic regime remains to be verified: one can check if the injection of polymers generates an increase in the flow resistance, which can be quantified by calculating the mean power $P = \langle \mathbf{f} \cdot \mathbf{u} \rangle = FU/2$ needed to maintain a mean flow U ($\langle \cdot \rangle$ now denotes a space-time average). In the absence of polymers, the force required to obtain the same mean flow would be $F_0 = \nu U/L^2$ and the corresponding mean power would be $P_{\text{lam}} = F_0 U/2$. Figure 5.4 shows the ratio

$$\frac{P}{P_{\text{lam}}} = \frac{F}{F_0} = \frac{FL^2}{\nu U} \quad (5.11)$$

as a function of η_p and confirms that more power is required to keep the mean flow fixed in solutions with higher concentrations.

An alternative way to demonstrate the increase in the flow resistance is to keep the forcing fixed and compare the kinetic energies. The time series of the kinetic energy in Fig. 5.5 show that, in the case of a low concentration ($\eta_p = 1$), the system repetitively attempts but fails to escape the laminar regime in a quasiperiodic manner. The amount of kinetic energy is initially close to that in the laminar regime. After some time, the solution dissipates a small fraction of kinetic energy but quickly relaxes back towards the laminar regime until it restarts this cyclic pattern. In contrast, for higher concentrations the kinetic energy is significantly reduced and, after an initial transient, it fluctuates chaotically around a constant value. It was observed that using a different initial condition for the conformation tensor \mathcal{R} may give rise to longer transients that involve a quasiperiodic sequence of activations and relaxations comparable to that observed for low values of η_p . The statistical steady state achieved at later times is nevertheless independent of any particular choice of

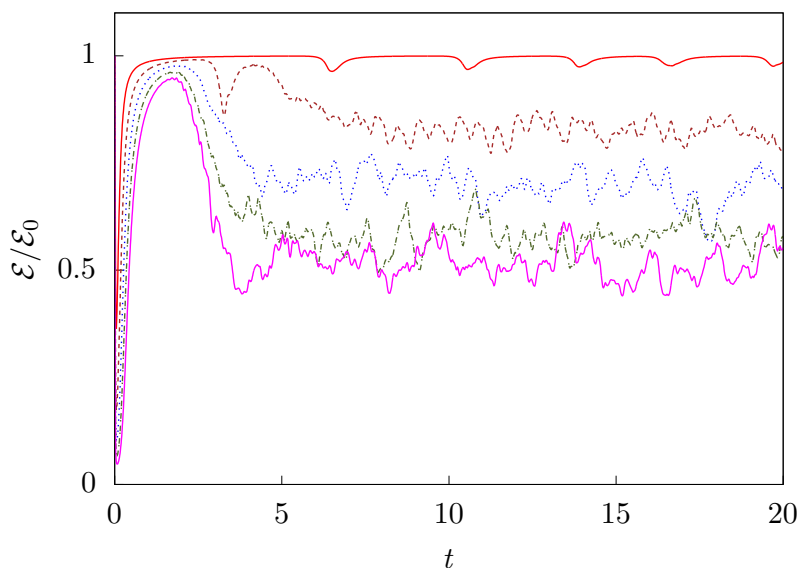


FIGURE 5.5. The kinetic energy $\mathcal{E} = \langle \mathbf{u}^2 \rangle / 2$ (averaged over space) for increasing polymer concentration η_p (from top to bottom): $\eta_p = 1$ (red, solid), $\eta_p = 2$ (brown, dashed), $\eta_p = 3$ (blue, dotted), $\eta_p = 4$ (green, dash-dotted) and $\eta_p = 5$ (magenta, solid) divided by the kinetic energy $\mathcal{E}_0 = F^2 L^4 / 2\nu^2$ corresponding to $\eta_p = 0$ and with the same value of the force $F = 512$ and forcing scale $L = 1/8$.

initial conditions. Figures 5.4 and 5.5 furthermore suggest the presence of a threshold concentration for the appearance of chaotic fluctuations.

Further insight into the apparent chaotic regime is gained by examining the kinetic-energy spectrum. For sufficiently large values of η_p , the spectrum behaves as a power law $E(k) \sim k^{-\alpha}$, where the exponent depends both on the scale of the force and on the concentration and varies between 4 and 5 (see Fig. 5.6). Therefore a wide range of scales is activated and these results in an enhancement of the mixing properties of the flow. Furthermore, the energy transfer due to the fluid inertia is negligible, and the dynamics is characterized by a scale-by-scale balance between the polymer energy transfer and viscous dissipation (inset of Fig. 5.6).

5.5. Concluding remarks and perspectives

The chaotic regime described here has properties comparable to those of elastic turbulence in viscoelastic fluids, inasmuch as the flow resistance is increased with the addition of rods and the kinetic-energy spectrum displays a power-law steeper than k^{-3} . In addition the Reynolds stress and the energy transfer due to the fluid inertia are negligible; hence the emergence of chaos is entirely attributable to polymer stresses.

This chapter establishes an analogy between the behaviour of viscoelastic fluids and that of solutions of rodlike polymers at low Re , similar to what is observed at high Re number. This demonstrates that elasticity is not essential to generate a chaotic dynamics at low inertia. The results therefore show that a chaotic behaviour at low Re can also be observed in fluids that are not viscoelastic. These results

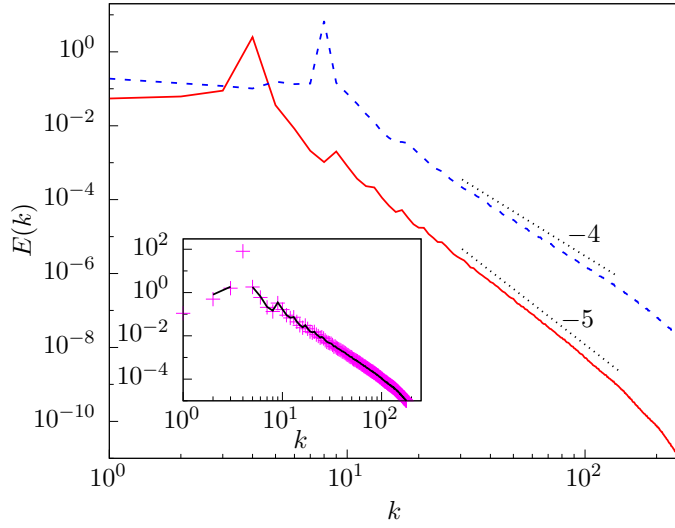


FIGURE 5.6. The kinetic energy spectrum $E(k)$ for $L = 1/4$, $\eta_p = 3$ (solid red) and $L = 1/8$, $\eta_p = 5$ (dashed blue). The two black dotted segments represent k^{-4} and k^{-5} . Inset: The unsigned kinetic-energy dissipation spectrum $2\nu k^2 E(k)$ (magenta +) and the polymer energy transfer (solid black) for $L = 1/4$ and $\eta_p = 3$.

suggest an alternative mechanism to enhance mixing in microfluidic devices that presumably has the benefit of being less affected by the degradation observed in elastic turbulence [38]. Indeed, there are experimental evidences that for rodlike polymers the degradation due to large strains is weaker than for elastic polymers [61].

It is hoped that these results will stimulate experimental studies on the dynamics of rodlike polymer solutions at low Re . Open questions concern the dependence of the mixing properties of these solutions on the type of force and on the boundary conditions. Experimental and numerical results of elastic turbulence indicate a power law with exponent between -3 and -4 [7, 8, 44], which is less steep than the power law observed here (between -4 and -5). It would then be informative to further quantify similarities and differences between the instabilities in rigid polymer solutions and those in viscoelastic solutions, for instance, to check if the slope of the power law is significantly different, if stability diagram of the $Re - \eta_p$ space is similar to that in Ref. [12], or if the degrees of chaoticity (quantified via the Lyapunov exponents) in the rigid polymer solutions compare to those in viscoelastic cases. Lastly, the orientation and rotation statistics of microscopic rods in turbulent flows has recently attracted a lot of attention [28, 39, 42, 59, 65, 78]; it would be interesting to investigate the dynamics of individual rods in the flow regime studied in this chapter.

Bibliography - Part II

- [1] Abed WM, Whalley RD, Dennis DJC, Poole RJ. Experimental investigation of the impact of elastic turbulence on heat transfer in a serpentine channel *J. Non-Newtonian Fluid Mech.* **231**, 68 (2016).
- [2] Amarouchene Y, Kellay H. Polymers in 2D turbulence: suppression of large scale fluctuations. *Phys. Rev. Lett.* **89**, 104502 (2002)
- [3] Barrett JW, Süli, E. Existence and equilibration of global weak solutions to kinetic models for dilute polymers I. *Math. Models Methods Appl. Sci.* **21**, 1211 (2011).
- [4] Beaumont J, Louvet N, Divoux T, Fardin M-A, Bodiguel H, Lerouge S, Manneville S, Colin A. Turbulent flows in highly elastic wormlike micelles. *Soft Matter* **9**, 735 (2010).
- [5] Benzi R, Ching ESC, Lo TS, L'vov VS, Procaccia I. Additive equivalence in turbulent drag reduction by flexible and rodlike polymers. *Phys. Rev. E* **72**, 016305 (2005).
- [6] Benzi R, Ching ESC, De Angelis E, Procaccia I. Comparison of theory and direct numerical simulations of drag reduction by rodlike polymers in turbulent channel flows. *Phys. Rev. E* **77**, 046309 (2008).
- [7] Berti S, Bistagnino A, Boffetta G, Celani A, Musacchio S. Two-dimensional elastic turbulence. *Phys. Rev. E* **77**, 055306(R) (2008).
- [8] Berti S, Boffetta G. Elastic waves and transition to elastic turbulence in a two-dimensional viscoelastic Kolmogorov flow. *Phys. Rev. E* **82**, 036314 (2010).
- [9] Bistagnino A, Boffetta G, Celani A, Mazzino A, Puliafito A, Vergassola M. Non-linear dynamics of the viscoelastic Kolmogorov flow. *J. Fluid Mech.* **590**, 61 (2007).
- [10] Bodiguel H, Beaumont J, Machado A, Martinie L, Kellay H, Colin A. Flow enhancement due to elastic turbulence in channel flows of shear thinning fluids. *Phys. Rev. Lett.* **114**, 028302 (2015).
- [11] Boffetta G, Celani A, Musacchio S. Two-dimensional turbulence of dilute polymer solutions. *Phys. Rev. Lett.* **91**, 034501 (2003).
- [12] Boffetta G, Celani A, Mazzino A, Puliafito A, Vergassola M. The viscoelastic Kolmogorov flow: eddy viscosity and linear stability. *J. Fluid Mech.* **523**, 161 (2005).
- [13] Boffetta G, Celani A, Mazzino. Drag reduction in the turbulent Kolmogorov flow. *Phys. Rev. E* **71**, 036307 (2005).
- [14] Boi S, Mazzino A, Pralits JO. Minimal model for zero-inertia instabilities in shear-dominated non-Newtonian flows. *Phys. Rev. E* **88**, 033007 (2013).
- [15] Bonn D, Ingremeau F, Amarouchene Y, Kellay H. Large velocity fluctuations in small-Reynolds-number pipe flow of polymer solutions. *Phys. Rev. E* **84**, 045301(R) (2011).

- [16] Burghilea T, Segre E, Steinberg V. Statistics of particle pair separations in the elastic turbulent flow of a dilute polymer solution. *Europhys. Lett.* **68**, 529 (2004).
- [17] Burghilea T, Segre E, Steinberg V. Mixing by polymers: Experimental test of decay regime of mixing. *Phys. Rev. Lett.* **92**, 164501 (2004).
- [18] Burghilea T, Segre E, Bar-Joseph I, Groisman A, Steinberg V. Chaotic flow and efficient mixing in a microchannel with a polymer solution. *Phys. Rev. E* **69**, 066305 (2004).
- [19] Burghilea T, Segre E, Steinberg V. Elastic turbulence in von Karman swirling flow between two disks. *Phys. Fluids* **19**, 053104 (2007).
- [20] Clarke A, Howe AM, Mitchell J, Staniland J, Hawkes LA. How viscoelastic-polymer flooding enhances displacement efficiency. *SPE Journal* **21**, 0675 (2016).
- [21] Constantin P. Collective L^∞ -estimates for families of functions with orthonormal derivatives. *Indiana Univ. Math. J.* **36**, 603 (1987).
- [22] Constantin P, Foias C. Global Lyapunov exponents, Kaplan–Yorke formulas and the dimension of the attractors for 2D Navier–Stokes equations. *Comm. Pure Appl. Math.* **38**, 1 (1985).
- [23] Constantin P, Foias C, Temam R. On the dimension of the attractors in two-dimensional turbulence. *Physica D* **30**, 284 (1988).
- [24] Constantin P, Kliegl M. Note on global regularity for two-dimensional Oldroyd-B fluids with diffusive stress. *Arch. Rational Mech. Anal.* **206**, 725 (2012).
- [25] Doering CR, Gibbon JD. Note on the Constantin–Foias–Temam attractor dimension estimate for two-dimensional turbulence. *Physica D* **48**, 471 (1991).
- [26] Doering CR, Gibbon JD. *Applied analysis of the Navier–Stokes equations*. Cambridge University Press, (1995).
- [27] Doi M, Edwards SF. *The Theory of Polymer Dynamics*. Oxford Univ. Press, Oxford (1988).
- [28] Einarsson J, Mihiretie BM, Laas A, Ankardal S, Angilella JR, Hanstorp D, Mehlig B. Tumbling of asymmetric microrods in a microchannel flow. *Phys. Fluids* **28**, 013302 (2016).
- [29] Elgindi TM, Rousset F. Global regularity for some Oldroyd-B type models. *Comm. Pure Appl. Math.* **68**, 2005 (2015).
- [30] El-Kareh AW, Leal LG. Existence of solutions for all Deborah numbers for a non-Newtonian model modified to include diffusion. *J. Non-Newtonian Fluid Mech.* **33**, 257 (1989).
- [31] Fardin M-A, Lopez D, Croso J, Grégoire G, Cardoso O, McKinley GH, Lerouge S. Elastic turbulence in shear banding wormlike micelles. *Phys. Rev. Lett.* **104**, 178303 (2010).
- [32] Fouxon A, Lebedev V. Spectra of turbulence in dilute polymer solutions. *Phys. Fluids* **15**, 2060 (2003).
- [33] Gibbon JD, Titi E. Attractor dimension and small length scale estimates for the three-dimensional Navier–Stokes equations. *Nonlinearity* **10**, 109 (1997).
- [34] Gillissen JJJ. Polymer flexibility and turbulent drag reduction. *Phys. Rev. E* **78**, 046311 (2008).
- [35] Grilli M, Vázquez-Quesada A, Ellero M. Transition to turbulence and mixing in a viscoelastic fluid flowing inside a channel with a periodic array of cylindrical obstacles. *Phys. Rev. Lett.* **110**, 174501 (2013).
- [36] Groisman A, Steinberg V. Elastic turbulence in a polymer solution flow. *Nature* **405**, 53 (2000).

- [37] Groisman A, Steinberg V. Efficient mixing at low Reynolds numbers using polymer additives. *Nature* **410**, 905 (2001).
- [38] Groisman A, Steinberg V. Elastic turbulence in curvilinear flows of polymer solutions. *New J. Phys.* **6**, 29 (2004).
- [39] Gupta A, Vincenzi D, Pandit R. Elliptical tracers in two-dimensional, homogeneous, isotropic fluid turbulence: The statistics of alignment, rotation, and nematic order. *Phys. Rev. E* **89**, 021001(R) (2014).
- [40] Gupta A, Perlekar P, Pandit R. Two-dimensional homogeneous isotropic fluid turbulence with polymer additives. *Phys. Rev. E* **91**, 033013 (2015).
- [41] Gupta A, Pandit R. Melting of a nonequilibrium vortex crystal in a fluid film with polymers: elastic versus fluid turbulence. *Phys. Rev. E* **95**, 033119 (2017).
- [42] Gustavsson K, Einarsson J, Mehlig B. Tumbling of small axisymmetric particles in random and turbulent flows. *Phys. Rev. Lett.* **112**, 014501 (2014).
- [43] Hu X, Lin F. Global solutions of two-dimensional incompressible viscoelastic flows with discontinuous initial data. *Comm. Pure Appl. Math.* **69**, 372 (2016).
- [44] Jun Y, Steinberg V. Power and pressure fluctuations in elastic turbulence over a wide range of polymer concentrations. *Phys. Rev. Lett.* **102**, 124503 (2009).
- [45] Jun Y, Steinberg V. Mixing of passive tracers in the decay Batchelor regime of a channel flow. *Phys. Fluids* **22**, 123101 (2010).
- [46] Kurganov A, Tadmor E. New high-resolution central schemes for nonlinear conservation laws and convection-diffusion equations. *J. Comp. Phys.* **160**, 241 (2000).
- [47] Larson RG. Instabilities in viscoelastic flows. *Rheol. Acta* **31**, 213 (1992).
- [48] Lieb EH, Thirring WE. Inequalities for the moments of the eigenvalues of the Schrödinger Hamiltonian and their relation to Sobolev inequalities. In *Mathematical Physics*, pp. 269–303. Princeton University Press. (1976).
- [49] Lei Z, Masmoudi N, Zhou Y. Remarks on the blowup criteria for Oldroyd models. *J. Differ. Equ.* **248**, 328 (2010).
- [50] Meulenbroek B, Storm C, Morozov AN, van Saarloos W. Weakly nonlinear subcritical instability of visco-elastic Poiseuille flow. *J. Non-Newtonian Fluid Mech.* **116**, 235 (2004).
- [51] Mitchell J, Lyons K, Howe AM, Clarke A. Viscoelastic polymer flows and elastic turbulence in three-dimensional porous structures. *Soft Matter* **12**, 460 (2016).
- [52] Montgomery-Smith S, He W, Jack DA, Smith DE. Exact tensor closures for the three-dimensional Jeffery's equation. *J. Fluid Mech.* **680**, 321 (2011).
- [53] Morozov AN, van Saarloos W. Subcritical finite-amplitude solutions for plane Couette flow of viscoelastic fluids. *Phys. Rev. Lett.* **95**, 024501 (2005).
- [54] Musacchio S, Boffetta G. Turbulent channel without boundaries: The periodic Kolmogorov flow. *Phys. Rev. E* **89**, 023004 (2014).
- [55] Oldroyd JG. On the formulation of rheological equations of state. *Proc. R. Soc. A* **200**, 523 (1950).
- [56] Ogilvie GI, Proctor MRE. On the relation between viscoelastic and magnetohydrodynamic flows and their instabilities. *J. Fluid Mech.* **476**, 389 (2003).
- [57] Ottino JM, Wiggins S. Introduction: mixing in microfluidics *Phil. Trans. Roy. Soc. A* **362**, 923 (2004).
- [58] Pan L, Morozov A, Wagner C, Arratia PE. Nonlinear elastic instability in channel flows at low Reynolds numbers. *Phys. Rev. Lett.* **110**, 174502 (2013).

- [59] Parsa S, Calzavarini E, Toschi F, Voth GA. Rotation rate of rods in turbulent fluid flow. *Phys. Rev. Lett.* **109**, 134501 (2012).
- [60] Paschkewitz JS, Dubief Y, Dimitropoulos CD, Shaqfeh ESG, Moin P. Numerical simulation of turbulent drag reduction using rigid fibres *J. Fluid Mech.* **518**, 281 (2004).
- [61] Pereira AS, Andrade RM, Soares EJ. Drag reduction induced by flexible and rigid molecules in a turbulent flow into a rotating cylindrical double gap device: Comparison between poly(ethylene oxide), polyacrylamide, and xanthan gum. *J. Non-Newton. Fluid Mech.* **202**, 72 (2013).
- [62] Poole RJ, Budhiraja B, Cain AR, Scott PA. Emulsification using elastic turbulence. *J. Non-Newtonian Fluid Mech.* **177-178**, 15 (2012).
- [63] Poole RJ, Lindner A, Alves MA. Viscoelastic secondary flows in serpentine channels *J. Non-Newtonian Fluid Mech.* **201**, 10 (2013).
- [64] Procaccia I., L'vov VS, Benzi R. Colloquium: Theory of drag reduction by polymers in wall-bounded turbulence. *Rev. Mod. Phys.* **80**, 225 (2008).
- [65] Pumir A, Wilkinson M. Orientation statistics of small particles in turbulence, *New J. Phys.* **13**, 093030 (2011).
- [66] Robinson JC. *Infinite-dimensional dynamical systems*. Cambridge University Press (2001).
- [67] Robinson JC. Parametrization of global attractors, experimental observations, and turbulence. *J. Fluid Mech.* **578**, 495 (2007).
- [68] Shaqfeh ESG. Purely elastic instabilities in viscometric flows. *Ann. Rev. Fluid Mech.* **28**, 129 (1996).
- [69] Squires TM, Quake SR. Microfluidics: Fluid physics at the nanoliter scale. *Rev. Mod. Phys.* **77**, 977 (2005).
- [70] Stone HA, Stroock AD, Ajdari A. Microfluidics toward a lab-on-a-Chip. *Ann. Rev. Fluid Mech.* **36**, 381 (2004).
- [71] Sureshkumar R, Beris AN. Effect of artificial stress diffusivity on the stability of numerical calculations and the flow dynamics of time-dependent viscoelastic flows. *J. Non-Newtonian Fluid Mech.* **60**, 53 (1995).
- [72] Thomases B, Shelley M. Transition to mixing and oscillations in a Stokesian viscoelastic flow. *Phys. Rev. Lett.* **103**, 094501 (2009)
- [73] Thomases B, Shelley M, Thiffeault JL. A Stokesian viscoelastic flow: Transition to oscillations and mixing. *Physica D* **240**, 1602 (2011).
- [74] Thomases B. An analysis of the effect of stress diffusion on the dynamics of creeping viscoelastic flow. *J. Non-Newtonian Fluid Mech.* **166**, 1221 (2011).
- [75] Traore B, Castelain C, Burghelea T. Efficient heat transfer in a regime of elastic turbulence *J. Non-Newtonian Fluid Mech.* **223**, 62 (2015).
- [76] Vaithianathan T, Robert A, Basseur JG, Collins LR. An improved algorithm for simulating three-dimensional, viscoelastic turbulence. *J. Non-Newtonian Fluid Mech.* **140**, 3 (2006)
- [77] Virk PS, Sherman DC, Wagger DL. Additive equivalence during turbulent drag reduction. *Amer. Inst. Chem. Eng. J.* **43**, 3257 (1997).
- [78] Voth GA and Soldati A. Anisotropic particles in turbulence. *Ann. Rev. Fluid Mech. J.* **49**, 249 (2017).
- [79] Zilz J, Poole RJ, Alves MA, Bartolo D, Levaché C, Lindner A. Geometric scaling of a purely elastic flow instability in serpentine channels. *J. Fluid Mech.* **712**, 203 (2012).